



HAL
open science

Multipath and receiver models for assessing the VOR bearing error : application to wind farms

Seif Ben-Hassine

► **To cite this version:**

Seif Ben-Hassine. Multipath and receiver models for assessing the VOR bearing error : application to wind farms. Signal and Image processing. Université Paul Sabatier - Toulouse III, 2020. English. NNT : 2020TOU30047 . tel-03001293

HAL Id: tel-03001293

<https://theses.hal.science/tel-03001293>

Submitted on 12 Nov 2020

HAL is a multi-disciplinary open access archive for the deposit and dissemination of scientific research documents, whether they are published or not. The documents may come from teaching and research institutions in France or abroad, or from public or private research centers.

L'archive ouverte pluridisciplinaire **HAL**, est destinée au dépôt et à la diffusion de documents scientifiques de niveau recherche, publiés ou non, émanant des établissements d'enseignement et de recherche français ou étrangers, des laboratoires publics ou privés.



Université
de Toulouse

THÈSE

En vue de l'obtention du

DOCTORAT DE L'UNIVERSITÉ DE TOULOUSE

Délivré par : *l'Université Toulouse 3 Paul Sabatier (UT3 Paul Sabatier)*



ECOLE NATIONALE DE L'AVIATION CIVILE



Financé par :

Présentée et soutenue le *30 juin 2020* par :

SEIF BEN HASSINE

Multipath and Receiver Models for Assessing the VOR Bearing Error - Application to Wind Farms

JURY

YANNIS POUSSET	Professeur	Rapporteur
BERNARD UGUEN	Professeur	Rapporteur
NATHALIE RAVEU	Professeur	Présidente du jury
ALEXANDRE CHABORY	Professeur	Examineur
CHRISTOPHE DEHAYNAIN	Ingénieur	Membre invité
CHRISTOPHE MORLAAS	Enseignant-chercheur	Membre invité
RÉMI DOUVENOT	Enseignant-chercheur	Membre invité

École doctorale et spécialité :

GEET : Électromagnétisme et Systèmes Haute Fréquence

Unité de Recherche :

Ecole Nationale de l'Aviation Civile - TELECOM-EMA

Directeur de Thèse :

Alexandre CHABORY et Christophe MORLAAS

Rapporteurs :

Yannis POUSSET et Bernard UGUEN

Acknowledgments

First of all, I would like to thank DTI, ENAC and région Occitanie for funding this thesis work. My gratitude goes to Christophe Dehaynain, Gilbert Noël and Françoise Tukalo for their availability to discuss the work progress and the deliverable for the DTI. My thanks go also to Alexandre Chabory and Christophe Macabiau for allowing me to complete these 42 months in the TELECOM-EMA team at ENAC.

I would like to thank Yannis Pousset and Bernard Uguen for accepting to be reviewers for my work. I would also like to thank Nathalie Raveu for accepting to be examiner, jury president and attend the presentation of this work.

Words are powerless to express my gratitude to Alexandre Chabory, Christophe Morlaas and Rémi Douvenot who supervised me during these three and a half years of thesis. They have been always ready to answer my questions and have shown interest in the progress of my work. Their analysis skills and their enthusiasm have shown me that the world of research can be an exciting universe. Finally, I really appreciated their numerous re-readings and corrections of this thesis.

My thanks go to Philippe Jobert for allowing me to carry out my measurements in the Radionav laboratory at ENAC. I want to express my gratitude to Eric Charpentier-tity for his help to make these measurements successful.

I would also like to thank all my friends and colleagues at the EMA and SIGNAV teams for their help, support and kindness. I really appreciated their trust that let me get involved in the collective life of the teams. In particular, I express my gratitude to Johan, Enik, Thomas, David, Bruno, Uygar for their help and support in difficult times.

I would like to express my thankfulness to my family for giving me a dignified education, their love has made the person I am today. To my father Majid Ben Hassine, you aroused in me the endurance with your rigor. To you mom Rebeh Ben Ali, this is my deepest gratitude for your wonderful love, may this report be the best gift I can offer you. To you, my brother Saber and sister Dalila, who always supported and encouraged me during these years of study.

I would also like to thank all my friends who have given me confidence and listening at all times. I thank them for putting up with my muddy jokes, but we can't simply change overnight. I particularly thank Said, Sammouda, Aymen, Azouz, Nader, Mosaab and all the others.

Of course, this list is not exhaustive and I would like to thank all those who know me

and make me feel like I exist ...

Thank you all.

Contents

Introduction	1
1 VOR Characteristics in Multipath Context	5
1.1 Introduction	5
1.2 VOR systems	5
1.2.1 Definition	6
1.2.2 Conventional VOR	6
1.2.3 Doppler VOR	9
1.3 Overview of multipath for VOR systems	10
1.3.1 Multipath parameters	11
1.3.2 Simulation models	11
1.3.3 VOR ERror SimulatOr (VERSO)	13
1.4 Overview of VOR receivers	21
1.4.1 Standard VOR receiver	21
1.4.2 FM demodulation	22
1.4.3 Phase comparison	26
1.5 Odunaiya VOR error expressions	27
1.6 Conclusion	28
2 Digital VOR Receiver Model	29
2.1 Introduction	29
2.2 Time series of multipath parameters	29
2.2.1 Sampling criterion	29
2.2.2 Aircraft trajectories	30
2.3 Digital VOR receiver model	32
2.3.1 Receiver block diagram	32
2.3.2 I/Q signal generator	33
2.3.3 Receiver simulator	34
2.4 Illustration test	39
2.4.1 Configuration and parameters	39
2.4.2 Results	40
2.5 Conclusion	42
3 Analysis from Laboratory Measurements	43
3.1 Introduction	43
3.2 Analysis of available in-flight measurements	43
3.2.1 Configuration	44
3.2.2 Results	46
3.2.3 Explanation of the differences between the simulation and measurement results	47
3.2.4 Conclusion	48
3.3 Confrontation from VHF measurements	48

3.3.1	Description	48
3.3.2	Configuration and parameters	49
3.3.3	Results	50
3.4	Confrontation from baseband IQ measurements	53
3.4.1	Description	53
3.4.2	Configuration and parameters	53
3.4.3	Results	54
3.5	Conclusion	56
4	Analysis of the Bearing Error	57
4.1	Introduction	57
4.2	Receiver group delay	57
4.3	Validity domain of the CVOR Odunaiya expression	59
4.3.1	Comparisons between the Odunaiya expression and the receiver model	60
4.3.2	Spectral analysis of the received intermediate signals	61
4.3.3	Geometric criterion	64
4.3.4	Conclusion	66
4.4	Analytic DVOR multipath error	66
4.4.1	Confrontation test	67
4.4.2	Demonstration	67
4.4.3	Validation	71
4.5	Multipath effect on the reference signal	72
4.5.1	Configuration	72
4.5.2	Results	73
4.5.3	Conclusion	75
4.6	Conclusion	75
5	Statistical Model of the CVOR Bearing Error	77
5.1	Introduction	77
5.2	Configuration	77
5.2.1	Deterministic parameters	78
5.2.2	Statistical parameters	78
5.3	Model principle	78
5.3.1	Relative amplitude distribution	79
5.3.2	Relative phase distribution	79
5.3.3	Relative azimuth distribution	82
5.3.4	CVOR error distribution	83
5.4	Monte-Carlo Analysis	84
5.5	Test-case	86
5.5.1	Presentation of the test-case	86
5.5.2	Results	88
5.6	Conclusion	92
	Conclusion	93
A	Demonstration of the Odunaiya expressions	97
A.1	CVOR error	97
A.1.1	Single multipath	97
A.1.2	N multipath	98
A.2	DVOR error	98
A.2.1	Single multipath	99
A.2.2	N multipath	101
B	Taylor series analysis	103

C	Statistics of the wind turbine characteristics	105
D	Summary in French (Résumé français)	109
D.1	Introduction	109
D.2	Modèle de récepteur VOR numérique	110
D.2.1	Introduction	110
D.2.2	Séries temporelles de paramètres multitrajets	110
D.2.3	Présentation du modèle de récepteur	110
D.2.4	Test d'illustration	111
D.2.5	Conclusion	114
D.3	Analyse du multitrajet VORC à partir de mesures en laboratoire	114
D.3.1	Introduction	114
D.3.2	Analyse des mesures de contrôle en vol: difficultés et limites	115
D.3.3	Confrontation à partir de mesures VHF	116
D.3.4	Confrontation à partir des mesures IQ en bande de base	118
D.3.5	Conclusion	119
D.4	Analyse de l'erreur angulaire obtenue à partir du modèle de récepteur	119
D.4.1	Introduction	119
D.4.2	Retard de groupe récepteur	120
D.4.3	Domaine de validité de l'expression d'Odunaiya pour le VORC	121
D.4.4	Erreur analytique du multitrajet VORD	121
D.4.5	Effet des multitrajets sur le signal de référence	123
D.4.6	Conclusion	124
D.5	Modèle statistique de l'erreur angulaire VORC	124
D.5.1	Introduction	124
D.5.2	Configuration	125
D.5.3	Statistiques de l'erreur VORC	125
D.5.4	Cas de test	126
D.5.5	Conclusion	127
D.6	Conclusion	127
	Lists of my publications	129
	Bibliography	130

Introduction

Context

The production of electrical energy is mainly based on fossil (oil, coal, natural gas) and fissile (nuclear) fuels. The systematic use of these fuels allows for low production costs but leads to a massive release of pollutant and greenhouse gases [1]. The production of electricity from the fossil fuels is notably the source of huge amounts of CO₂. Besides, some products processed in the nuclear industry remain highly radioactive for many years. Hence, the development and exploitation of renewable energies such as wind turbines and solar panels have grown strongly in the recent years. The implementation of these equipments requires considerable areas.

The VOR (VHF Omnidirectional Range) and radars are essential systems for air navigation and surveillance of civil and military aircraft. However, these systems are very sensitive to scattering by large-size metallic and non-metallic objects such as buildings, cranes, pylons, or wind turbines. These latter deserve a special consideration because of their height. For VOR, the wind turbines yield an error on the azimuth assessed by the on-board receiver. The level of this error varies according to the proximity of the wind turbine and its size. In addition, the concentration of several wind turbines in a farm can also have a cumulative effect.

State of the art

In recent years, the impact of multipath on VOR systems has been studied in several ways. In 2004, Odunayia and Quinet [2, 3] have developed a mathematical model that can assess the performances of VOR systems when affected by multipath. In 2008, Morlaas *et al.* [4] have determined the influence of wind turbines around VOR using Radar Cross Sections RCS computed via the method of moments. The VOR error is then deduced using the expressions of Odunaiya. In 2011, De la Vega *et al.* [5] have developed an approach for determining the shadowing areas due to wind turbines and the degradation of the VOR signal in terms of Signal to Noise ratio (SNR). The method is based on the analytical calculation of the wind turbine RCS. In 2019, Shrader *et al.* [6, 7] have developed a numerical method for predicting the Doppler VOR (DVOR) bearing error caused by the wind turbines. The model has been validated by measurements of real DVOR signals-in-space.

Since 2010, the Electromagnetics and Antennas (EMA) research axis of the French Civil Aviation University (ENAC) has developed a simulator to model the electromagnetic propagation of VOR signals in the presence of scattering objects on a dielectric ground with relief [8, 9, 10]. The electromagnetic model allows to give a list of multipath parameters. The Odunaiya expressions [3] are applied in order to evaluate the VOR error. This simulator is called VERSO (VOR ERror SimulatOr). It uses deterministic methods in order to compute the multipath parameters. VERSO has been tested by means of simulations and comparisons with measurements.

Objectives

The main objective of this PhD thesis consists in providing one or several fast, accurate and validated simulation tools in order to assess the impact of multipath on the VOR bearing error in presence of wind turbines.

The main tasks to be carried out in this thesis work are:

- Development of a digital VOR receiver model which can reproduce the response of a VOR receiver in a realistic way.
- Assessment of the impact of multipath change in time along a realistic aircraft trajectory on a real VOR receiver by analyzing the bearing error from the digital VOR receiver model.
- Determination of the validity of the digital VOR receiver model and the static expressions of Odunaiya from simulations, physical analyses and laboratory measurements.
- Development of an alternative model providing the statistical distribution of the bearing error from few parameters.

Outline

This thesis work is organized in 5 chapters:

In **Chapter 1**, we introduce the general context of the study. The principle and existing types of VOR transmitters, which are the Conventional (CVOR) and Doppler VOR (DVOR), are described. The numerical methods proposed in the literature to model the characteristics of the multipath generated by the presence of large scatterers such as wind turbines are described and discussed. An overview of VOR receivers is given by presenting classical architectures. The static expressions, *i.e.* the Odunaiya expressions [3], used to compute VOR error in the VERSO simulator are reminded and discussed.

In **Chapter 2**, we present a digital VOR receiver model which can reproduce the response of a VOR receiver in a realistic way. A time series generator along a realistic aircraft trajectory is presented. Our digital VOR receiver model is detailed by describing its components. An illustration test is exposed from which the effects of the multipath

changes in time are analyzed along a realistic trajectory. Our receiver model response is compared with the Odunaiya expression in this test.

In order to validate the digital VOR receiver model, a comparison can be performed between its response and available records of in-flight measurements. We show in **Chapter 3** the limitations of this approach. Then, a solution which consists in performing laboratory measurements in a controlled environment is proposed. Comparisons with results obtained from a calibration receiver are presented and discussed in order to verify if our receiver model provides a consistent response.

In **Chapter 4**, the bearing error is analyzed from the digital VOR receiver model. The receiver group delay is presented. We present a method to determine the validity domain of the static Odunaiya expression for computing the CVOR multipath error. A DVOR analysis is also given. We evaluate the sensitivity of the VOR bearing error to the type of FM demodulator and the sensitivity of the reference signal to multipath.

In **Chapter 5**, we present an alternative model providing the statistical distribution of the CVOR bearing error from few parameters. The configuration and the statistical distributions of the input parameters are defined and justified. The principle of our model is presented by determining the statistical distributions of the multipath parameters and the CVOR error. A Monte-Carlo analysis is given in order to assess the parameter of the error distribution. Simulation results for a test-case are presented and analyzed.

In **Conclusion**, we synthesize the main results of this research work. Recommendations for future works are also presented.

Chapter 1

VOR Characteristics in Multipath Context

1.1 Introduction

The VHF Omnidirectional Range (VOR) system is one of the navaid systems: it gives an aircraft its bearing relative to magnetic North. This information can be impaired by surrounding wind turbines that produce multipath. The on-board VOR receiver then processes signals from unwanted directions, which yields a bearing error. In the literature, several methods have been proposed to model multipath and calculate its characteristics. Then, the analytic expression proposed by Odunaiya and Quinet [3] is generally used to compute the bearing error from the multipath parameters.

This chapter introduces the general context of the study by presenting the phenomenon of multipath generated by the presence of large scatterers such as wind turbines in the vicinity of VOR stations.

In Section 1.2, VOR systems are presented by describing their principle for both existing types of transmitters, namely Conventional VOR (CVOR) and Doppler VOR (DVOR). The signal modulations associated with CVOR and DVOR are presented. Multipath are then introduced in Section 1.3 by describing their characteristics. To model them, several methods from the literature are presented *e.g.* [11, 12, 10]. One of these methods has been developed by ENAC [10]. Since our work is based on this model, it is presented in details. One of the main objectives of this work is to improve the VOR receiver model. Therefore, an overview of VOR receivers is given in Section 1.4 by describing the classical architecture and the main reception steps such as demodulations and phase detection. Odunaiya expressions for the VOR error are finally presented in Section 1.5.

1.2 VOR systems

In this section, the basic principle of the VOR system is introduced. Then, the conventional and Doppler VOR are detailed by presenting their signals.

1.2.1 Definition

The VOR is a ground-based system for navigation transmitting an electromagnetic signal of frequency between 108 MHz and 118 MHz. This signal allows aircraft to navigate: it provides azimuth information with respect to magnetic North. The principle of the VOR system is shown in Figure 1.1.

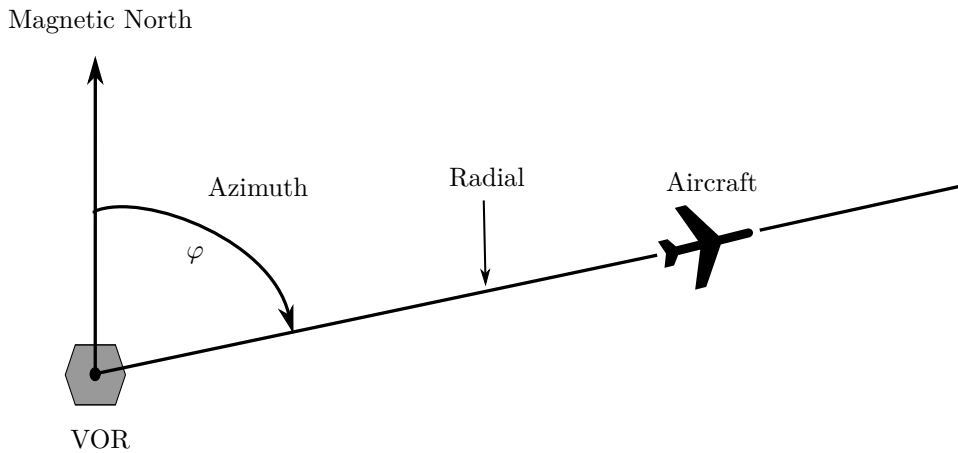


Figure 1.1: VOR principle.

There are two classes of VOR ground stations. The first is called En-route VOR. It has a typical power of 200 W and transmits frequencies between 112 MHz and 117.95 MHz. This band contains 8.33 kHz channels separated by 5 kHz. The range of this type of VOR can reach up to 200 NM. The second is called Terminal VOR (T-VOR). It transmits signals with 50 W of power in the band between 108 MHz and 111.85 MHz. The space between the 8.33 kHz channels is also 5 kHz. It differs from the En-route VOR in its limited range of 40-50 NM due to its weaker power.

There are also two different types of VOR systems. The first one is called Conventional VOR (CVOR) because it is the first to have been implemented. The second one is called Doppler VOR (DVOR) because it uses the properties of the Doppler-Fizeau effect. The DVOR has been established to address some signal disturbance problems due to the CVOR environment. For each kind of VOR signals, the receiver is the same. The description of CVOR and DVOR is given in the next section.

1.2.2 Conventional VOR

For the Conventional VOR [13], the variable signal (VAR) containing the azimuth information is modulated in amplitude and the reference signal (REF) in frequency. This type of VOR is very sensitive to perturbations generated by the propagation channel and in particular by multipath [14]. Figure 1.2 shows a CVOR antenna.



Figure 1.2: A CVOR antenna [wikimedia commons].

In order to generate the variable signal, a low frequency (LF) signal at $f_{LF} = 30$ Hz containing the azimuth information φ_0 modulates the VHF carrier in amplitude with a modulation rate m_a of 30%. The carrier is characterized by an amplitude a_0 , a frequency f_0 and a phase θ_0 . The variable signal is then expressed as

$$U_{\text{var}}^{\text{C}} = a_0 \cos(2\pi f_0 t + \theta_0) [1 + m_a \cos(2\pi f_{LF} t - \varphi_0)]. \quad (1.1)$$

The block diagram of the VAR signal generation for a CVOR is shown in Figure 1.3.

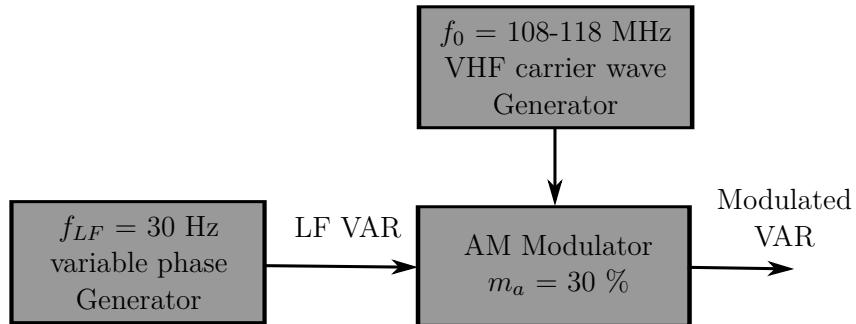


Figure 1.3: Block diagram of the VAR signal generation for a CVOR.

In order to generate the reference signal, a sub-carrier at $f_{sc} = 9960$ Hz is modulated in frequency by the LF signal at 30 Hz. The modulation index set by ICAO being $m_f = 16$, the bandwidth of REF signal [15] is then

$$W_{\text{ref}} = 2 f_{LF} m_f = 960 \text{ Hz}. \quad (1.2)$$

The 9960 Hz sub-carrier modulates in amplitude the VHF carrier. The reference signal (REF) is thus expressed as

$$U_{\text{ref}}^{\text{C}} = a_0 \cos(2\pi f_0 t + \theta_0) [1 + m_a \cos(2\pi f_{sc} t + m_f \sin(2\pi f_{LF} t))]. \quad (1.3)$$

The block diagram of the REF signal generation for a CVOR is shown in Figure 1.4.

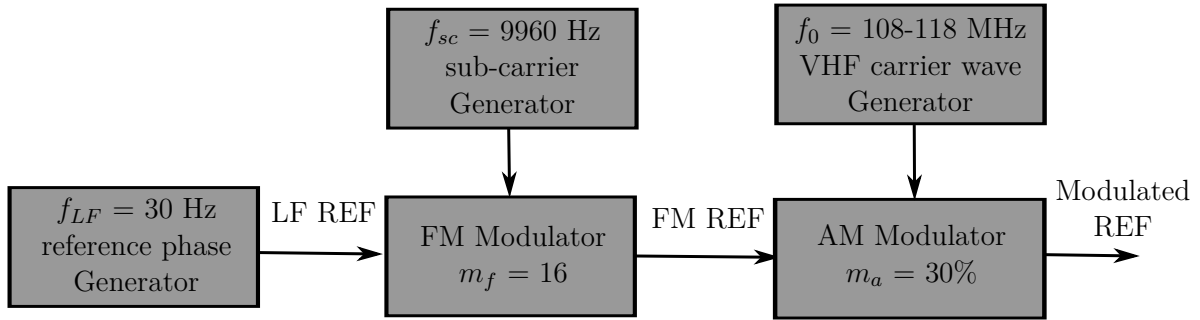


Figure 1.4: Block diagram of the REF signal generation for a CVOR.

The total signal radiated by CVOR is the sum of the REF and VAR signals. It is given by

$$U_{\text{tot}}^C = a_0 \cos(2\pi f_0 t + \theta_0) [1 + m_a \cos(2\pi f_{sc} t + m_f \sin(2\pi f_{LF} t)) + m_a \cos(2\pi f_{LF} t - \varphi_0)]. \quad (1.4)$$

The VHF carrier is also modulated by a voice and a morse identification signals. These additional components of the VOR signal are ignored in our study. Only the impact of multipath on the navigation information contained in the REF and VAR signals is studied. The frequency bands of the components of the CVOR signal are shown in Figure 1.5.

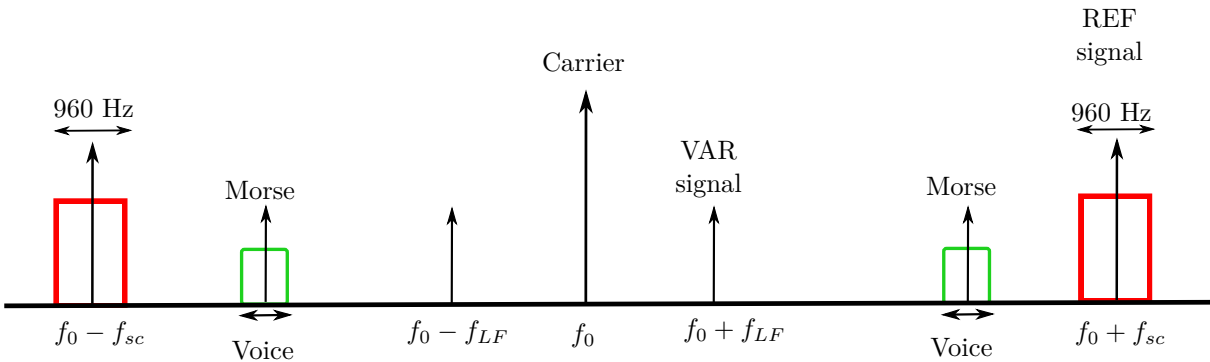


Figure 1.5: Frequency bands of the components of the CVOR signal.

The amplitude modulation is much less robust than frequency modulation in a noisy or multipath propagation channel [16]. Hence, The variable signal is very sensitive to multipath for CVOR. The DVOR has been developed to minimize this effect.

1.2.3 Doppler VOR

The Doppler VOR has been established to overcome some signal disturbance problems due to the presence of multipath in the propagation channel. A DVOR antenna is illustrated in Figure 1.6.



Figure 1.6: A DVOR antenna [wikimedia commons].

In DVOR, modulations of the VAR and REF components are reversed: the azimuth information is modulated in frequency and the reference signal in amplitude. This renders DVOR more robust to multipath than CVOR.

An omnidirectional central antenna is used to transmit the modulated reference signal. It is expressed as

$$U_{\text{ref}}^{\text{D}} = a_0 \cos(2\pi f_0 t + \theta_0) [1 + m_a \cos(2\pi f_{LF} t)]. \quad (1.5)$$

The modulated variable signal is generated by means of a large number of antennas (48 for Thales DVOR) arranged on a circle. It is expressed as

$$U_{\text{var}}^{\text{D}} = a_0 \cos(2\pi f_0 t + \theta_0) [1 + m_a \cos(2\pi f_{sc} t + m_f \sin(2\pi f_{LF} t - \varphi_0))]. \quad (1.6)$$

The block diagrams of the REF and VAR signals generation for a DVOR are shown in Figures 1.7 and 1.8, respectively.

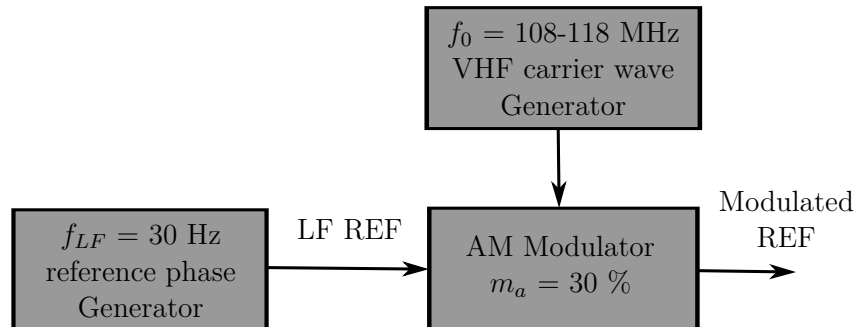


Figure 1.7: Block diagram of the REF signal generation for a DVOR.

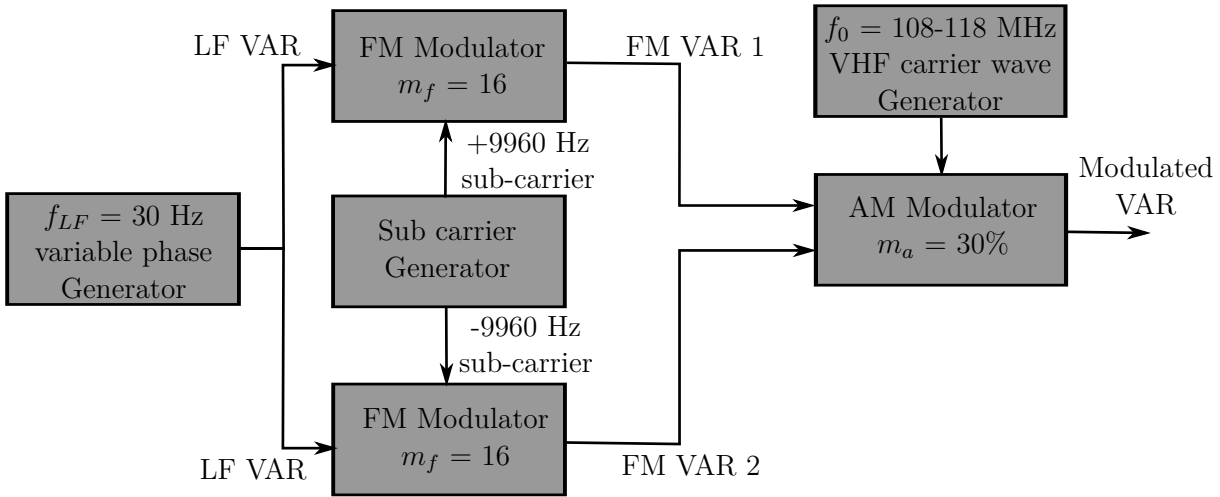


Figure 1.8: Block diagram of the VAR signal generation for a DVOR.

The total signal radiated by DVOR is the sum of the REF and VAR signals. It is given by

$$U_{\text{tot}}^{\text{D}} = a_0 \cos(2\pi f_0 t + \theta_0) [1 + m_a \cos(2\pi f_{sc} t + m_f \sin(2\pi f_{LF} t - \varphi_0)) + m_a \cos(2\pi f_{LF} t)]. \quad (1.7)$$

The frequency bands of the components of the DVOR signal are shown in Figure 1.9.

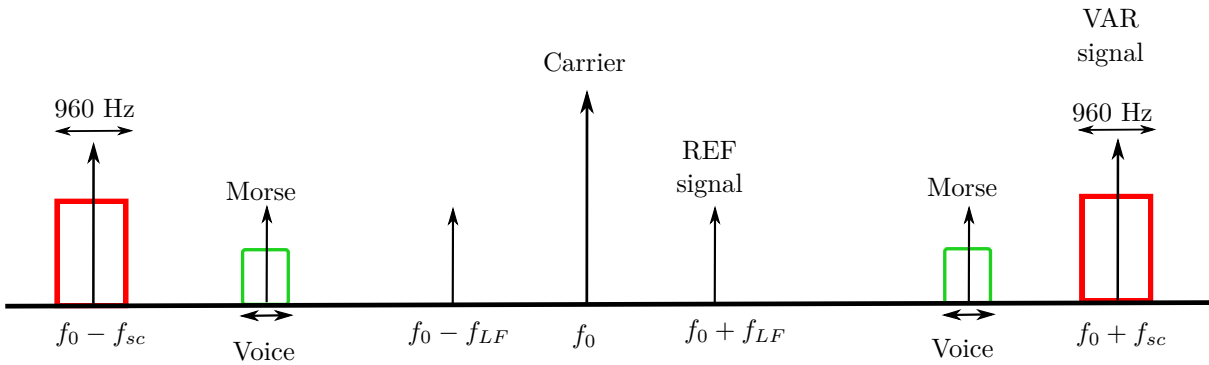


Figure 1.9: Frequency bands of the components of the DVOR signal.

1.3 Overview of multipath for VOR systems

In this section, we introduce the phenomenon of multipath generated by the presence of large scatterers such as wind turbines in the vicinity of VOR systems presented in the previous section. Several methods from literature are given in order to model the

characteristics of multipath. Since this work relies on the model developed by ENAC, it is presented in details.

1.3.1 Multipath parameters

The presence of a wind farm in a VOR environment generates the phenomenon of multipath due to scattering on the fixed and mobile components of the wind turbines. This phenomenon implies an error on the azimuth information at the receiver level. Figure 1.10 shows the phenomenon of multipath due to a wind farm. The N multipath are characterized by their respective amplitudes a_n , phases θ_n and azimuths with respect to magnetic North φ_n .

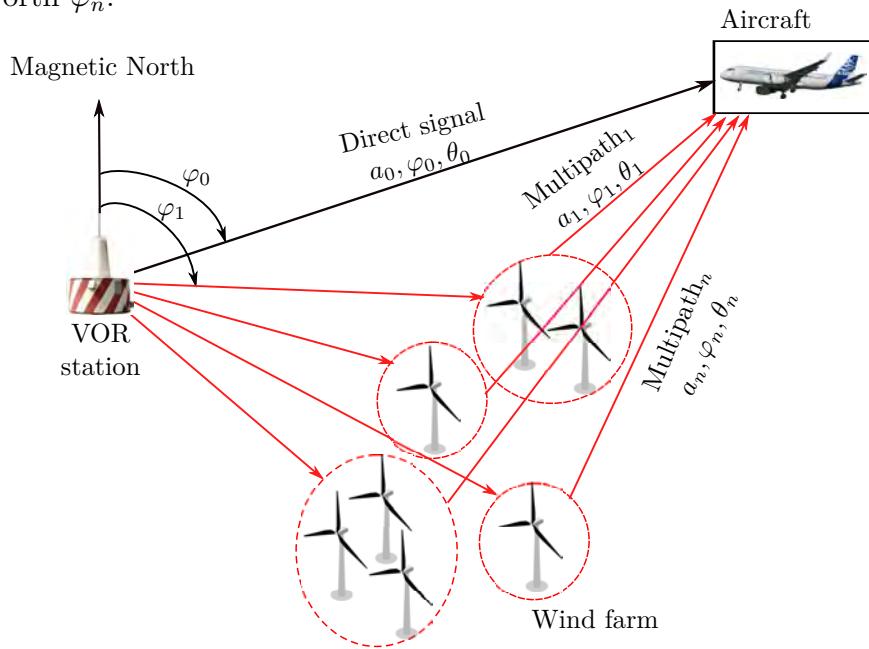


Figure 1.10: Multipath due to a wind farm in the vicinity of a VOR station.

The electromagnetic modelling of the influence of multipath on VOR system and the computation of the bearing error are presented in the next section.

1.3.2 Simulation models

There are several methods in the literature to model the influence of wind turbines on VOR systems and compute the VOR error. The advantages and limitations of each model are discussed here.

1.3.2.a Physical Optics and Method of Moments

The "MONURBS" tool developed by González *et al.* [11, 17], calculates the field scattered by a simplified wind turbine model. This tool works at the VOR and radar frequencies.

The scattered field is calculated using either the Method of Moments (MoM) or the Physical Optics (PO). The MoM is characterized by its computational accuracy but it requires more resources for the calculation of large complex scenes.

Morlaas *et al.* [4] have developed a technique that consists in pre-computing by the MoM a database of fields scattered by objects which are illuminated by a plane wave at different incidences. These scattering objects are the elements of a wind turbine: a blade, a mast and a nacelle. The scenario to be modeled is then used to determine the orientation of the objects relative to the electromagnetic source (VOR station) and the position of the receiver. The field scattered by the wind turbine and the direct field are then computed at the aircraft position, taking into account a planar dielectric ground using the image theory.

1.3.2.b Modelling from Radar Cross Section expressions

The computation of the scattered field by a simplified wind turbine model can be performed by splitting the wind turbine into simple canonical elements, and using analytical bistatic Radar Cross Section (RCS) expressions for each element. Several works have been realized based on this solution [12, 18] with which the computation of the scattered field is simple and fast. However, these methods have several limitations. Firstly, the antenna pattern and the ground are not taken into account because only a plane wave illumination is considered. Secondly, this method is only applicable for wind turbines modeled by simple canonical elements, *e.g.* cylinders or spheres, which is a strong approximation.

1.3.2.c Hybridization Geometric Optics-Physical Optics

Weinmann *et al.* [19, 20, 21, 22] have developed a tool based on the combination of Geometric Optics (GO) with PO. GO is implemented by the Shooting and Bouncing Rays (SBR) algorithm in order to model the phenomenon of multiple reflections by wind turbines. This tool has been tested at radar frequencies. The contribution of each ray is calculated according to the PO formulation. In addition, the contribution of the edge and corner diffraction is included using the Physical Theory of Diffraction (PTD). The simulations have been done with a generic wind turbine model. The computation of this developed tool can take into account the ground and the terrain using a stochastic scattering model for the ray tracing algorithm [21, 22].

1.3.2.d Hybridization of the Parabolic Equation with Physical Optics

ENAC EMA [8, 9, 10, 23, 24, 25] has developed a deterministic simulator of the VOR error called VERSO (VOR ERror SimulatOr). This simulator is based on the combination of Parabolic Equation (PE) and PO to calculate the scattered field by wind turbines. The two-ray model is used to compute the direct field received by the aircraft. VERSO neglects the interactions between wind turbines as well as the shadowing effects. VERSO allows to

simulate different types of scatterers: wind turbines and buildings. This tool is detailed in Section 1.3.3. The overview of VERSO simulator is shown in Figure 1.11.

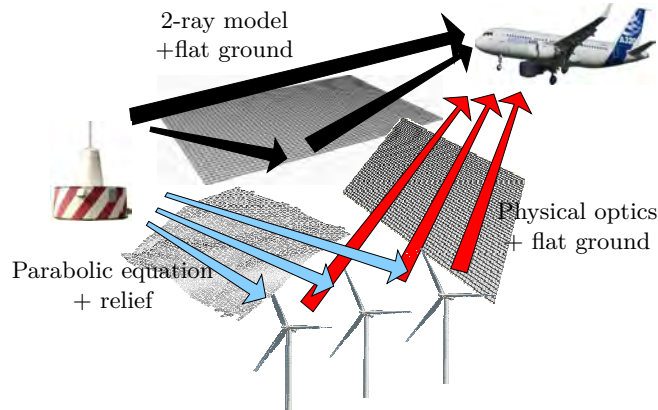


Figure 1.11: Numerical methods in the VERSO simulator [10].

Another hybridization between PE and PO has been proposed by Casanova *et al.* [26] for modeling the propagation of communication signals from a transmitter to a receiver on irregular terrain and in the presence of a wind turbine.

The VERSO simulator computes the parameters of the multipath. The Odunaiya expressions are applied in order to calculate the VOR error. We adopt this electromagnetic model in the context of our thesis work. VERSO simulator is then introduced in the next section.

1.3.3 VOR Error Simulator (VERSO)

VERSO is a deterministic simulator of the VOR error due to obstacles near the ground station. In this section, each calculation step of this simulator is explained. Figure 1.12 shows the block diagram of the simulator.

In Section 1.3.3.a, the configuration parameters are firstly defined. The direct signal is computed as presented in Section 1.3.3.b. The same calculation is used to initiate the PE. The propagation of the fields from the VOR to the scatterers is performed by using the PE as detailed in Section 1.3.3.c. The meshing of the scatterers is described. In Section 1.3.3.d, the incident fields are then interpolated on this mesh. The scattered fields are calculated by applying the approximations of PO as shown in Section 1.3.3.e. Finally, the multipath parameters are extracted and combined in order to compute analytically the VOR error as presented in Section 1.3.3.f and 1.3.3.g, respectively.

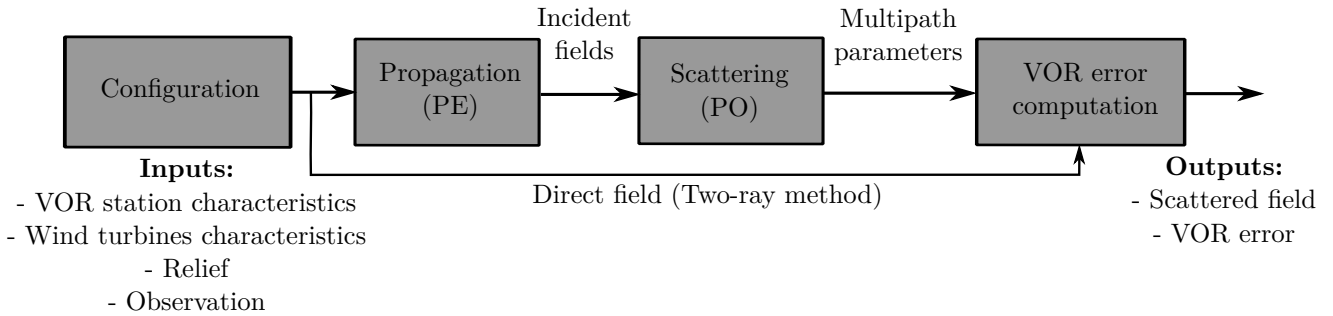


Figure 1.12: Block diagram of VERSO simulator.

1.3.3.a Configuration

VERSO takes as input the configuration parameters: the position and the characteristics of the VOR station, the positions and the characteristics of the wind turbines, the relief and the observation points.

The VOR station is characterized by its position, its frequency, its height above the ground, its power and its radiation pattern. Figure 1.13 presents the radiation patterns of two antennas of type Thomson (AN431) and Thales (540C).

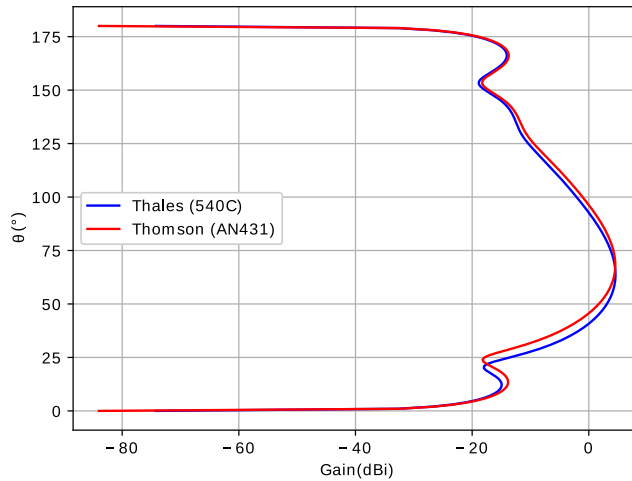


Figure 1.13: Radiation patterns of Thomson (AN431) and Thales (540C) antennas.

A generic model of wind turbine is implemented in VERSO. This model includes three elements as presented in Figure 1.14:

- **The mast**, modeled by a metallic conical section and characterized by its height H , its ground diameter D_1 and its top diameter D_2 .

- **The nacelle**, modeled by a metallic rectangular box and characterized by its size h_1 , h_2 , h_3 .

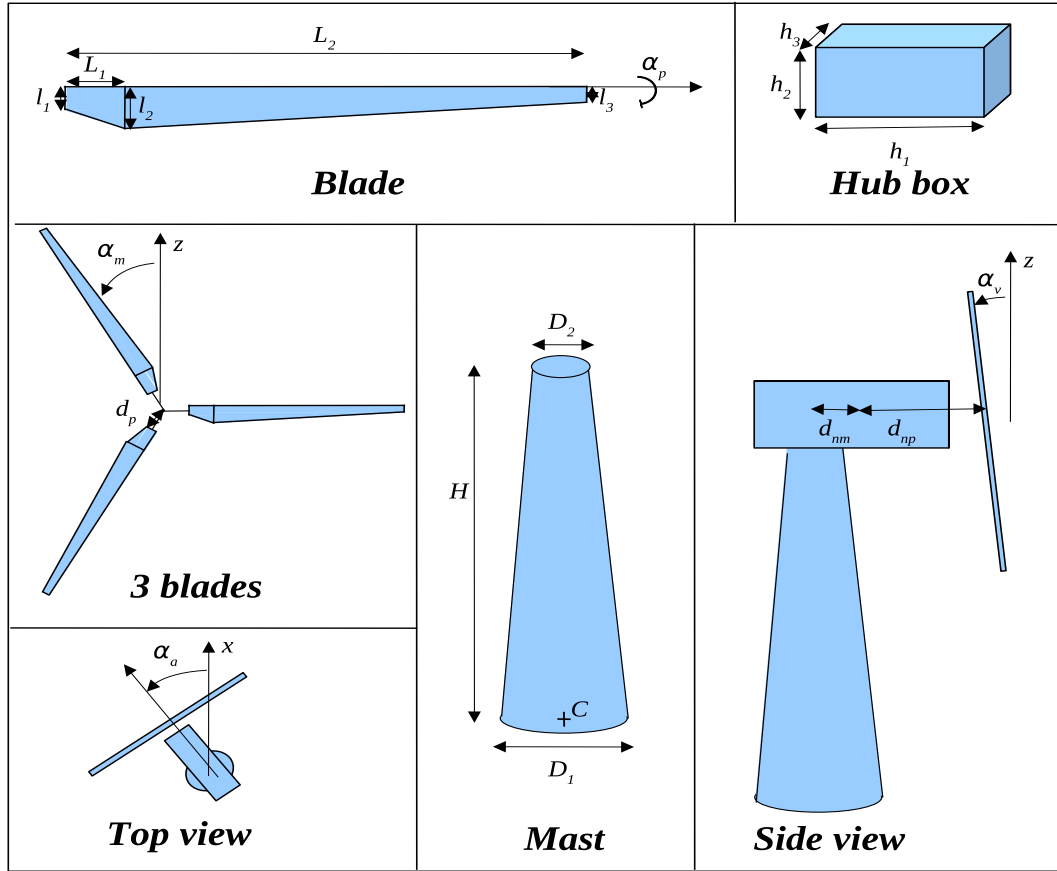


Figure 1.14: Wind turbine model [27].

- **The blades**, modeled by a simplified multilayer dielectric structure in agreement with the model of Morlaas et al. [4]. We show in Figure 1.15 the structure of one blade composed by two parallel dielectric layers separated by air. This structure is represented by two trapezoids and characterized by the length of the first trapezoid L_1 , the total length L_2 , the initial, maximal and final widths l_1 , l_2 , l_3 . Each dielectric layer is characterized by its thickness w_l , its permittivity ϵ_l and its conductivity σ_l .

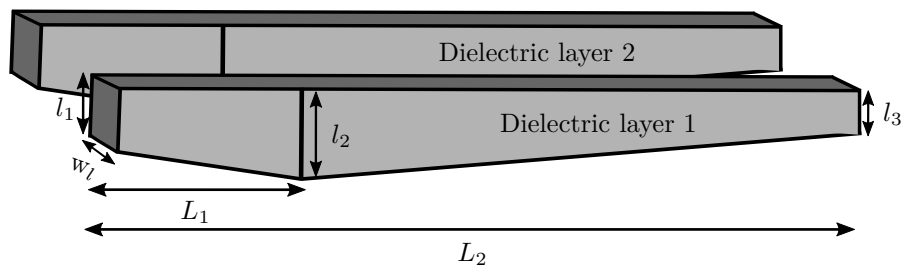


Figure 1.15: Model of one blade composed by two dielectric layers .

The respective positions of these elements are specified with the following parameters:

- The coordinates of the center of the mast C with respect to the ground level,
- The distance d_{nm} between the center of the mast and the center of the nacelle,
- The distance d_{np} between the hub and the center of the nacelle,
- The distance d_p between the hub and the blades.

We also define the following rotation angles:

- The rotation angle of the blades α_p about their longitudinal axis,
- The rotation angle of the blades α_m about the hub,
- The inclination of the hub α_v relative to the vertical axis,
- The orientation (azimuth) of blades and nacelle α_a .

We can define several types of grounds (dry, humid, fresh water, sea water, etc.) which are characterized by their respective relative permittivity ε_{gr} and conductivity σ_{gr} . The reliefs are defined between the VOR antenna and the wind turbines. They are characterized by their altitude with respect to the distance to the VOR station. The relief is obtained from the IGN data.

Several types of observations points can be defined in VERSO: half sphere, horizontal and vertical cuts, horizontal and vertical planes.

1.3.3.b Computation by the two-ray method

The direct field received by the on-board receiver is calculated using the two-ray method. The antenna far field at the observation point r_{obs} is expressed in free space as

$$E_{\varphi}(r_{obs}) = \sqrt{\frac{\zeta_0 P_{ant}}{2\pi} G_{ant}} \frac{e^{j(\theta_{ant} - kr_{obs})}}{r_{obs}}, \quad (1.8)$$

where ζ_0 is the vacuum impedance, P_{ant} is the antenna power, G_{ant} and θ_{ant} are the gain and the phase of the radiation pattern in the observation direction, respectively, k is the wavenumber. In the presence of ground, an image antenna is added. Then, the direct field and the image field are summed to obtain the total radiated field given by

$$E_{tot} = E_{dir} + \Gamma E_{im}, \quad (1.9)$$

where E_{dir} and E_{im} are the direct and image fields, respectively. Γ is the Fresnel reflection coefficient. This calculation is also used to obtain the initial fields in the PE simulations as explained in the next section.

1.3.3.c Propagation by Parabolic Equation

The PE is used to calculate the propagation of the electromagnetic field from the VOR antenna to the scatterers. The PE is a 2D method that neglects the backpropagation. It is accurate in the presence of complex ground and atmosphere [28]. The antenna pattern is taken into account. To solve PE, the propagation is iteratively computed along $\hat{\rho}$ in the cylindrical coordinate system $(\hat{\rho}, \hat{\varphi}, \hat{z})$ centered on the VOR station.

The PE is obtained from the 2D Helmholtz equation and is given by [29]

$$\frac{\partial u}{\partial \rho} = -\frac{jk_0}{2} \left(\frac{1}{k_0^2} \frac{\partial^2 u}{\partial z^2} + (n_r^2 - 1)u(\rho, z) \right), \quad (1.10)$$

where u is the reduced variable expressed as

$$u = E_\varphi \sqrt{\rho} e^{jk_0 \rho}, \quad (1.11)$$

k_0 is the wavenumber in vacuum, n_r is the refractive index. Equation (1.10) is valid for small angles around the paraxial direction of propagation $\hat{\rho}$.

To solve the PE, the split-step Fourier method is used [30]. The principle of this method is shown in Figure 1.16.

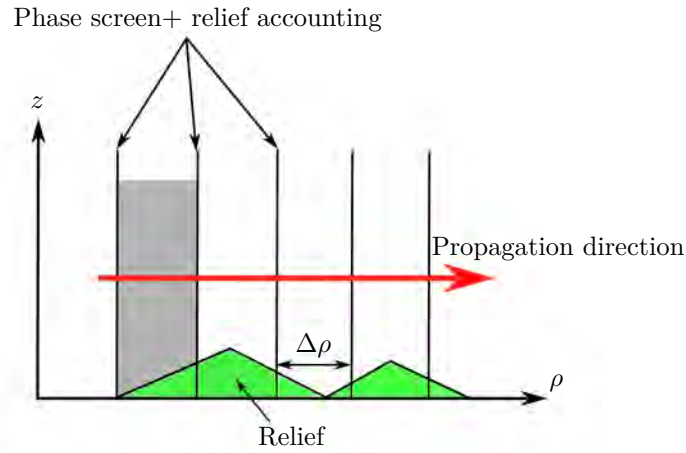


Figure 1.16: Split-step Fourier method.

The field is initialized on a vertical with the two-ray method. Then, the field is calculated in the spectral domain with a Fourier transform. The field is propagated in the spectral domain and then, with an inverse transform, it is obtained on a new vertical. This means that (1.10) is solved iteratively by

$$u(\rho + \Delta \rho, z) = \exp \left(-\frac{jk_0(n_r^2 - 1)\Delta \rho}{2} \right) \mathfrak{F}^{-1} \left[\exp \left(\frac{jk_z^2 \Delta \rho}{k_0} \right) \mathfrak{F}(u(\rho, z)) \right], \quad (1.12)$$

where $\Delta\rho$ is the horizontal step of propagation, k_z is the z component of the wavevector, \mathfrak{F} and \mathfrak{F}^{-1} are the Fourier transform and its inverse, respectively.

In order to take into account the relief in the split-step Fourier method, a staircase modelling is used [28]. The Leontovich impedance boundary conditions are used in order to take into account the dielectric aspect of the ground which reflection coefficient for the horizontal polarization is expressed as

$$R = \frac{k_z - k_{zg}}{k_z + k_{zg}}, \quad (1.13)$$

where k_z and k_{zg} are the longitudinal components of the wavevectors in the air and ground, respectively. They are given by

$$\begin{aligned} k_z &= k_0 \cos \theta_i, \\ k_{zg} &= \sqrt{k_g^2 - k_0^2 \sin^2 \theta_i}, \end{aligned} \quad (1.14)$$

where θ_i is the angle of incidence and k_g is the wavenumber in the ground.

1.3.3.d Hybridization of the Parabolic Equation with Physical Optics

In order to simulate the wind turbine scattering by PO, the wind turbine is first meshed into multilayer-slab or metallic polygonal facets. Figure 1.17 shows an example of wind turbine mesh.

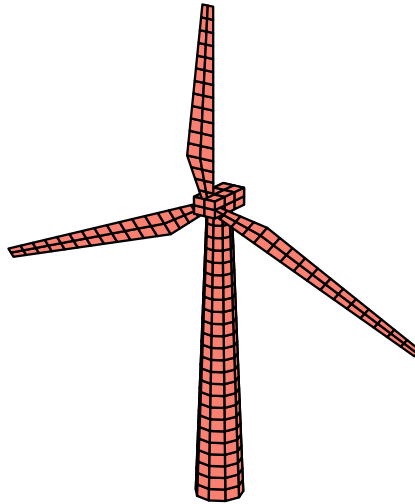


Figure 1.17: Wind turbine mesh.

The PE provides the incident field on the vertical axis of the object, which corresponds to the central axis. An interpolation operation is realized by assuming that each facet is illuminated by a plane wave characterized by an amplitude, a phase and a direction of propagation.

For a facet p , the amplitude and the phase of the plane wave are obtained by performing an interpolation of the incident field on the radial and the vertical coordinates (ρ_p, z_p) of the facet barycenter \mathbf{b}_p .

The direction of propagation of the plane wave is defined on this facet p by

$$\hat{\mathbf{s}}_p = \frac{k_{\rho p} \hat{\boldsymbol{\rho}} + k_{z p} \hat{\mathbf{z}}}{k_0}, \quad (1.15)$$

where $k_{\rho p}$ is the radial component of the wave vector expressed as

$$k_{\rho p} = \sqrt{k_0^2 - k_{z p}^2}, \quad (1.16)$$

where $k_{z p}$ is the vertical component, which is calculated from a linear regression of the phase of the incident field computed on the vertical axis of the scatterer.

The incident field on each of the mesh facets is assimilated to a plane wave. We can then apply the computation of PO.

1.3.3.e Scattering by Physical Optics

The computation of the scattered field is performed by PO approximations. We consider a facet p illuminated by a plane wave $(\mathbf{E}_i, \mathbf{H}_i)$. The reflected and transmitted fields $(\mathbf{E}_r, \mathbf{H}_r)$ and $(\mathbf{E}_t, \mathbf{H}_t)$ are deduced at the facet interface using the reflection and transmission coefficients as presented in [31]. From the equivalence principle, the scattering of facet p amounts to the radiation of electric and magnetic currents given by

$$\begin{aligned} \mathbf{J}_p &= \hat{\mathbf{n}}(\mathbf{b}_p) \times (\mathbf{H}_i(\mathbf{b}_p) + \mathbf{H}_r(\mathbf{b}_p) - \mathbf{H}_t(\mathbf{b}_p)), \\ \mathbf{M}_p &= -\hat{\mathbf{n}}(\mathbf{b}_p) \times (\mathbf{E}_i(\mathbf{b}_p) + \mathbf{E}_r(\mathbf{b}_p) - \mathbf{E}_t(\mathbf{b}_p)), \end{aligned} \quad (1.17)$$

where $\hat{\mathbf{n}}(\mathbf{b}_p)$ is the normal vector of the surface at barycenter \mathbf{b}_p . We assume that the observation point \mathbf{r} is located in the far field of each facet, which corresponds to

$$\|\mathbf{r} - \mathbf{b}_p\| \gg \frac{2D_p^2}{\lambda}, \quad (1.18)$$

where D_p represents the size of the facet p . The currents \mathbf{J}_p and \mathbf{M}_p radiate the field \mathbf{E}_p scattered by the facet p . $\mathbf{E}_p(\mathbf{r})$ is given by

$$\mathbf{E}_p(\mathbf{r}) = \frac{jk_0\zeta_0}{4\pi} \hat{\mathbf{r}}_p \times (\hat{\mathbf{r}}_p \times \mathbf{J}_p + \mathbf{M}_p) \frac{e^{-jk_0 r_p}}{r_p} \iint_{S_p} e^{-jk_0(\hat{\mathbf{s}}_p - \hat{\mathbf{r}}_p) \cdot (\mathbf{r}' - \mathbf{b}_p)} d\mathbf{r}', \quad (1.19)$$

where S_p represents the surface of the facet p , $\mathbf{r}_p = r_p \hat{\mathbf{r}}_p$ is the vector between the barycenter \mathbf{b}_p and the observation point \mathbf{r} . The integral of the linear phase on a polygonal surface is calculated following Lee and Mittra [32]. The image theory [33] is applied between the scatterer and the observation points to take into account the ground reflection.

1.3.3.f Extraction of the multipath parameters

This section presents the extraction of the multipath parameters from the fields (direct and scattered) previously computed in order to obtain the bearing error.

We consider that each facet p , characterized by an azimuth φ_p , yields a multipath. In our study, the on-board receiving antenna is considered as isotropic and horizontally polarized. Therefore, the induced voltage at the terminal of the receiver antenna is defined by

$$V_p = \sqrt{\frac{\lambda^2 \Re(Z_{\text{in}})}{\pi \zeta_0}} E_p^H, \quad (1.20)$$

where Z_{in} is the antenna impedance, E_p^H is the component in horizontal polarization of the scattered field defined in (1.19). The amplitude a_p of the multipath corresponds to the amplitude of the induced voltage V_p ,

$$a_p = |V_p|. \quad (1.21)$$

The phase θ_p of the multipath p is defined by

$$\theta_p = \angle V_p. \quad (1.22)$$

Each facet of the scatterer corresponds to one multipath. This leads to an important computation time for a large number of obstacles. Therefore, we group multipath with nearby azimuths. To do so, we subdivide $[0, 2\pi]$ with a criterion δ_φ to obtain the following clusters

$$\Omega_\varphi^M = \{[0, \delta_\varphi], [\delta_\varphi, 2\delta_\varphi], \dots, [(M-1)\delta_\varphi, M\delta_\varphi]\}, \quad M\delta_\varphi = 2\pi \quad (M \in \mathbb{N}). \quad (1.23)$$

We gather all the multipath corresponding to the same cluster Ω_φ^N , from which we define one equivalent multipath. This latter is defined by an average azimuth φ_n

$$\varphi_n = \frac{1}{\dim \Omega_\varphi^n} \sum_{p \in \Omega_\varphi^n} \varphi_p, \quad (1.24)$$

an amplitude a_n

$$a_n = \left| \sum_{p \in \Omega_\varphi^n} V_p \right|, \quad (1.25)$$

and a phase θ_n

$$\theta_n = \angle \left(\sum_{p \in \Omega_\varphi^n} V_p \right). \quad (1.26)$$

1.3.3.g VOR error computation

The bearing error is computed from the multipath characteristics by means of the analytic expressions proposed by Odunaiya and Quinet [3] which are given by

$$\varepsilon_{\text{Od}}^{\text{C}} = \tan^{-1} \left(\frac{\sum_{n=1}^N \frac{a_n}{a_0} \cos(\theta_n - \theta_0) \sin(\varphi_n - \varphi_0)}{1 + \sum_{n=1}^N \frac{a_n}{a_0} \cos(\theta_n - \theta_0) \cos(\varphi_n - \varphi_0)} \right) \quad (1.27)$$

for a CVOR, and

$$\varepsilon_{\text{Od}}^{\text{D}} = \tan^{-1} \left(\frac{2 \sum_{n=1}^N \frac{a_n}{a_0} \cos(\theta_n - \theta_0) J_1 \left(2m_f \sin \left(\frac{\varphi_1 - \varphi_0}{2} \right) \right) \cos \left(\frac{\varphi_1 - \varphi_0}{2} \right)}{m_f + 2 \sum_{n=1}^N \frac{a_n}{a_0} \cos(\theta_n - \theta_0) J_1 \left(2m_f \sin \left(\frac{\varphi_1 - \varphi_0}{2} \right) \right) \sin \left(\frac{\varphi_1 - \varphi_0}{2} \right)} \right) \quad (1.28)$$

for a DVOR, where J_1 is the Bessel function of the first-order.

The formulation (1.28) is only valid for weak multipath relatively to the direct field. An illustration of these expressions is given later in Section 1.5. To demonstrate these formulations, Odunaiya and Quinet consider that the demodulation, the filtering and the phase comparison are ideal. In the next section, the standard architecture of a VOR receiver is presented. Some models of FM demodulators and phase detectors are given from the literature.

1.4 Overview of VOR receivers

In this section, the operating principle of a standard VOR receiver is presented. Then, we focus on the FM signal demodulator and phase comparator applied in the VOR receiver by presenting some types of these components that exist in the literature.

1.4.1 Standard VOR receiver

The purpose of the on-board VOR receiver is to measure the phase shift between the reference and variable signals. It should be noted that a receiver can process signals from both CVOR and DVOR. Figure 1.18 shows the block diagram of the standard architecture of a VOR receiver [15, 34, 35, 36].

First, the VHF electromagnetic waves are received by the antenna. The signal from the desired beacon is detected, amplified and filtered in the first steps of reception. The AM detector performs an amplitude demodulation of the carrier in order to recover the modulating signals; one of the two 30 Hz signals, the 9960 Hz sub-carrier, the 1020 Hz identification signal and the 300/3000 Hz voice signal. These signals are detected separately using dedicated filters. A frequency modulation (FM) detector and a 30 Hz filter recover the LF signal modulating the 9960 Hz sub-carrier. A phase comparator is then

applied to calculate the phase shift between the two 30 Hz signals and thus be able to interpret the angle of the radial on which the aircraft is located. The information is finally filtered to remove unwanted noise and sent to the display devices.

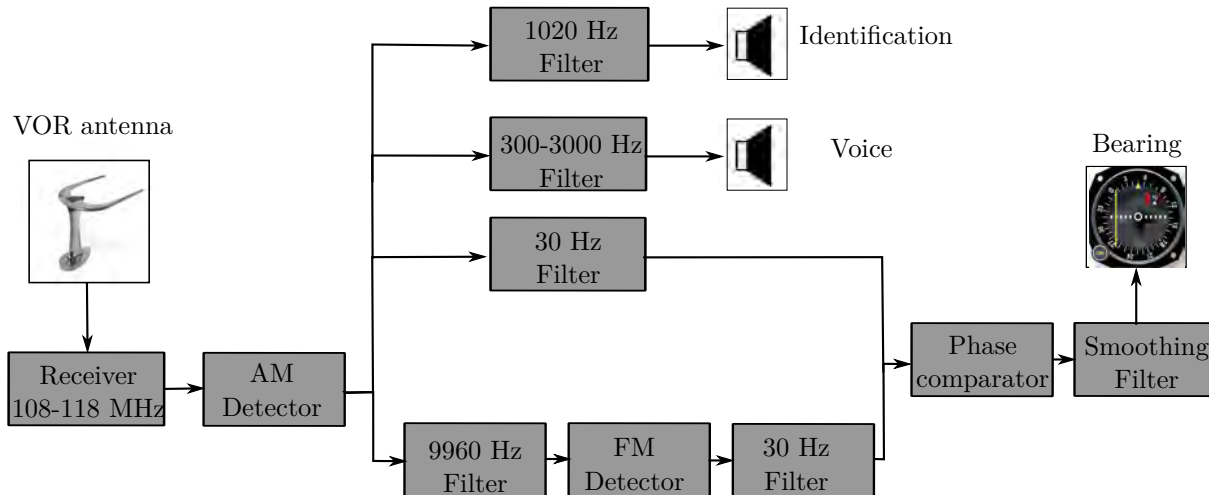


Figure 1.18: Block diagram of the standard architecture of VOR receiver.

In the next sections, the two most complex blocks, *i.e.* the FM demodulator and the phase comparator, are explained in details.

1.4.2 FM demodulation

The demodulation of the FM signal at 9960 Hz requires a system that produces an output signal proportional to the instantaneous frequency of the applied signal. There are different categories of FM demodulators [37, 38, 39, 40]: FM-to-AM frequency discrimination, zero-crossing detection, phase-locked loop (PLL) frequency detection and phase-shift discrimination. These categories are described in this section.

1.4.2.a FM-to-AM frequency discrimination

Figure 1.19 shows the block diagram of an FM-to-AM frequency discriminator. A conversion to an AM signal is applied to the FM input signal using a differentiator. The AM signal is demodulated with an envelope detector to extract the information [37].

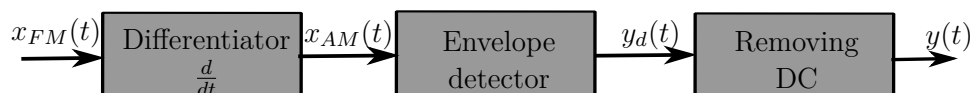


Figure 1.19: Block diagram of FM-to-AM frequency discriminator.

We consider an FM input signal expressed as

$$x_{FM}(t) = A_c \cos[2\pi f_c t + \theta(t)], \quad (1.29)$$

where A_c and f_c are the amplitude and frequency of the carrier, respectively. $\theta(t)$ is the phase containing the information $m(t)$. It is given by

$$\theta(t) = m_f \int_0^t m(\tau) d\tau. \quad (1.30)$$

At the differentiator output, the signal is given in the form of

$$x_{AM}(t) = -A_c \left[2\pi f_c + \frac{d\theta(t)}{dt} \right] \sin[2\pi f_c t + \theta(t)]. \quad (1.31)$$

The envelope of this signal is expressed as

$$y_d(t) = -A_c \left[2\pi f_c + \frac{d\theta(t)}{dt} \right]. \quad (1.32)$$

A DC block removes the constant carrier-frequency offset ($-2\pi A_c f_c$). Thus, we get an output signal in the form of

$$y(t) = -A_c \frac{d\theta(t)}{dt}. \quad (1.33)$$

It is easy to design this type of FM demodulator. Nevertheless, as this model is based on FM-to-AM conversion, it makes the system sensitive to interferences and causes some ripples in the demodulated signal as noted in [37].

1.4.2.b Zero-crossing detection

The FM demodulation can also be performed with the zero-crossing algorithm [37, 41, 42]. The block diagram of zero crossing demodulation is shown in Figure 1.20.

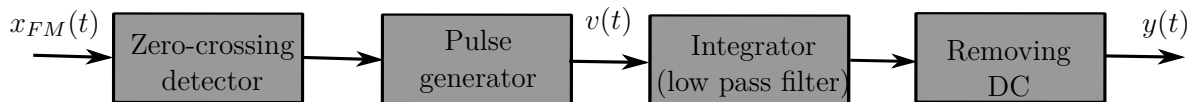


Figure 1.20: Zero-crossing demodulation.

A zero-crossing detector is applied to determine the positive zero-crossing points. When the input signal amplitude is modified from a negative to a positive value, a zero-crossing point impulse is generated. Then, these impulses are converted to pulse chain $v(t)$ with

a fixed amplitude and duration by means of a pulse generator. To find the modulating signal at the instant t , the pulse chain is continuously integrated over the past T seconds. A DC block is then applied to remove the carrier frequency offset.

For this type of FM demodulator, a higher sampling frequency is required in order to get a higher demodulation accuracy as noted in [37, 41].

1.4.2.c Phase-Locked Loop (PLL)

The Phase-Locked Loop (PLL) is a system used for the detection and demodulation of FM signals. As noted in [37], the principle of the PLL consists in monitoring the phase variations of the input signal and providing a signal at the output depending on the rate of variation of the input phase. The PLL shows a good demodulation accuracy. The diagram of a PLL used for FM demodulation is shown in Figure 1.21.

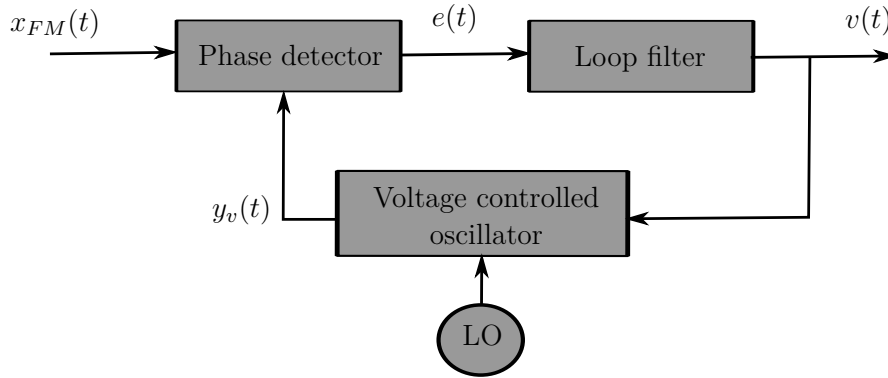


Figure 1.21: Block diagram of PLL used for FM demodulation.

We consider the FM input signal defined in (1.29). The voltage controlled oscillator (VCO) produces a signal $y_v(t)$ whose instantaneous frequency $f_v(t)$ is determined by the voltage $v(t)$ at the input of this VCO

$$f_v(t) = f_c + k_v v(t), \quad (1.34)$$

where k_v is a constant of proportionality and f_c is the carrier frequency adjusted by the local oscillator (LO). The signal $y_v(t)$ can be expressed at the output of the VCO as

$$y_v(t) = A_v \sin(2\pi f_c t + \theta_v(t)), \quad (1.35)$$

where A_v and $\varphi_v(t)$ are the amplitude and the instantaneous phase of the signal at the output of the VCO, respectively.

The function of the phase detector is to calculate the phase shift between the input signal and the VCO output signal. The loop filter removes the high frequencies produced by the phase comparator. The PLL adjusts the instantaneous phase at the VCO output to

the one of the input FM signal so that $\theta_v(t) = \theta(t)$. The output voltage $v(t)$ is then proportional to the modulating signal.

1.4.2.d Phase-shift discrimination

Another category of available FM demodulators is based on the phase-shift discrimination [43, 44]. As exposed in Figure 1.22, the FM modulated signal and its quadrature phase shifted version are multiplied. Then, the signal is low-pass filtered.

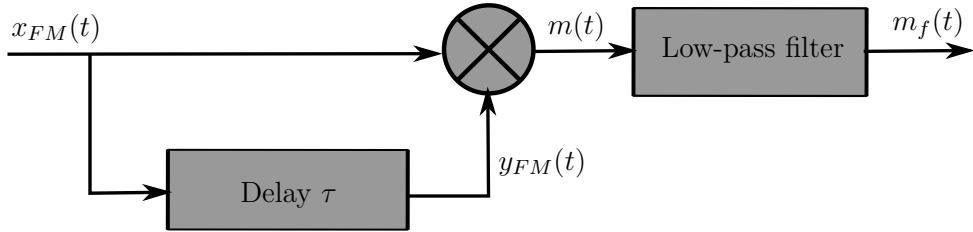


Figure 1.22: Block diagram of phase-shift discriminator.

We consider the input signal defined in (1.29). The frequency of signal $\theta(t)$ must be much smaller than the carrier frequency f_c . The first demodulation step consists in shifting the FM signal by a delay τ which allows to introduce a quadrature phase shift on the cosine argument.

$$\begin{aligned} y_{FM}(t) &= A_c \cos(2\pi f_c(t - \tau) + \theta(t - \tau)) \\ &= A_c \sin(2\pi f_c t + \theta(t - \tau)). \end{aligned} \quad (1.36)$$

The signal can be expressed at the multiplier output as

$$\begin{aligned} m(t) &= A_c^2 \cos(2\pi f_c t + \theta(t)) \sin(2\pi f_c t + \theta(t - \tau)) \\ &= \frac{A_c^2}{2} [\sin(4\pi f_c t + \theta(t) + \theta(t - \tau)) - \sin(\theta(t) - \theta(t - \tau))]. \end{aligned} \quad (1.37)$$

The term around $2f_c$ frequency is eliminated by the low-pass filtering. Thus, the produced signal can be expressed as

$$m_f(t) = \frac{-A_c^2}{2} \sin(\theta(t) - \theta(t - \tau)). \quad (1.38)$$

Since the carrier has fast variations compared to $\theta(t)$, the delay τ can be chosen short compared to the period of the signal constituting $\theta(t) - \theta(t - \tau)$ so that

$$\begin{aligned} \sin(\theta(t) - \theta(t - \tau)) &\approx \theta(t) - \theta(t - \tau) \\ &\approx \tau \dot{\theta} \left(t - \frac{\tau}{2} \right). \end{aligned} \quad (1.39)$$

Thus, we can express the demodulated signal as

$$m_f(t) = -\tau \frac{A_c^2}{2} \dot{\theta} \left(t - \frac{\tau}{2} \right). \quad (1.40)$$

1.4.3 Phase comparison

The azimuth information represents the phase difference between the REF and VAR 30 Hz signals. To extract this information, a phase comparator is applied at the output of REF and VAR channel. The simplest phase comparator model consists of a multiplier (with gain k) and a low-pass filter, as shown in Figure 1.23 [37].

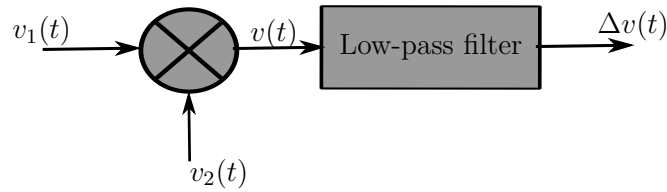


Figure 1.23: Phase comparator "the multiplier".

We consider two sinusoidal signals of the same frequency f_{LF} which are expressed as follows

$$\begin{aligned} v_1(t) &= V_{1M} \cos(2\pi f_{LF}t + \theta_1), \\ v_2(t) &= V_{2M} \cos(2\pi f_{LF}t + \theta_2). \end{aligned} \quad (1.41)$$

The input signals are characterized by their amplitudes V_{1M} and V_{2M} and their initial phases θ_1 and θ_2 , respectively. $v_1(t)$ and $v_2(t)$ are multiplied. This provides the output voltage $v(t)$ expressed as

$$\begin{aligned} v(t) &= kV_{1M}V_{2M} \cos(2\pi f_{LF}t + \theta_1) \cos(2\pi f_{LF}t + \theta_2) \\ &= \frac{kV_{1M}V_{2M}}{2} [\cos(4\pi f_{LF}t + \theta_1 + \theta_2) + \cos(\theta_1 - \theta_2)]. \end{aligned} \quad (1.42)$$

The low-pass filter placed at the output of the multiplier allows to remove the term around the $2f_{LF}$ frequency. Hence, we have

$$\Delta v(t) = \frac{kV_{1M}V_{2M}}{2} \cos(\theta_1 - \theta_2). \quad (1.43)$$

We then obtain a signal which is a function of the phase shift between $v_1(t)$ and $v_2(t)$. The phase shift is obtained on $[0, \pi]$. It is possible to modify this phase detector using complex numbers so that the estimated phase can be in the range $[-\pi, \pi]$, as explained in Section 2.3.3.e.

1.5 Odunaiya VOR error expressions

For the standard architecture of VOR receivers presented in the previous section, it is possible to analytically estimate the VOR error by considering the receiver components as ideal [3]. The CVOR and DVOR errors are then computed from the multipath characteristics using (1.27) and (1.28). The demonstrations of these expressions are detailed in Appendix A. The formulation of the Doppler error is only valid for weak multipath. Figure 1.24 shows the evolution of CVOR and DVOR errors for multipath of relative amplitude $a_1/a_0 = 0.01$, according to its relative azimuth and phase.

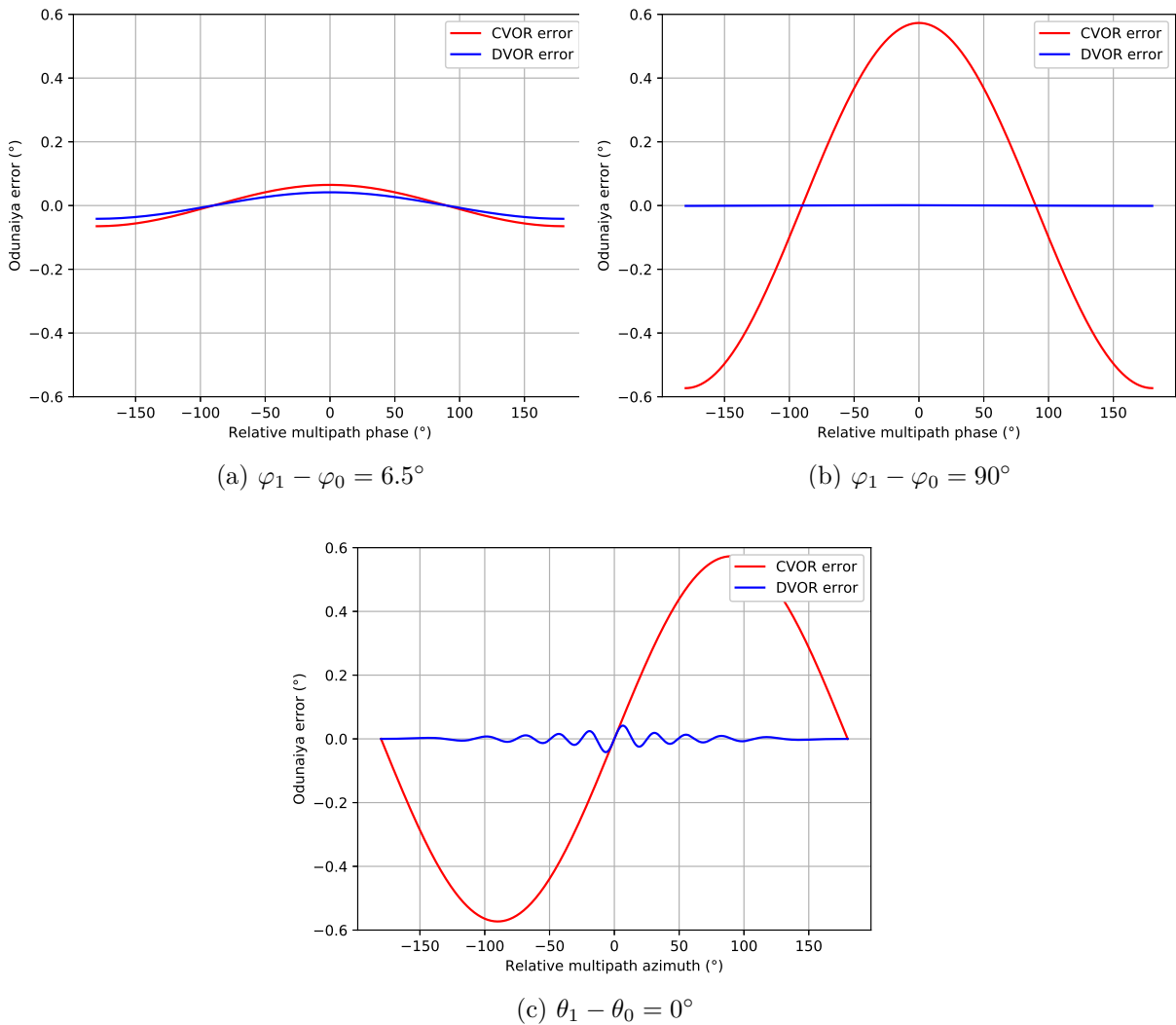


Figure 1.24: Evolution of CVOR and DVOR errors according to the relative azimuth and phase of weak multipath.

Firstly, we can analyze from Figures 1.24a and 1.24b the impact of the relative multipath phase on the error. The CVOR and DVOR errors are maximum in magnitude when the

multipath and direct signal are in phase or in phase opposition. Besides, the error is zero when they are in phase quadrature.

Secondly, from Figure 1.24c, we can analyze the impact of the relative multipath azimuth. The errors are equal to zero when the relative multipath azimuth tends to 0 or $\pm 180^\circ$. We observe that the maximums of both errors do not correspond to the same value of the relative multipath azimuth: $\pm 90^\circ$ for CVOR and $\pm 6.5^\circ$ for DVOR, respectively.

Thirdly, the DVOR error is typically 10 times smaller than the CVOR error. The azimuth information is modulated in frequency for the DVOR while it is modulated in amplitude for the CVOR. Therefore, DVOR is more robust against the multipath effect than CVOR.

The limitation of the Odunaiya expressions is that everything is assumed static. In reality, since the aircraft moves, multipath change in time. Thus, filters and response times of the receiver may render the bearing errors estimated by (1.27) and (1.28) inaccurate. Then, one of the aim of this PhD thesis consists in developing a receiver model which can reproduce the response of a VOR receiver when the multipath change in time along a realistic aircraft trajectory. This represents the aim of the next chapter.

1.6 Conclusion

In this chapter, the basic principle of the CVOR and DVOR systems has been presented. The multipath phenomenon generated by the wind turbines in the vicinity of VOR stations has been detailed by presenting its parameters and some associated modeling methods that exist in the literature. An overview of the VOR receivers has been presented by describing the standard structure of a VOR receiver and the signal processing steps such as demodulation, filtering and phase detection to extract the azimuth information. To calculate the VOR error, the analytical expressions proposed by Odunaiya and Quinet for the CVOR and DVOR systems have been given and illustrated. The Odunaiya expressions neglect the variations in time of multipath in the bearing error. Thus, we introduce in the next chapter a dynamic VOR receiver model including filtering and demodulation in order to reproduce the response of a VOR receiver in a realistic way.

Chapter 2

Digital VOR Receiver Model

2.1 Introduction

In this chapter, we present a digital VOR receiver model which can reproduce the response of a VOR receiver on a realistic aircraft trajectory in the presence of multipath changing with time. In Section 2.2, a method for generating time series is described. A sampling criterion is discussed and the studied trajectories are presented. The digital VOR receiver model is presented in Section 2.3 by describing its components. In Section 2.4, an illustration test is exposed from which the effects on the multipath changes in time are analyzed along a realistic trajectory.

2.2 Time series of multipath parameters

The time series allows to give the evolution of multipath change in time along a sampled trajectory. A method for generating and computing the time series is presented in this section.

2.2.1 Sampling criterion

To obtain time series, a realistic aircraft trajectory is sampled using a constant time step. A particular attention must be devoted to the choice of this time step. Indeed, to completely capture the signal variations in space, two consecutive samples must be separated by a sufficiently short distance with respect to the wavelength at VHF frequency. Actually, the space step (Δx) must be shorter than half a wavelength according to the Nyquist criterion [45]

$$\Delta x < \frac{\lambda}{2}. \quad (2.1)$$

The time step is expressed in terms of the space step and the maximum speed (V_{\max}) along the trajectory

$$\Delta t_{\min} = \frac{\Delta x}{V_{\max}}. \quad (2.2)$$

We consider an example with typical values: a VOR frequency of 113.8 MHz, a space sampling step equal to $\frac{\lambda}{5}$ ($\simeq 0.526$ m) and a maximum speed of 500 km/h along the trajectory. Using (2.2), the time step should be of order of few milliseconds ($\simeq 3$ ms).

The time sampling criterion is fixed along a defined aircraft trajectory. In the next section, we study the generation of this trajectory.

2.2.2 Aircraft trajectories

In our study, the aircraft trajectory is defined by a series of straight or circular elements. We introduce in this section the generation details of these types of motion.

2.2.2.a Straight motion

We consider an aircraft moving along a straight trajectory. As illustrated in Figure 2.1, the initial position of the aircraft is \mathbf{P}_0 . The trajectory is characterized by a departure speed v_0 , an arrival speed v_1 , a distance D and a direction of movement which is defined by an azimuth φ_m and an elevation ψ_m . A linear speed along the segment (constant acceleration) is considered between \mathbf{P}_0 and the arrival position \mathbf{P}_1 .

Therefore, the position vector of the aircraft at time t is expressed as

$$\mathbf{P}_a(t) = \mathbf{P}_0 + s(t) \hat{\mathbf{s}}_m, \quad (2.3)$$

where $\hat{\mathbf{s}}_m$ is the direction of the aircraft motion, which is defined by

$$\hat{\mathbf{s}}_m = \begin{bmatrix} \cos \psi_m \cos \varphi_m \\ \cos \psi_m \sin \varphi_m \\ \sin \psi_m \end{bmatrix}. \quad (2.4)$$

We consider an uniformly accelerated motion of the aircraft. Therefore, the position $s(t)$ of the aircraft relative to its initial position is defined at time t by

$$s(t) = \frac{1}{2} a_0 t^2 + v_0 t, \quad (2.5)$$

where a_0 is the aircraft acceleration along the trajectory given by

$$a_0 = \frac{v_1 - v_0}{T}, \quad (2.6)$$

where T is the motion duration of the aircraft along the trajectory expressed as

$$T = 2 \frac{D}{v_0 + v_1}. \quad (2.7)$$

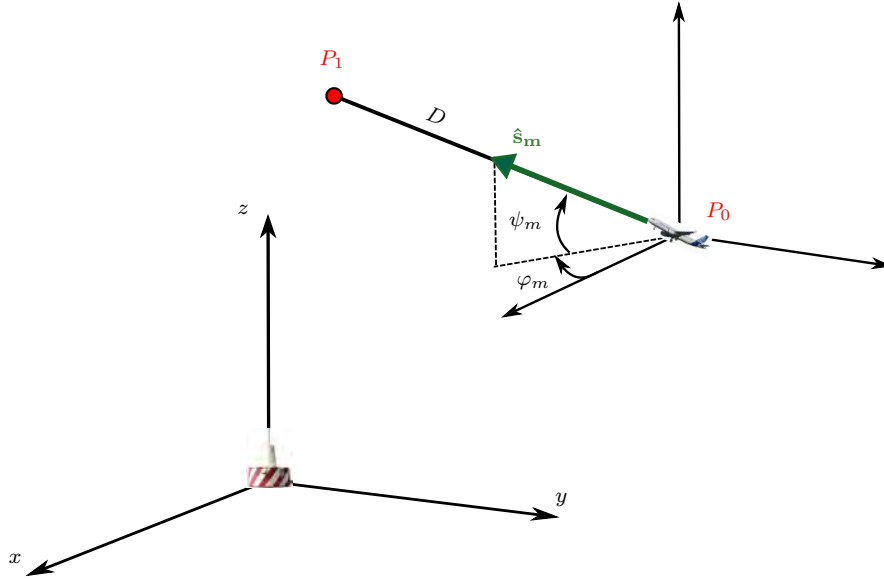


Figure 2.1: Aircraft motion along a straight trajectory.

2.2.2.b Circular motion

We consider an aircraft moving along a circular trajectory. As illustrated in Figure 2.2, the initial position of the aircraft is \mathbf{P}_0 . The trajectory is characterized by a departure speed v_0 , an arrival speed v_1 , a distance D , a radius of curvature R and an initial direction of movement which is defined by an azimuth φ_m and an elevation ψ_m . A linear speed along the segment (constant acceleration) is considered between \mathbf{P}_0 and the arrival position \mathbf{P}_1 .

We consider that the aircraft moves in a plane P defined by two vectors as shown in Figure 2.2: $\hat{\mathbf{s}}_m$ the initial aircraft motion direction and a vector $\hat{\mathbf{u}}_h$ which is perpendicular to $\hat{\mathbf{s}}_m$ and in the horizontal plane. Mathematically, this vector is given by

$$\hat{\mathbf{u}}_h = \frac{\hat{\mathbf{s}}_m \times \hat{\mathbf{z}}}{\|\hat{\mathbf{s}}_m \times \hat{\mathbf{z}}\|}. \quad (2.8)$$

From Figure 2.2, the position vector of the aircraft is expressed at time t as

$$\mathbf{P}_a(\mathbf{t}) = \mathbf{P}_0 + R(\cos(\alpha_t) - 1) \hat{\mathbf{u}}_h + R \sin(\alpha_t) \hat{\mathbf{s}}_m, \quad (2.9)$$

where α_t is the angle between the initial position and the position at time t of the aircraft on its trajectory. This angle is given by

$$\alpha_t = \frac{1}{R} \left(\frac{1}{2} a_0 t^2 + v_0 t \right). \quad (2.10)$$

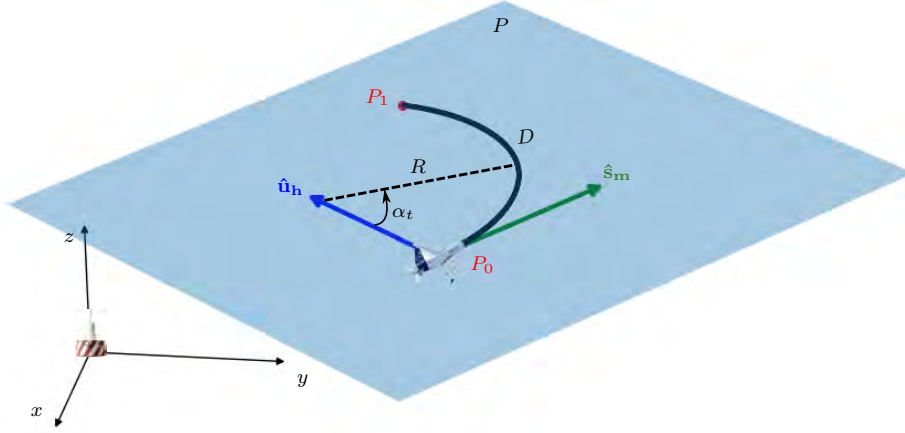


Figure 2.2: Aircraft motion along a circular trajectory.

The time series are generated along the aircraft trajectory. At each epoch, we use the hybridization method of PE with PO in order to compute the multipath parameters. These characteristics will be sent to a digital VOR receiver to assess the influence of the multipath changes in time on the bearing error.

2.3 Digital VOR receiver model

In the literature, the analytic expression proposed by Odunaiya and Quinet [3] is generally used to compute the VOR error from the multipath characteristics. In this expression, everything is expected static. However, multipath change in time as the aircraft moves. Thus, we here propose a digital VOR receiver model to reproduce the dynamic response of a realistic VOR receiver, taking into account demodulations and filtering. In this section, the structure of the proposed model is presented by describing its block elements.

2.3.1 Receiver block diagram

We here propose a digital VOR receiver model to assess the impact of multipath variations in time on the bearing error. Our model is based on a I/Q signal generator from the multipath parameters computed by VERSO simulator. The block diagram of our digital VOR receiver model for CVOR signal is given in Figure 2.3. It should be noted that the receiver model can also process signals of DVOR.

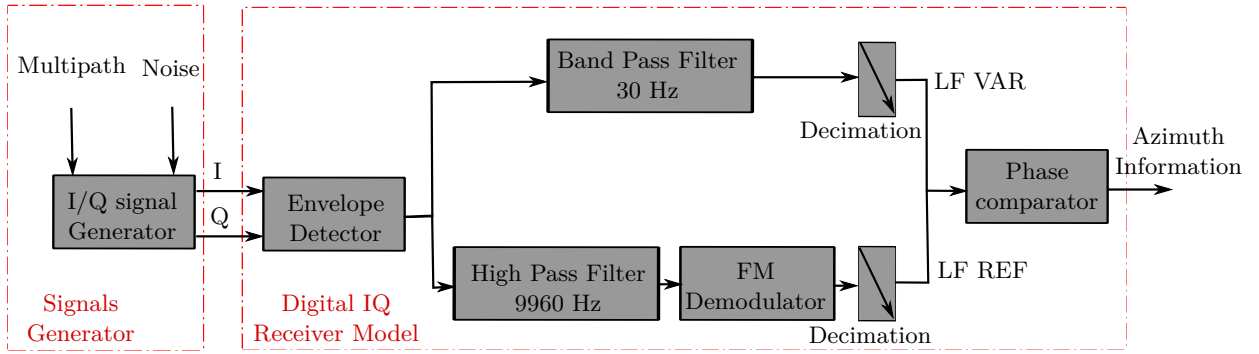


Figure 2.3: Block diagram of the digital VOR receiver model for CVOR (for DVOR, the REF and VAR channels are reversed).

2.3.2 I/Q signal generator

Our model is based on a I/Q signal generator to obtain the data received by a VOR receiver. Its block diagram is shown in Figure 2.4.

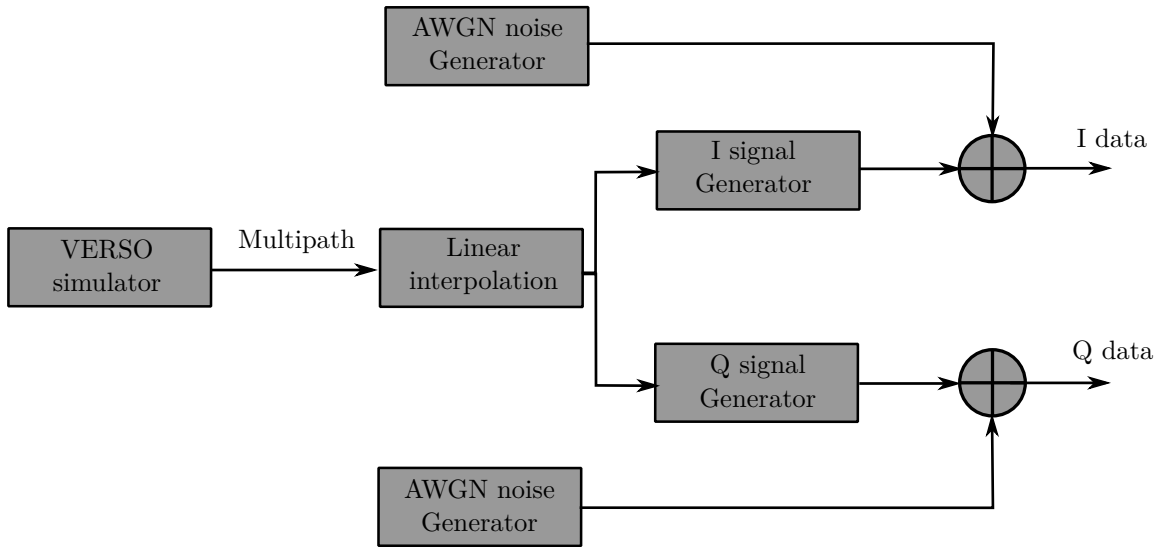


Figure 2.4: Block diagram of the I/Q signal generator.

The sampling frequency for the multipath computation is typically set to few hundreds of Hz using (2.2). Since I/Q baseband signals have a bandwidth of $(f_{sc} + f_{LF}m_f)$, we need in the receiver a sampling frequency of at least $2(f_{sc} + f_{LF}m_f) = 20880$ Hz to respect the Nyquist criterion. Thus, an oversampling must be performed on the multipath parameters. This is done using a linear interpolation. To avoid the effect of phase jumps, this interpolation is performed on the unwrapped phase.

In order to model the noise detected at the input of the receiver model, an Additive White Gaussian Noise (AWGN) is added to the I/Q signals. This noise can be characterized by an equivalent temperature T_e . Its power is defined by

$$P_{\text{noise}} = k_B T_e B, \quad (2.11)$$

where k_B is the Boltzmann constant ($= 1.38 \cdot 10^{-23}$ J/K) and B is the VOR bandwidth.

We can also define an AWGN noise in the I/Q signal generator from the Signal to Noise Ratio (SNR) given by

$$\text{SNR}_{\text{dB}} = 10 \log_{10} \left(\frac{P_{\text{signal}}}{P_{\text{noise}}} \right), \quad (2.12)$$

where P_{signal} is the power of the received VOR signal.

After interpolating the multipath parameters and generating the AWGN noise, the I/Q signals are defined by

$$I(t) = \sum_{n=0}^N M_n(t) \cos(\theta_n(t)) + \eta_I(t), \quad (2.13)$$

$$Q(t) = \sum_{n=0}^N M_n(t) \sin(\theta_n(t)) + \eta_Q(t), \quad (2.14)$$

where $\eta_I(t)$ and $\eta_Q(t)$ are the AWGN noises associated to the I/Q signals, respectively. $M_n(t)$ is the n^{th} multipath signal, which is defined by

$$M_n(t) = a_n(t)[1 + m_a \cos(2\pi f_{sc}t + m_f \sin(2\pi f_{LF}t)) + m_a \cos(2\pi f_{LF}t - \varphi_n)] \quad (2.15)$$

for CVOR, and

$$M_n(t) = a_n(t)[1 + m_a \cos(2\pi f_{sc}t + m_f \sin(2\pi f_{LF}t - \varphi_n)) + m_a \cos(2\pi f_{LF}t)] \quad (2.16)$$

for DVOR.

2.3.3 Receiver simulator

Once the I/Q signals are generated, they are transmitted to the receiving unit to extract the azimuth information. This section describes the demodulation and filtering steps applied in the proposed digital VOR receiver model.

2.3.3.a Envelope detection

The envelope detector carries out an AM demodulation in order to recover the VAR and REF signals. The complex envelope is defined by

$$A(t) = \sqrt{I^2(t) + Q^2(t)}. \quad (2.17)$$

In order to extract separately the VAR and REF signals, dedicated filterings are applied on the complex envelope.

2.3.3.b Complex envelope filtering

The filtering is an essential step to identify the VAR and REF signals at the AM demodulator output. For CVOR, a band-pass filter is used to extract the variable signal at 30 Hz and a high-pass filter is applied to obtain the reference signal at 9960 Hz. Figure 2.5 shows the pattern of these filters and illustrates all their parameters *i.e.* the positions of the transition bands and the pass-band and stop-band ripples. The 3 dB bandwidths of the 30 Hz band-pass filter and the 9960 Hz high-pass are noted by W_{30} and W_{9960} , respectively.

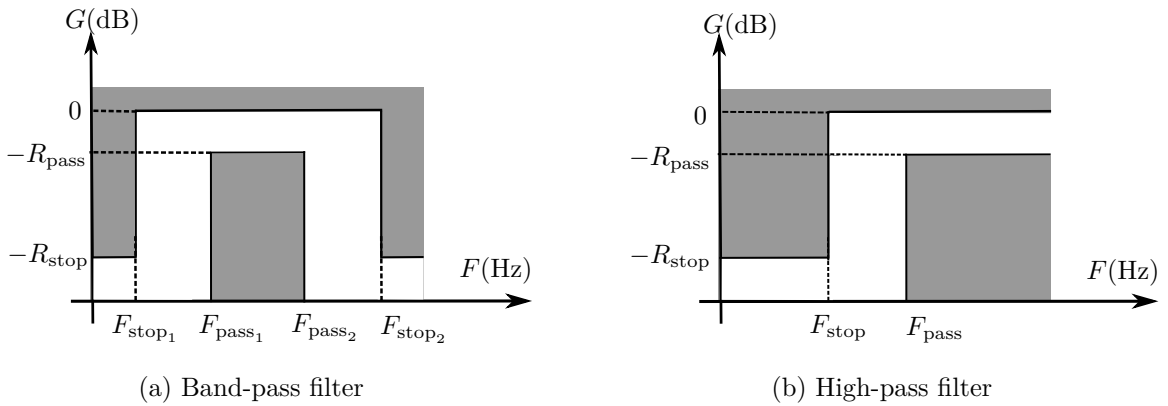


Figure 2.5: Patterns of the applied filters in the VOR receiver model.

The REF signal at the high-pass filter output is modulated in frequency at 9960 Hz. In order to extract the REF signal at 30 Hz, a FM demodulator, which is presented in the next section, is applied.

2.3.3.c FM demodulation

We propose the phase-shift discriminator presented in Section 1.4.2.d in order to extract the REF signal at 30 Hz. Figure 2.6 shows the block diagram of the proposed FM demodulator.

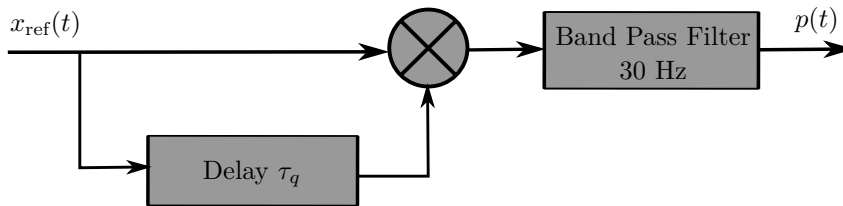


Figure 2.6: Block diagram of the FM demodulator.

We here explain in details how this FM demodulator works. We consider the REF signal of CVOR at the FM demodulator input. From (1.3), this signal is given by

$$x_{\text{ref}}(t) = A_0 \cos(2\pi f_{sc}t + \phi_{LF}(t)), \quad (2.18)$$

with $\phi_{LF}(t) = m_f \sin(2\pi f_{LF}t)$ and $A_0 = m_a a_0$.

The first demodulation step consists in introducing a replica of the REF signal with a quadrature delay. We need to find an integer q such that

$$2\pi f_{sc} \frac{q}{F_s} = 2\pi f_{sc} \tau_q = \frac{\pi}{2}[\pi] + \varepsilon, \quad (2.19)$$

where ε , the quadrature phase shift error should be as small as possible. The second operation is to multiply the reference signal with its delayed replica. This yields

$$\begin{aligned} p(t) &= x_{\text{ref}}(t) x_{\text{ref}}(t - \tau_q) \\ &= A_0^2 \cos(2\pi f_{sc}t + \phi_{LF}(t)) \cos(2\pi f_{sc}(t - \tau_q) + \phi_{LF}(t - \tau_q)) \\ &= \frac{A_0^2}{2} [\cos(4\pi f_{sc}t - 2\pi f_{sc}\tau_q + \phi_{LF}(t) + \phi_{LF}(t - \tau_q)) \\ &\quad + \cos(2\pi f_{sc}\tau_q + \phi_{LF}(t) - \phi_{LF}(t - \tau_q))]. \end{aligned} \quad (2.20)$$

The term around the frequency $2f_{sc}$ is eliminated by band-pass filtering. Thus, after filtering, we have

$$\begin{aligned} p(t) &= \frac{A_0^2}{2} \cos(2\pi f_{sc}\tau_q + \phi_{LF}(t) - \phi_{LF}(t - \tau_q)) \\ &= \frac{A_0^2}{2} [\cos(2\pi f_{sc}\tau_q) \cos(\delta\phi_{LF}) - \sin(2\pi f_{sc}\tau_q) \sin(\delta\phi_{LF})], \end{aligned} \quad (2.21)$$

where $\delta\phi_{LF} = \phi_{LF}(t) - \phi_{LF}(t - \tau_q)$. τ_q is taken small compared to the 30 Hz signal period constituting $\phi_{LF}(t)$. Therefore, we can perform the following simplifications

$$\begin{aligned} \cos(\delta\phi_{LF}) &\simeq 1 \\ \sin(\delta\phi_{LF}) &\simeq \delta\phi_{LF} \\ \frac{\delta\phi_{LF}}{\tau_q} &\simeq \dot{\phi}_{LF} \left(t - \frac{\tau_q}{2} \right). \end{aligned} \quad (2.22)$$

If ε is small enough in (2.19), we can write

$$\begin{aligned} \cos(2\pi f_{sc}\tau_q) &= -\sin(\varepsilon) \simeq -\varepsilon \\ \sin(2\pi f_{sc}\tau_q) &= \cos(\varepsilon) \simeq 1. \end{aligned} \quad (2.23)$$

We include the simplifications (2.22) and (2.23) in (2.21). The signal at the output of the FM demodulator is expressed as

$$p(t) = \frac{-A_0^2}{2} \left[\varepsilon + \tau_q \dot{\phi}_{LF} \left(t - \frac{\tau_q}{2} \right) \right]. \quad (2.24)$$

We observe that the signal in (2.24) is the demodulated signal since it is proportional to the derivative of the signal ϕ_{LF} if ε is small. A more detailed study based on Taylor series is given in Appendix B.

2.3.3.d Decimation

At the output of the REF and VAR channels, only signals at LF (30 Hz) should remain. Thus, a decimation operation is applied in order to reduce the computation time. This downsampling step consists in keeping a number of samples of VAR and REF signals as small as possible to fulfill the Nyquist criterion at 30 Hz. The decimated data are sent to the phase comparator in order to extract the azimuth information.

2.3.3.e Phase comparison

The phase comparator calculates the phase difference between the VAR and REF LF (30 Hz) signals. We propose a modified version of the phase comparator model studied in Section 1.4.3. Figure 2.7 shows the block diagram of our proposed model.

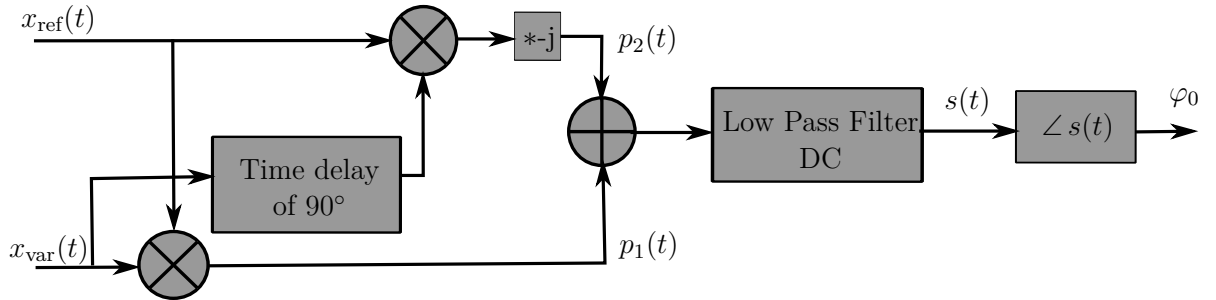


Figure 2.7: Block diagram of the phase detector.

We consider the input LF VAR and REF signals

$$\begin{aligned} x_{\text{var}}(t) &= A_{\text{var}} \cos(2\pi f_{LF}t - \varphi_0), \\ x_{\text{ref}}(t) &= A_{\text{ref}} \cos(2\pi f_{LF}t), \end{aligned} \quad (2.25)$$

where φ_0 is the azimuth information, A_{var} and A_{ref} are the amplitudes of the VAR and REF signals, respectively.

The first product is performed between the REF and VAR signals, it is defined by

$$\begin{aligned}
p_1(t) &= x_{\text{var}}(t)x_{\text{ref}}(t) \\
&= A_{\text{var}}A_{\text{ref}}\cos(2\pi f_{LF}t - \varphi_0)\cos(2\pi f_{LF}t) \\
&= \frac{A_{\text{var}}A_{\text{ref}}}{2}[\cos(4\pi f_{LF}t - \varphi_0) + \cos(\varphi_0)].
\end{aligned} \tag{2.26}$$

We introduce a replica of the VAR signal with a quadrature delay. We need to find an integer m such that

$$2\pi f_{LF} \frac{m}{F_s} = 2\pi f_{LF} \tau_m = \frac{\pi}{2}[\pi] + \alpha, \tag{2.27}$$

where α is the quadrature phase shift error should be as small as possible. In order to simplify the calculation, α is considered zero. The delayed replica of the VAR signal is then given by

$$\begin{aligned}
x_{\text{var}}^{\text{delay}}(t) &= x_{\text{var}}(t - \tau_m) \\
&= A_{\text{var}}\cos(2\pi f_{LF}(t - \tau_m) - \varphi_0) \\
&= A_{\text{var}}\cos(2\pi f_{LF}t - 2\pi f_{LF}\tau_m - \varphi_0) \\
&= A_{\text{var}}\sin(2\pi f_{LF}t - \varphi_0).
\end{aligned} \tag{2.28}$$

A second product is performed between the REF signal and the delayed replica of the VAR signal. After multiplication by $-j$, a purely imaginary number is obtained, which is given by

$$\begin{aligned}
p_2(t) &= -j x_{\text{var}}^{\text{delay}}(t)x_{\text{ref}}(t) \\
&= -j A_{\text{var}}A_{\text{ref}}\sin(2\pi f_{LF}t - \varphi_0)\cos(2\pi f_{LF}t) \\
&= -j \frac{A_{\text{var}}A_{\text{ref}}}{2}[\sin(4\pi f_{LF}t - \varphi_0) + \sin(-\varphi_0)].
\end{aligned} \tag{2.29}$$

The next operation consists in adding $p_1(t)$ and $p_2(t)$ and performing a low-pass filtering in order to eliminate the term located around $2f_{LF}$. The 3 dB bandwidth of the DC low-pass filter is noted by W_{DC} . This yields

$$s(t) = \frac{A_{\text{var}}A_{\text{ref}}}{2}[\cos(\varphi_0) + j\sin(\varphi_0)]. \tag{2.30}$$

Finally, the azimuth is assessed by computing the argument of $s(t)$, *i.e.*

$$\varphi_0 = \angle s(t). \tag{2.31}$$

2.3.3.f Filtering choices

For the 30 Hz band-pass and DC low-pass filtering, we use filters of type IIR (Infinite Impulse Response) because this type of filters requires a lower number of coefficients than

the filters of type FIR (Finite Impulse Response). We want a maximum flat frequency response in the pass-band of the IIR filters. Thus, we apply Butterworth filters [46]. For the 9960 Hz high-filter, the FIR filtering shows less ripples in the pass-band compared to the IIR filtering. The Kaiser window is preferred because it requires a minimum number of coefficients and has no ripples in the pass-band [47] compared to other types such as Hamming, Blackman, rectangular, etc.

2.4 Illustration test

In the previous section, our digital VOR receiver model has been presented by describing the demodulation and filtering steps in order to extract the azimuth information. This section introduces a simulation test with our receiver model and with the Odunaiya expression to analyze the multipath changes in time.

2.4.1 Configuration and parameters

We consider a CVOR station operating at a frequency of 113.8 MHz with a power of 50 W. A wind turbine of type ENERCON E82 is placed at 1 km from the VOR station, which should yield one multipath. To simplify the analysis, a straight trajectory of 6 km is considered here. Firstly, the aircraft is motionless for 5 s to ensure the end of the receiver transient period. Then, it starts at low speed until reaching the second waypoint at 180 km/h. The configuration is shown in Figure 2.8.

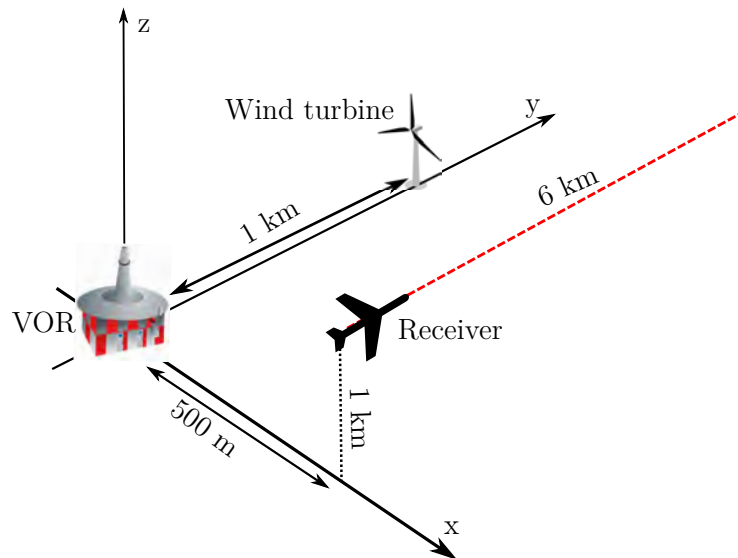


Figure 2.8: Proposed configuration for the illustration test.

The multipath parameters are interpolated at a frequency of 25 kHz in the I/Q signal generator. To focus on the effect of the multipath, no additional noise is considered.

The filtering parameters of our digital I/Q receiver model are given in Table 2.1. The characteristics of the filters are expressed in terms of the attenuation patterns given in Figure 2.5.

Input parameters					
	Type	F_{pass} (Hz)	F_{stop} (Hz)	R_{pass} (dB)	R_{stop} (dB)
Band-pass filter 30 Hz	IIR Butterworth	[29,31]	[24,36]	0.1	30
Low-pass filter DC	IIR Butterworth	1	2	0.1	20
High-pass filter 9960 Hz	FIR Kaiser	8000	7000	N/A	60
Filter characteristics					
	Cutoff frequency (Hz)			Order	
Band-pass filter 30 Hz	31.74			9	
Low-pass filter DC	1.43			5	
High-pass filter 9960 Hz	7795.14			15	

Table 2.1: Parameters of the filters in the receiver model used for the illustration test.

2.4.2 Results

In Figure 2.9, the power azimuth profile is displayed. This corresponds to the azimuth of the multipath plotted with respect to time and with a color that indicates the power of the multipath relatively to the direct path.

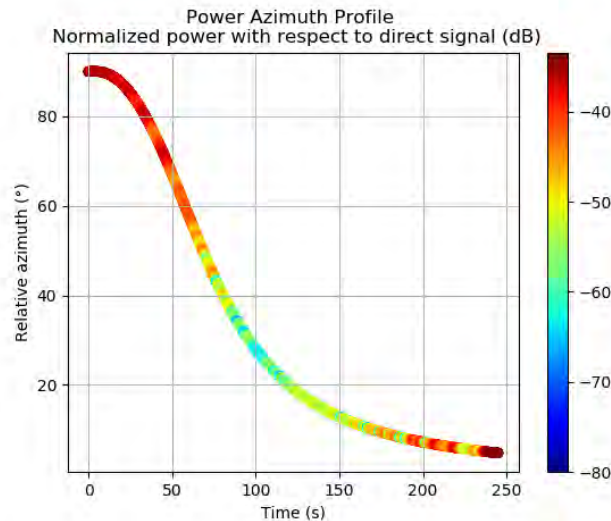
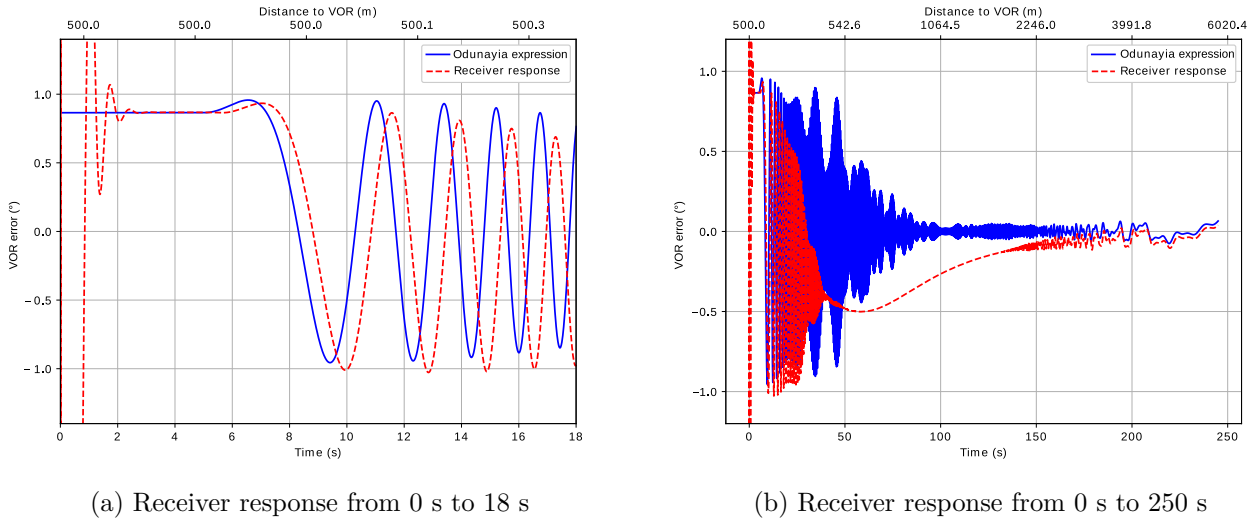


Figure 2.9: Relative Power Azimuth Profile (dB) of the multipath along the trajectory.

As expected, we observe one single multipath. This multipath is powerful during the first part of the trajectory from 0 s to 50 s and during the last part from 200 s to 250 s. This is when the aircraft is in the specular reflection zone of the wind turbine.

In Figures 2.10a and 2.10b, we display the VOR errors obtained with the Odunaiya expression and with the digital VOR receiver model using 2 time scales.



(a) Receiver response from 0 s to 18 s

(b) Receiver response from 0 s to 250 s

Figure 2.10: Receiver response along the trajectory.

From Figure 2.10a, the receiver response rapidly changes during the first 2 seconds. It is due to the receiver transient period. The receiver response converges to the one of Odunaiya during 5 s when no dynamic effects are involved.

From 7 s, the aircraft moves slowly and the receiver response remains close to the static response of Odunaiya. During this phase, there is a delay between both models that is due to the receiver group delay. When the aircraft accelerates, both models do not give the same response (from 25 s to 150 s in Figure 2.10b). This is due to the fast variation of multipath. This phenomenon is explained in Section 4.3. When the aircraft moves at a larger distance from the VOR and the wind turbine, the phase difference between the direct and the multipath changes in a slower way, which explains the slower fluctuations of the VOR error. Hence, the static response converges again to the dynamic model despite the high speed of the aircraft.

We have observed that Odunaiya expression does not always give the same response compared to our digital receiver model. Therefore, a comparison between our digital VOR receiver model and a calibration receiver is useful to further analyze this result. This will be the aim of the next chapter.

2.5 Conclusion

In this chapter, a time series generator along a realistic aircraft trajectory which is defined by straight and circular sections has been presented. A sampling criterion has also been proposed to be sure to capture all the multipath variations in time and space. The digital VOR receiver model has been detailed by describing its components. In order to analyze the effect of multipath dynamics on the VOR receiver, an illustration test has been given by comparing the receiver model response with the Odunaiya expression.

Chapter 3

Analysis of CVOR Multipath from Laboratory Measurements

3.1 Introduction

In the previous chapter, our digital IQ receiver model has been presented and tested for a time variant configuration. In this chapter, we show that the model can reproduce the response of a VOR receiver in a realistic way. To do so, we compare the receiver model with a real receiver, here a calibration receiver used by Air Navigation Service Provider (ANSP) to test VOR beacons. We perform two types of laboratory measurements in order to analyze the response of our digital IQ receiver model for a conventional VOR signal. The first one is realized in the VHF frequency band for one canonical multipath. The second one is realized using baseband IQ signals in a complex scenario.

In Section 3.2, we present the difficulty to compare simulation results with available in-flight measurements. The confrontation results from VHF measurements is given in Section 3.3. We present in Section 3.4 the confrontation results from baseband IQ measurements.

3.2 Analysis of available in-flight measurements: difficulty and limitations

In order to analyse the behavior of a simulation VOR receiver, a comparison can be performed between its response and an available record of in-flight measurements. We show in this section the limitations of this approach when the measurements were not specifically realized for assessing multipath.

In Section 3.2.1, we present the campaign of the proposed in-flight measurement to be studied here. In Section 3.2.2, the results are illustrated and analyzed. The differences between the simulation and measurement results are explained in Section 3.2.3. A con-

clusion is given in Section 3.2.4 by presenting some solutions which can be envisaged to overcome the difficulty to compare simulation results with available measurements.

3.2.1 Configuration

We focus here on a measurement campaign performed by DGAC/DTI. The case of the wind farm located in Boulogne-sur-Mer (France) is studied. As shown in Figure 3.1, the scenario is composed by 9 wind turbines (yellow circles) of type ENERCON E-70 located at 5 km from the conventional VOR of Boulogne-sur-Mer operating at a frequency of 113.8 MHz. These wind turbines are composed by a mast modelled by a metallic conical section (ground diameter = 7.5 m, top diameter = 2 m, height = 98 m), a nacelle modelled by a metallic rectangular box (4 m \times 11 m \times 4 m), and 3 blades modelled by two parallel dielectric slabs (length = 35.5 m, thickness = 43.98 mm, $\epsilon_r = 5$).

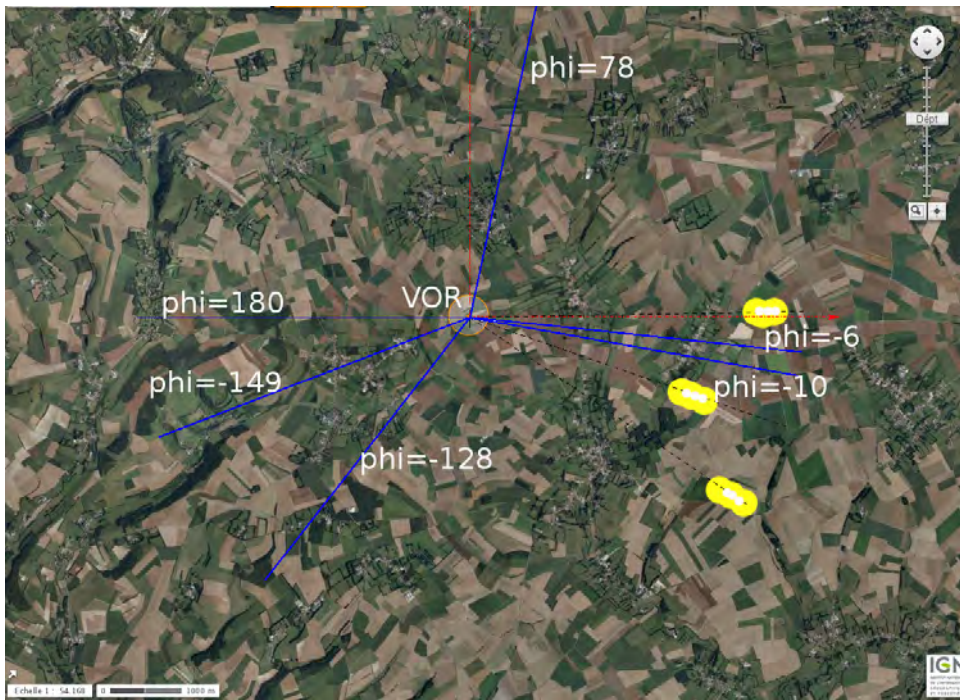


Figure 3.1: Wind farm located at 5 km from the CVOR station in Boulogne-sur-Mer [10].

The measurement campaign has been carried out on 6 radials and at three different times corresponding to three configurations: without wind turbines, with only the masts and with the complete wind turbines. In the PhD thesis work of Claudepierre [9], this configuration has been simulated. We focus on the radials -6° and -10° .

The relief between the VOR antenna and the wind turbines grouped in three different azimuths (-1° , -22° and -40°) is taken into account in the simulations. Its profile relative to the VOR station altitude (considered zero) is shown in Figure 3.2. The ground is considered as humid with characteristics of $\epsilon_r = 25$ and $\sigma = 0.02$ S/m.

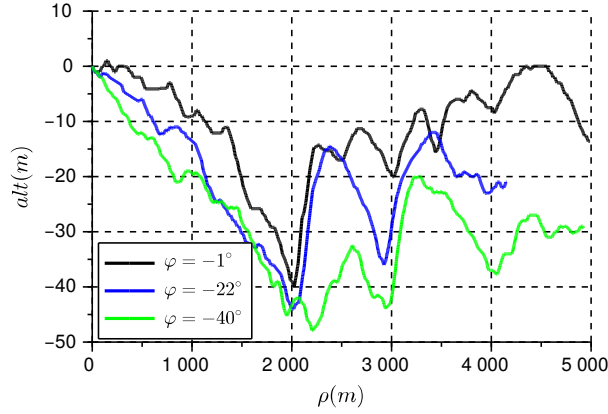


Figure 3.2: Relief profile from the VOR station to the wind turbines placed in three different azimuths [10].

The flight trajectories are given by an onboard GPS receiver. The altitude and the azimuth of the aircraft with respect to the distance from the VOR on each radial are plotted in Figures 3.3 and 3.4.

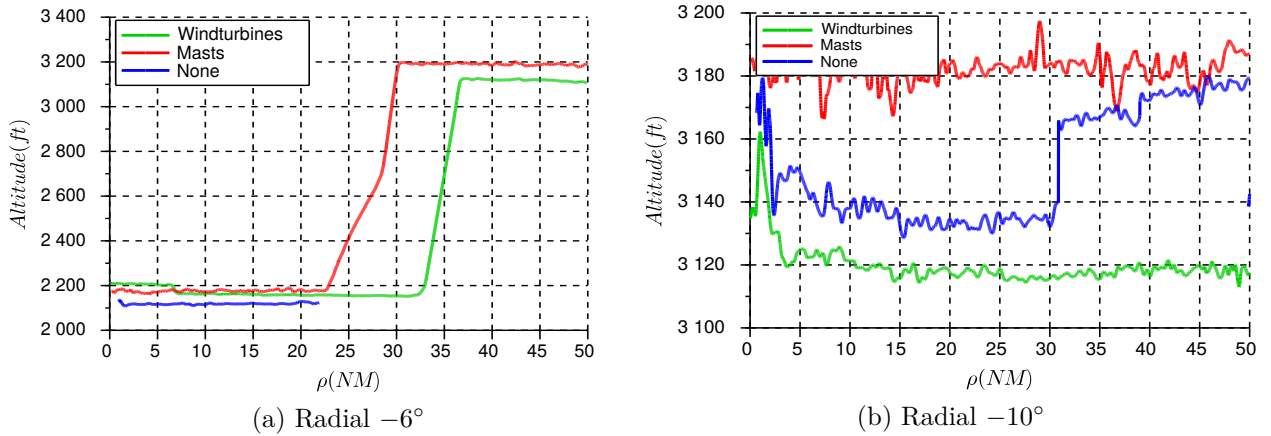


Figure 3.3: Altitudes of the aircraft for the three measurement configurations [10].

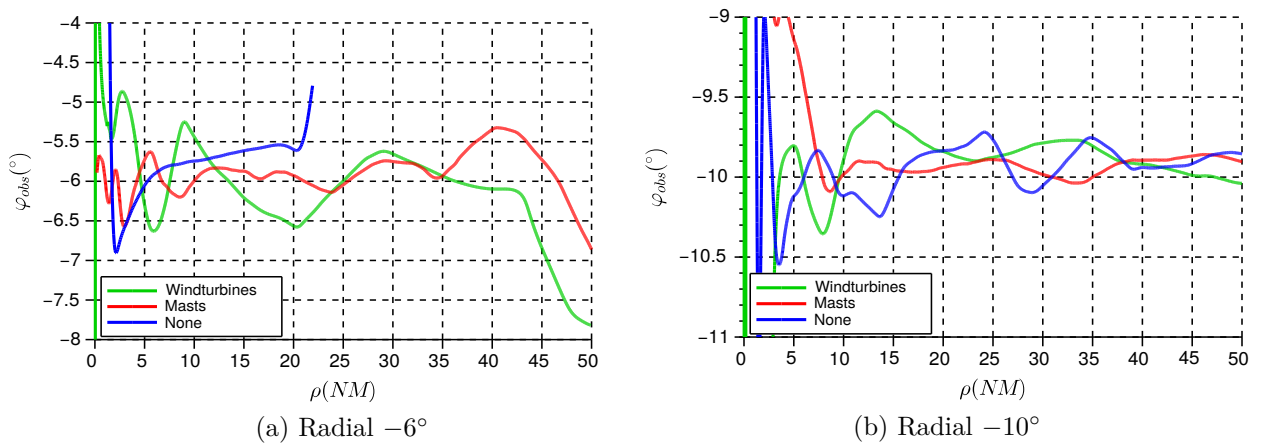


Figure 3.4: Azimuths of the aircraft for the three measurement configurations [10].

3.2.2 Results

We here present the simulation and measurement results for the radials -6° and -10° . We illustrate in Figure 3.5 the measured VOR errors for the three measurement campaigns. It can be observed that the error due to the environment (without the 9 wind turbines) reaches 1° on both radials -6° and -10° . This residual error can be due to other obstacles around the VOR. Indeed, there are 45 other wind turbines located at distances shorter than 15 km from the VOR and a high voltage line in the East of the wind farm.

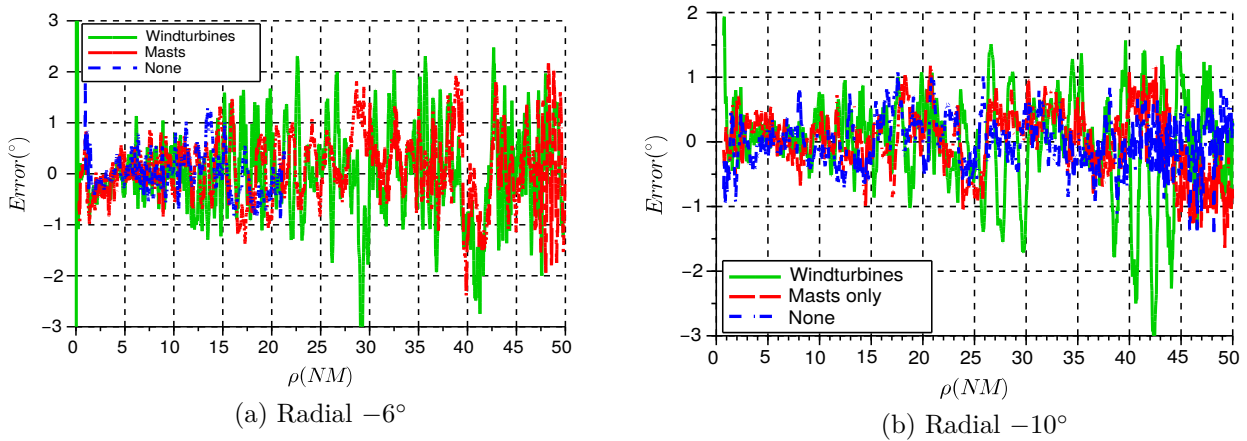


Figure 3.5: Measured VOR error for the three measurement campaigns [10].

The simulated and measured VOR errors in the presence of the wind turbines are plotted in Figure 3.6 with respect to the distance from the VOR. It can be seen that the simulation successfully reproduces the envelope and the oscillations period of the measured error. However, we observe that it is difficult to recover all the oscillations of the measured error for both simulations.

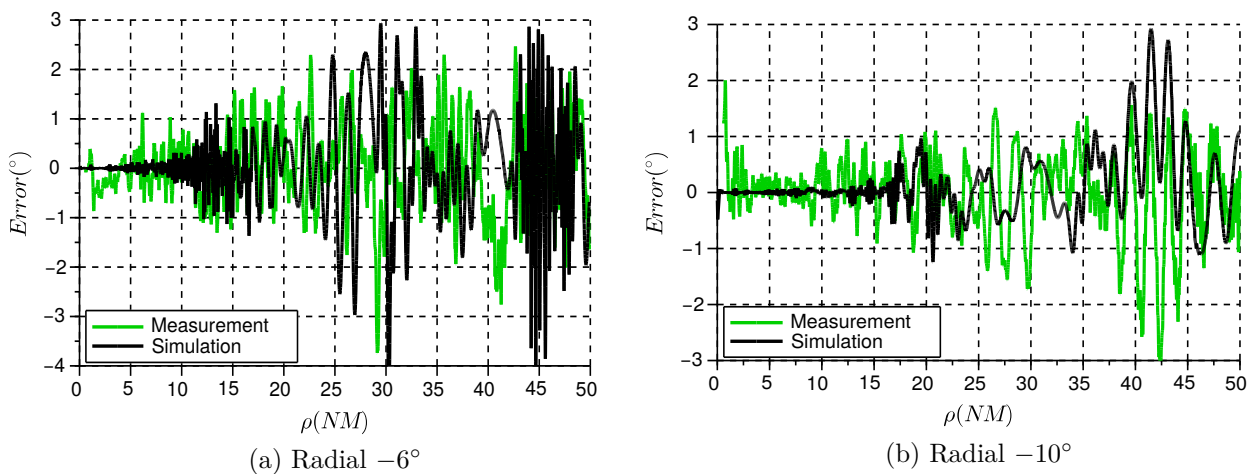


Figure 3.6: Simulated and measured VOR errors in the presence of the wind turbines [10].

The comparison of results is quantified by their statistical characteristics: maximum value, mean and standard deviation. These characteristics are computed and given in Table 3.1. The maximum of the simulated errors for both radials are of the same order of magnitude. The difference between measurements and simulations does not exceed 0.8° . According to the values of the means and the standard deviations, we can observe that the statistical behavior of the measurements is well reproduced by our simulations.

	Radial -6°		Radial -10°	
	Measurement	Simulation	Measurement	Simulation
Max. ($^\circ$)	3.52	4.25	3.01	2.8
Mean ($^\circ$)	0.08	0.05	0.06	0.04
Std dev. ($^\circ$)	0.83	1.13	0.67	0.56

Table 3.1: Moments of the simulated and measured errors.

3.2.3 Explanation of the differences between the simulation and measurement results

The inaccuracies between the simulation and the measurements results can be due to the relief not considered between the wind turbines and the observation points. They are most likely due to the inaccuracies in the positions. A slight change in aircraft trajectory or wind turbines positions significantly changes the multipath phase. The error can then be significantly impacted as well. This is due to the high dependence of the VOR error on the multipath phase.

Figure 3.7 shows the simulated error due to the wind turbines for two slightly different trajectories along radial -10° . These results show that slight variations in the trajectory have a significant influence on the VOR error.

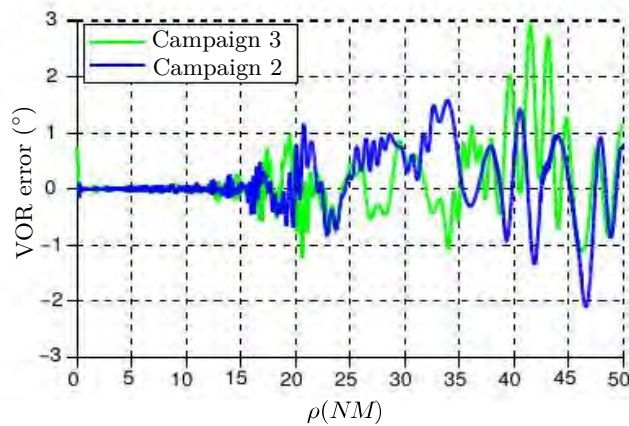


Figure 3.7: Simulated error due to the wind turbines for two slightly different trajectories along radial -10° .

Furthermore, the complex combination of multipath with various phases and Doppler

shifts generated by the aircraft motion in relation to the VOR and the wind turbines positions can affect the response of the receiver.

3.2.4 Conclusion

In this section, the comparisons of available measurements with simulation results have been presented. This corresponds to results obtained by Claudepierre in his PhD thesis. We have seen that the general properties of the errors obtained in measurements and simulations are consistent. Maximal values, means and standard deviations are notably similar. Nevertheless, available measurements concern situations for which the wind turbines respects DGAC setting criteria. This means that, in available measurements, the wind turbines yield acceptable bearing errors, typically of the same order as other sources of errors. Thus, wind turbines are not the only contributors to the bearing error. Besides, the error is very sensitive to uncertainties in the scenario, notably the aircraft trajectory.

This shows the difficulty to compare simulation results with available measurements. Two solutions could be envisaged to overcome this issue. A first solution consists in implementing a configuration in which the wind turbine error is predominant. This can be performed with a specific measurement campaign, probably with a mobile VOR placed nearby wind turbines, which is outside the scope of this thesis. A second solution is to carry out laboratory measurements in a controlled environment. This is performed here.

3.3 Confrontation from VHF measurements

The objective of this section is to compare by means of measurements the digital VOR receiver model with a calibration receiver, the Rhode & Schwarz EVS300 by processing VHF signals in presence of a canonical multipath. We here describe the measurement campaign. The confrontation results are then illustrated and analyzed.

3.3.1 Description

Figure 3.8 shows the configuration of our measurement campaign. A direct signal and a canonical multipath are generated. The combination of these signals is sent to a calibration VOR receiver via its RF input and to the digital VOR receiver model via a digital IQ detector to estimate the bearing error.

- **Generation of VOR signals**

The simplest solution would be to use two VOR signal generators, *e.g.* Rhode & Schwarz SMA100, to generate the direct and multipath signals. However, with this solution the phases of both REF and VAR signals would not be fully synchronised. Alternatively, we propose to use two baseband signal generators here two HP 8904A in order to generate the direct and multipath signals in baseband with controllable phase. Two SMA100 are then used as VHF signal modulators.

- **Combination/Splitting of VHF signals**

The direct signal and the multipath are combined by means of a power combiner of type ZFSC-2-5. The same device is used as a splitter.

- **Analog to IQ digital converter**

In order to send the VHF signal to our IQ receiver model, we need an interface to convert VHF signals into baseband IQ signals. A TNT-SDR dongle of type Nooelec R820T2 is used. This device is characterized by a frequency bandwidth of 25-1700 MHz and a maximum sample rate of 3.2 MHz.

- **Azimuth measurement**

The combination of the direct signal and the canonical multipath is sent to the calibration receiver EVS300 via its RF input and to the digital IQ receiver model in order to estimate the bearing errors. The results are then displayed and compared.

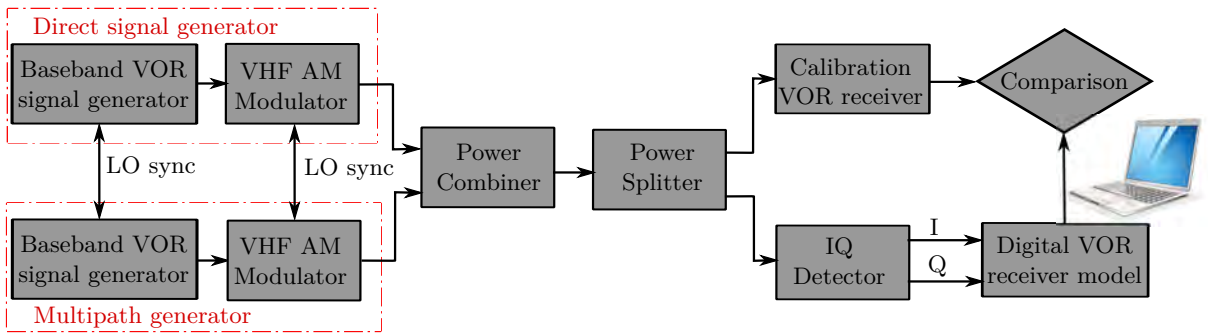


Figure 3.8: Block diagram of the VHF measurement campaign.

3.3.2 Configuration and parameters

We consider a CVOR of frequency 113 MHz. We set a power of -50 dBm for the direct signal and -70 dBm for the multipath. The signal from the RF input of R820T2 dongle is amplified with a gain of 20 dB, converted to baseband IQ data using a multiplier and a local oscillator at a sampling frequency of 1 MHz. The converted signal is filtered and decimated by a factor of 40. Our receiver model then processes these data at 25 kHz to estimate the azimuth information. The filtering parameters of our receiver model are the same as in Section 2.4.1 (see Table 2.1). In order to maximize the conventional VOR error, we set a relative multipath azimuth at 90° . We consider a relative multipath phase which randomly varies. In practice, this phase variation is performed manually as shown in Figure 3.9. In this test, we consider two recordings of 6 min.

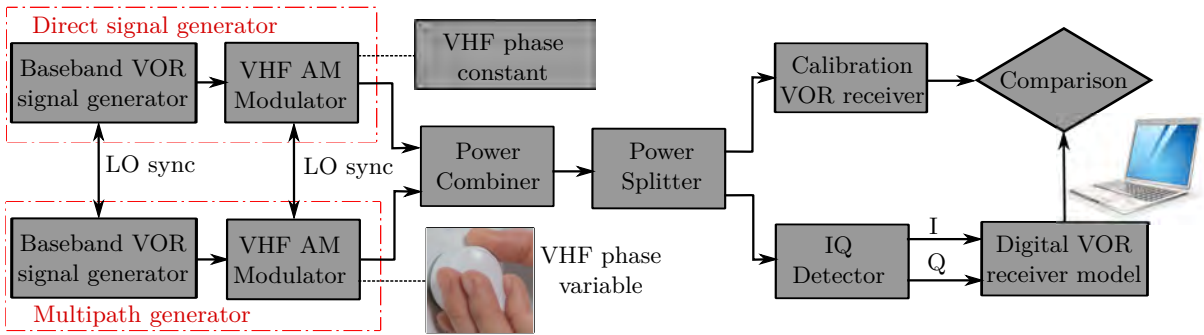


Figure 3.9: Random variation of the relative multipath phase.

3.3.3 Results

In Figures 3.10a and 3.10b, the bearing errors calculated by the digital IQ receiver model and the calibration receiver are plotted with respect to time for the two recordings. We can observe noise in the response of our digital IQ receiver model, generated during the data acquisition by the TNT-SDR dongle. Therefore, a smoothing filter of cutoff frequency 0.3 Hz is applied. We observe a very good agreement between our receiver model and the real receiver except during the first seconds, which corresponds to the transient period of the receiver model. The error measured by the EVS300 receiver is well evaluated by the receiver model in terms of envelope and oscillations.

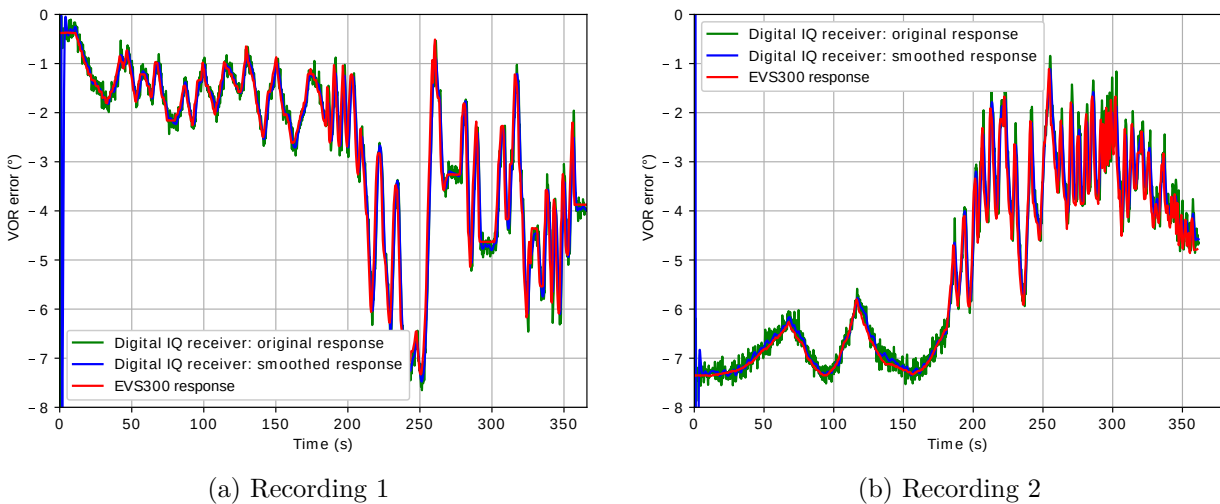


Figure 3.10: Receivers responses for the two recordings.

Now, we study the sensitivity of the results to the receiver model parameters. To this end, we modify the 3 dB bandwidths W_{30} and W_{DC} of the 30 Hz band-pass filter and the DC low-pass filter, respectively. The first parametric study is to assess the effect of parameter W_{30} on the receiver response. The second one consists in evaluating the response by varying the parameter W_{DC} . As shown in Table 3.2, we consider three different values for each parameter.

Parametric study 1		Parametric study 2	
W_{30} (Hz)	W_{DC} (Hz)	W_{30} (Hz)	W_{DC} (Hz)
2	1	10	1
6	1	10	2
10	1	10	3

Table 3.2: Characteristics of the parametric studies.

In Figures 3.11 and 3.12, we display the receiver responses for the first parametric study by varying the value of W_{30} and fixing the value of W_{DC} . During the first 2 seconds, the receiver responses change rapidly. This is due to the transient period of filters. The results of the three simulations are really similar with a delay that increases as the value of W_{30} increases. This is mainly due to the filtering group delay.

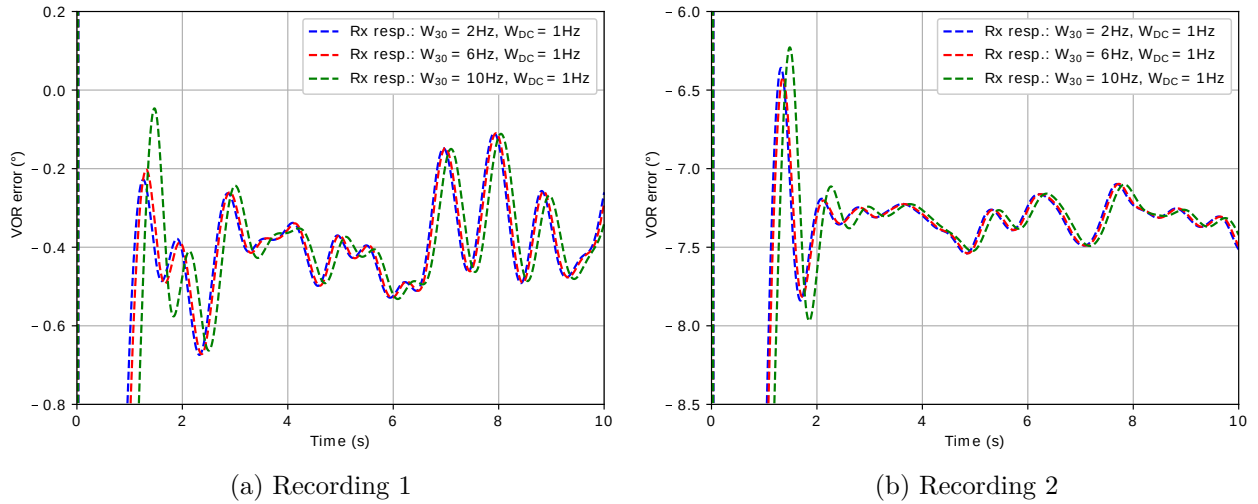


Figure 3.11: Results of the first parametric study from 0 s to 10 s.

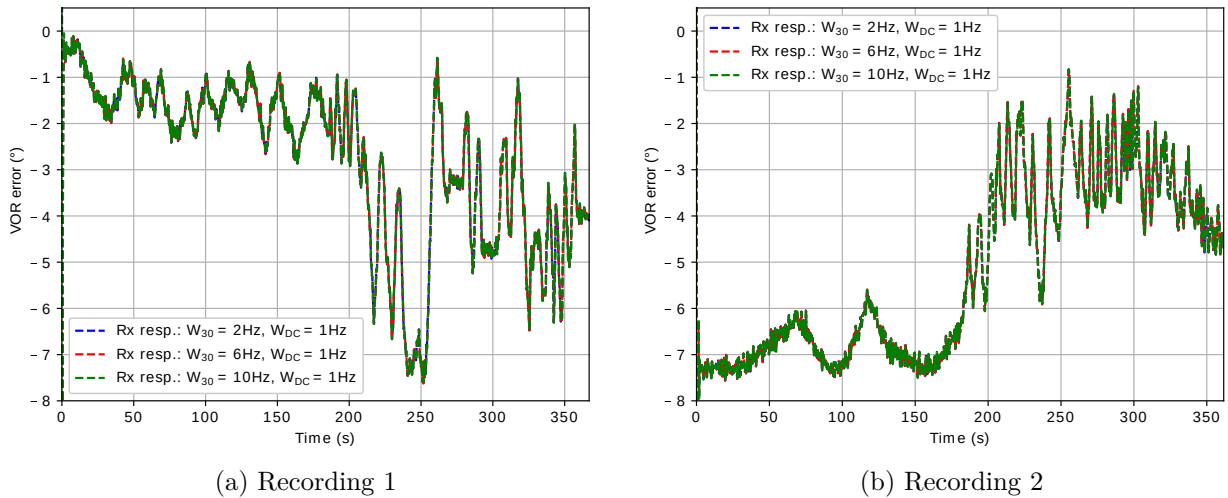


Figure 3.12: Results of the first parametric study from 0 s to 360 s.

In Figures 3.13 and 3.14, we display the receiver responses for the second parametric study where W_{DC} is varying while W_{30} is fixed. We can observe that if the 3 dB bandwidth of the DC low-pass filter increases, there are more fluctuations in the receiver response.

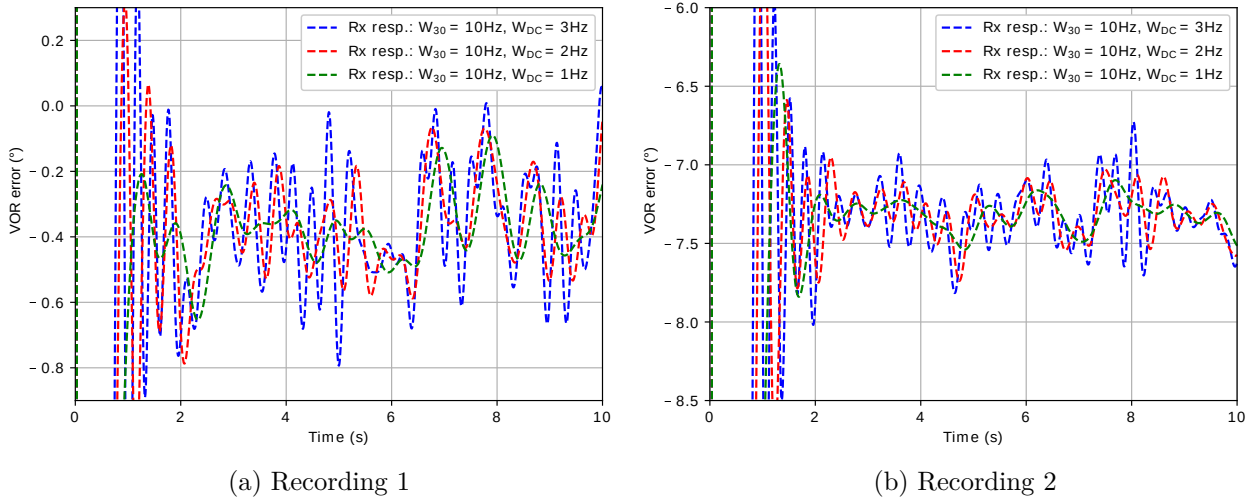


Figure 3.13: Results of the second parametric study from 0 s to 10 s.

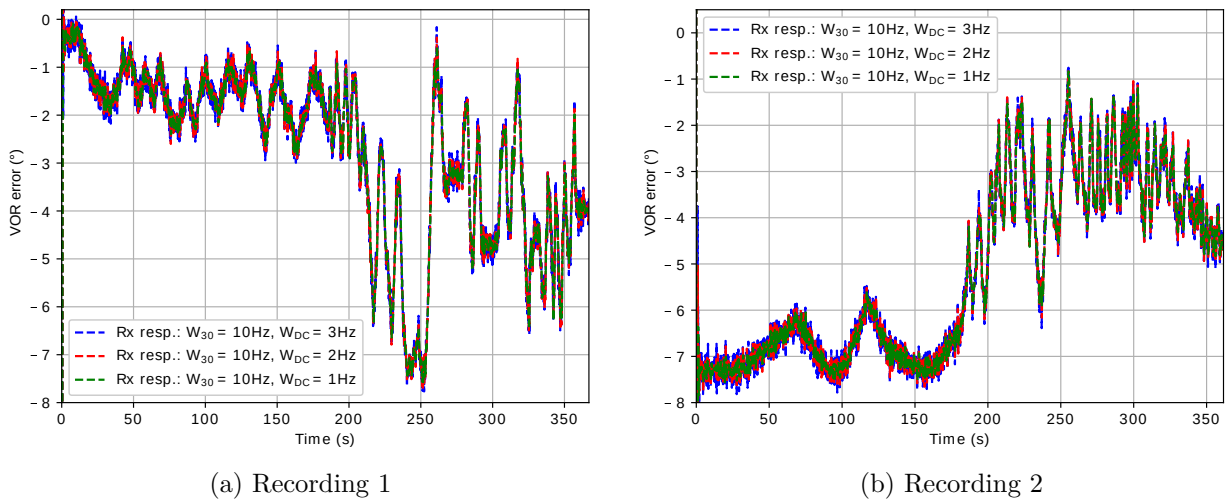


Figure 3.14: Results of the second parametric study from 0 s to 360 s.

From the results of the parametric study on the 3 dB bandwidths of the 30 Hz and DC filters, we have observed that the receiver response is mainly sensitive to the low-pass filter parameters of the phase comparator.

In the next section, we analyze the response of the digital receiver model for more complex scenarios.

3.4 Confrontation from baseband IQ measurements

The objective of this measurement consists in comparing the receiver model with the calibration receiver from a baseband IQ signal in a complex realistic scenario. In this section, we describe the measurement campaign. The confrontation results are then illustrated and analyzed.

3.4.1 Description

The block diagram of the baseband IQ measurement campaign is shown in Figure 3.15. The baseband IQ signal is generated in a complex scenario computed with our multipath time series simulator. The bearing error is computed by our digital VOR receiver model. We also perform an analytic calculation with Odunaiya expressions in order to emphasize the behavior of our receiver model in the context of time variation of multipath. To estimate the bearing error by the calibration receiver, the IQ data is sent to the EVS300 via its LF input by means of a digital-to-analog converter which is the audio output of a PC sound card.

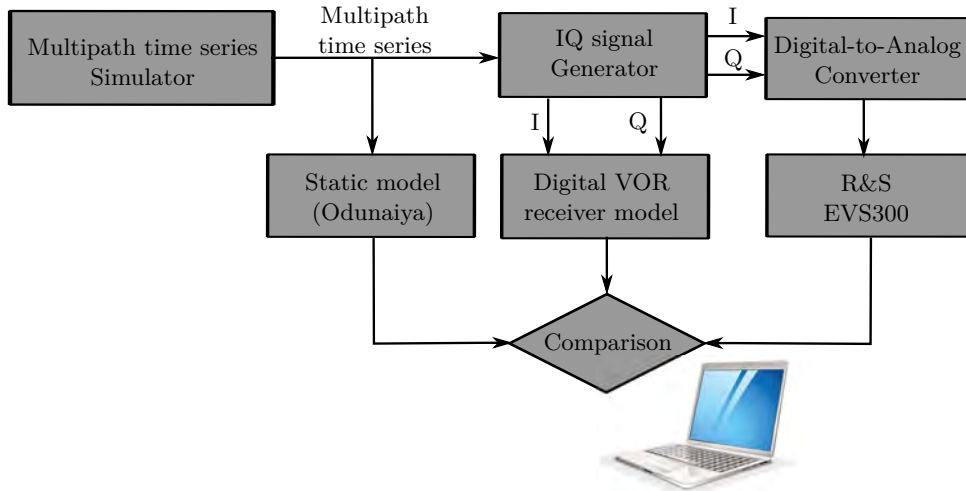


Figure 3.15: Block diagram of the baseband IQ measurement campaign.

In the next section, we propose the configuration to be simulated in order to generate the baseband IQ signal. The parameters of the measurement campaign are presented.

3.4.2 Configuration and parameters

As shown in Figure 3.16, we consider a CVOR station operating at a frequency of 113 MHz with a power of 50 W. At 1 km from the VOR station, there is a generic wind turbine. The aircraft moves along a straight trajectory of 15 km with a constant azimuth of 45° . The aircraft is motionless for the first 10 s to ensure the end of the transient state of the receiver. It starts at low velocity until the end of the trajectory where it reaches a speed of 180 km/h. The filtering parameters of our receiver model are the same as in Section 2.4.1 (see Table 2.1).

The time series of multipath parameters are computed by VERSO simulator and interpolated at a sampling frequency of 25 kHz in order to respect the Nyquist criterion and generate the I/Q data. Nevertheless, the sound card is unable to send this data to the EVS300. The current sound cards present a sampling frequencies of 44.1-192 kHz and a resolution of 16-32 bits. Therefore, we generate the I/Q data to be sent to the EVS300 at a sampling frequency of 48 kHz. We set the maximal sound card resolution, *i.e.* 32 bits, to minimize the quantization noise.

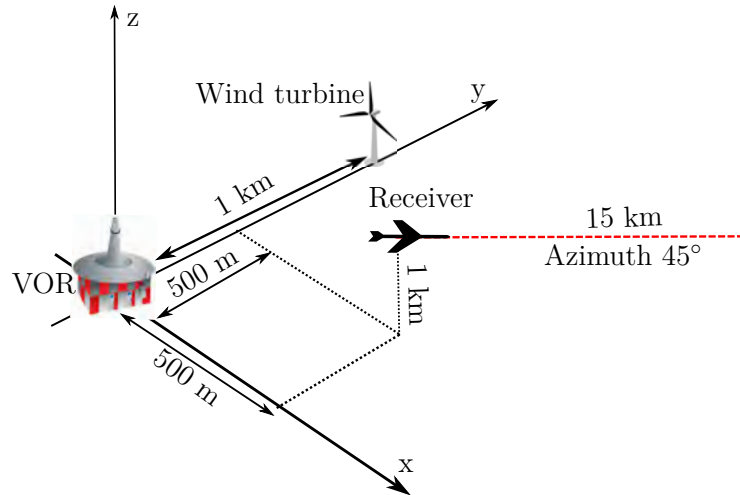


Figure 3.16: Proposed configuration for the baseband IQ comparisons.

3.4.3 Results

In Figure 3.17, the azimuth of the multipath is plotted with respect to time. The color indicates the power of the multipath relatively to the direct path.

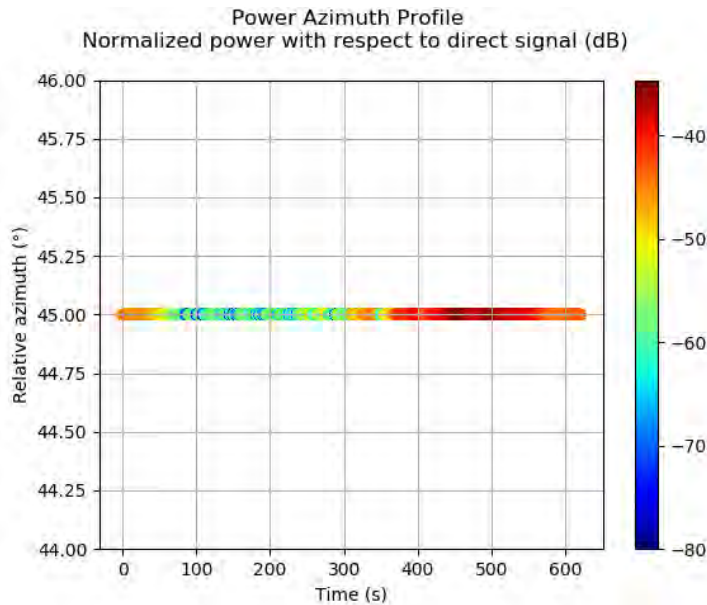


Figure 3.17: Relative Power Azimuth Profile (dB) of the multipath along the trajectory.

We observe that a single multipath exists. The multipath is powerful during the last part of the trajectory from 300 s to 600 s. This is when the aircraft is in the specular reflection zone of the wind turbine.

We show in Figure 3.18 the bearing errors computed by the Odunaiya expression, the receiver model, and the calibration receiver along the aircraft trajectory. The calibration receiver and receiver model responses change rapidly during the first 2 seconds. This is due to the filtering transient period. The receiver responses are equal to the Odunaiya expression during 8 s when no dynamic effects are involved. Consistently with the relative power azimuth profile plotted in Figure 3.17, the three responses are only significant during the last part of the aircraft trajectory.

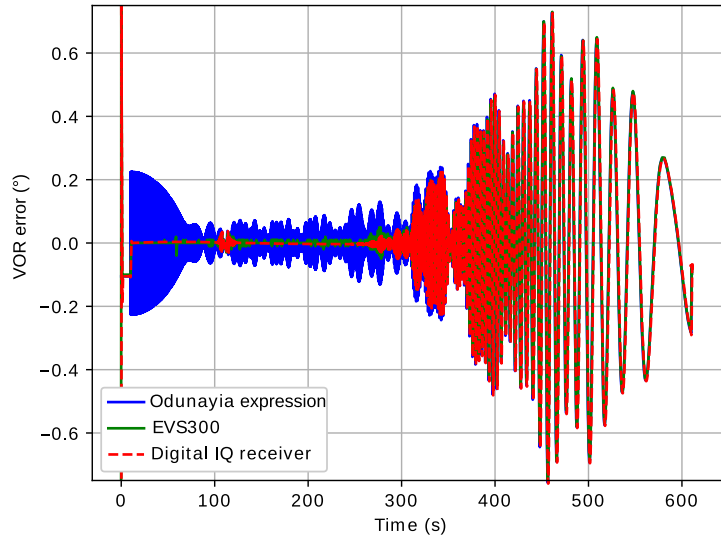


Figure 3.18: Receiver responses along the trajectory for the baseband IQ measurements.

In Figures 3.19a, 3.19b, the bearing errors are plotted using 2 time scales. When the aircraft accelerates in the vicinity of the VOR station and the wind turbine, the phase difference between the direct signal and the multipath changes in a fast way. This explains the fast fluctuations of the VOR error estimated by the Odunaiya expression between 10 s and 320 s as illustrated in Figures 3.18 and 3.19a. Therefore, the static response follows neither the calibration receiver nor the receiver model. This is explained in Section 4.3. When the aircraft moves away from the VOR and the wind turbine, the receiver responses correspond again to the Odunaiya expression despite the high speed of the aircraft as shown in Figure 3.19b. This is due to the slow variation of multipath. During this phase, there is a slight delay between the three responses that is due to the receiver group delays.

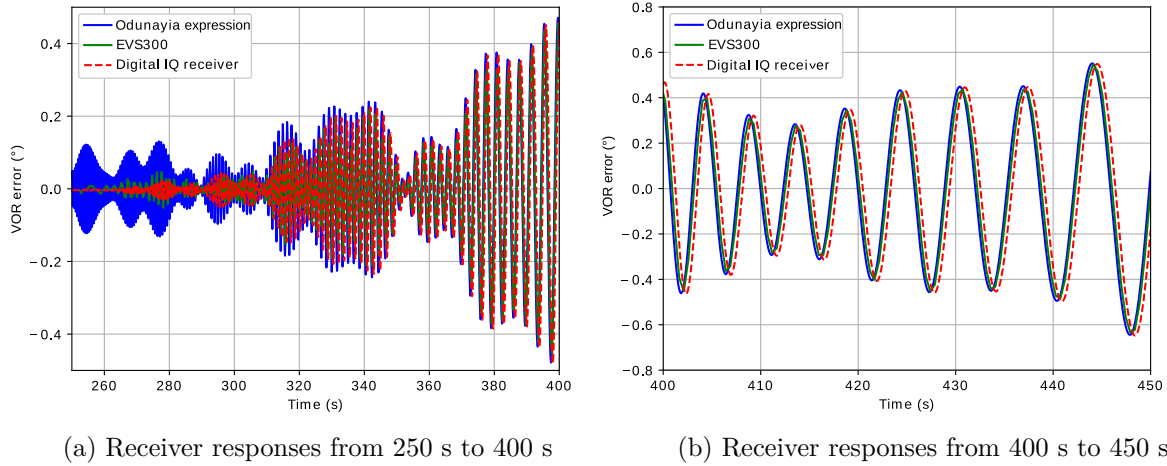


Figure 3.19: Receiver responses for 2 time scales.

3.5 Conclusion

In this chapter, the difficulty of analysing the simulation results in comparison with available in-flight measurements has been presented. Thus, a solution which consists in performing two laboratory measurements in a conducted environment for CVOR signals has been proposed. The first one has been performed in the VHF frequency band for one canonical multipath. A parametric study has been carried out in this measurement in order to assess the sensitivity of the results to the receiver model parameters. The second one has been performed using baseband IQ signals in a complex scenario. The measurements results have shown a good agreement between receivers. Thus, we can be confident on the structure and the parameters of our digital IQ receiver model based on this confrontation with the EVS300 calibration receiver. We have also observed here that the Odunaiya expression does not always give the consistent response compared to the receivers. This phenomenon and the receiver group delay are discussed in the next chapter.

Chapter 4

Analysis of the Bearing Error Obtained from the Receiver Model

4.1 Introduction

The Odunaiya formula does not always give the consistent response compared to the digital IQ receiver model and to the calibration receiver for conventional VOR signals as shown in Figure 3.18. A delay between the receiver response and the Odunaiya expression has been constantly detected as shown in Figure 2.10. In this chapter, we present a CVOR analysis in order to clarify these observations. A DVOR analysis is also given. We evaluate the sensitivity of our receiver model to the type of FM demodulator and the sensitivity of the reference signal to multipath.

In Section 4.2, the receiver group delay is presented. We present in Section 4.3 a method to determine the validity domain of the static Odunaiya expression for computing the CVOR multipath error. We demonstrate in Section 4.4 that the DVOR error is sensitive to the type of FM demodulator used in the receiver model. In Section 4.5, we evaluate the effect of multipath on the reference signal for DVOR.

4.2 Receiver group delay

The illustration test given in Section 2.4 has shown that there is a delay between the digital IQ receiver model and the Odunaiya response as shown in Figure 2.10. We show here that this is due to the receiver group delay, which mainly corresponds to the filtering response.

The group delay τ_g is defined as the derivative of the phase of the filter transfer function $\theta(\omega)$ with respect to the angular frequency ω . This is expressed as

$$\tau_g = -\frac{d\theta(\omega)}{d\omega}. \quad (4.1)$$

A linear phase gives a constant group delay. A constant group delay implies that all spectral components of a signal are transmitted with the same time shift. Contrary to the FIR filters, the IIR filters are generally characterized by a non-linear phase response [48]. As the 30 Hz band-pass filter and the DC low-pass filter applied in our receiver model are IIR filters, their group delays are not constant.

We consider an example to illustrate the group delay of these IIR filters for different orders. The 3 dB bandwidths W_{30} and W_{DC} of the 30 Hz band-pass filter and the DC low-pass filter are set to 2 Hz and 1 Hz, respectively. Four order values (5, 7, 9 and 11) are considered for each filter. The group delay calculated with (4.1) is shown in Figure 4.1. As expected, the group delay is not constant in the pass-band of these filters. We also observe that this delay increases as the filter order increases.

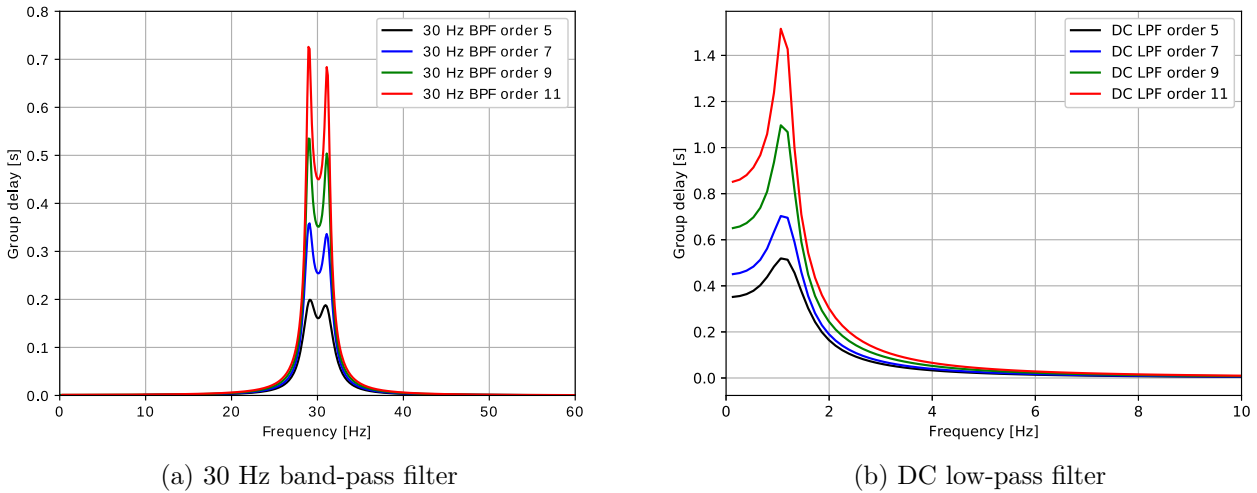


Figure 4.1: Group delay of filters.

In our receiver model, the 9960 Hz high-pass filter is a FIR. Its group delay is then constant and its value can be expressed as

$$\tau_g^{\text{HPF}} = \frac{M - 1}{2F_s}, \quad (4.2)$$

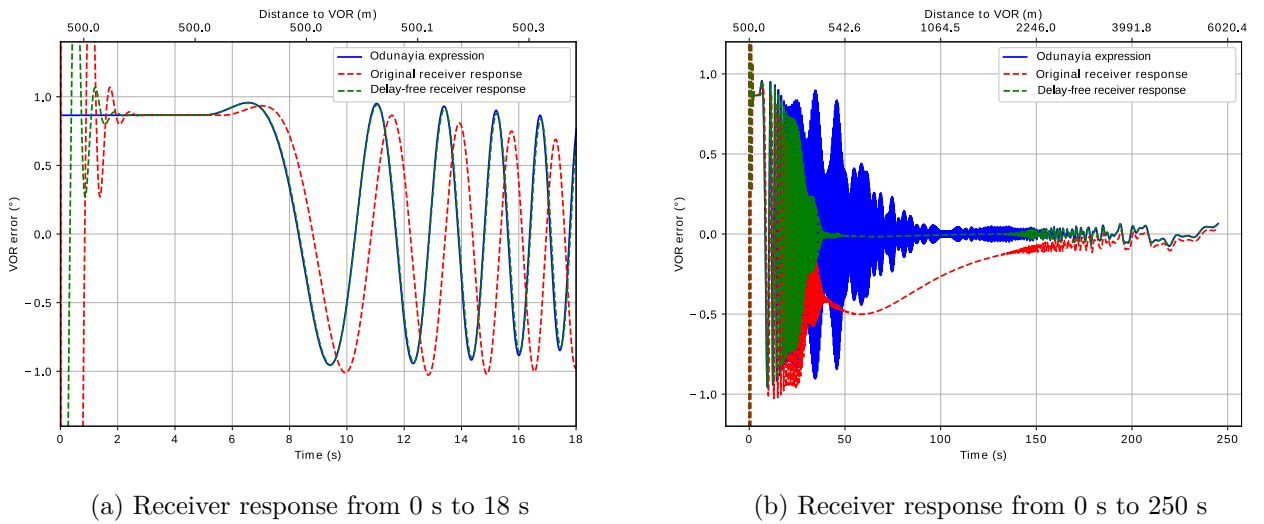
where M is the filter order and F_s is the sampling frequency. Based on the order value of the 9960 Hz high-pass filter given in Table 2.1 and the F_s value of 25 kHz, τ_g^{HPF} is equal to 0.28 ms. Therefore, the value of this delay is neglectable compared to the 30 Hz and DC filters delays. Thus, the total group delay of the receiver is given by the sum of the delays τ_g^{BPF} and τ_g^{LPF} corresponding to the 30 Hz band-pass filter and the DC low-pass filter, respectively, such that

$$\tau_g^{\text{tot}} = \tau_g^{\text{BPF}} + \tau_g^{\text{LPF}}. \quad (4.3)$$

In post-processing, we can remove the effect of this delay in the receiver response. We

consider the example of the test results given in Section 2.4.2 (see Figure 2.10). Based on the filtering parameters given in Table 2.1 and the value of the sampling frequency of 25 kHz, the receiver group delay is approximately equal to 0.52 s.

We illustrate in Figures 4.2a and 4.2b the results of the delay-free receiver response using 2 time scales. When the effect of the group delay is removed, the receiver response better fits with the expression of Odunaiya in Figure 4.2a. In Figure 4.2b, the relative multipath phase changes in a fast way as the aircraft accelerates in the vicinity of the VOR station and wind turbine between 30 s and 140 s. When the aircraft speed is slow or when the aircraft is far from the VOR station, the results fit with the Odunaiya expression. This is the case when $t < 30$ s and $t > 140$ s, approximately. When the aircraft speed is faster, for $30 \text{ s} < t < 140 \text{ s}$, the results do not fit with the Odunaiya formulation and the error tends towards zero.



(a) Receiver response from 0 s to 18 s

(b) Receiver response from 0 s to 250 s

Figure 4.2: Delay-free receiver response.

From now on, in all the simulations, delay-free responses are considered.

4.3 Validity domain of the CVOR Odunaiya expression

In the Odunaiya expression, everything is expected static. However, multipath change in time as the aircraft moves. This may explain why the delay-free receiver response is not always consistent with the Odunaiya expression. Therefore, we propose to determine the validity domain of the static Odunaiya expression for computing the CVOR multipath error. To do this, a comparison test between our receiver model and the Odunaiya expression is shown and interpreted in Section 4.3.1. In Section 4.3.2, a spectral analysis is

performed to explain the results. Finally, a geometric criterion is deduced and illustrated in Section 4.3.3 in order to define the validity domain of the Odunaiya CVOR expression.

4.3.1 Comparisons between the Odunaiya expression and the receiver model

We present in this section a confrontation test between the digital receiver model and the Odunaiya formula when multipath changes in time.

As shown in Figure 4.3, we consider a CVOR station operating at a frequency of 113 MHz with a power of 50 W. A generic wind turbine is located at 1 km from the VOR station. The aircraft moves along a circular trajectory around the VOR with a radius of 4.5 km and an altitude of 1 km. The aircraft is motionless for the first 10 s to ensure the end of the transient state of the receiver. Then, it starts at low velocity until the end of the trajectory where it reaches a speed of 324 km/h. The time series of multipath parameters are interpolated at a frequency of 25 kHz in the I/Q signal generator. The 3 dB bandwidths of the 30 Hz band-pass filter W_{30} and the DC low-pass filter W_{DC} are set to 2 Hz and 1 Hz, respectively.

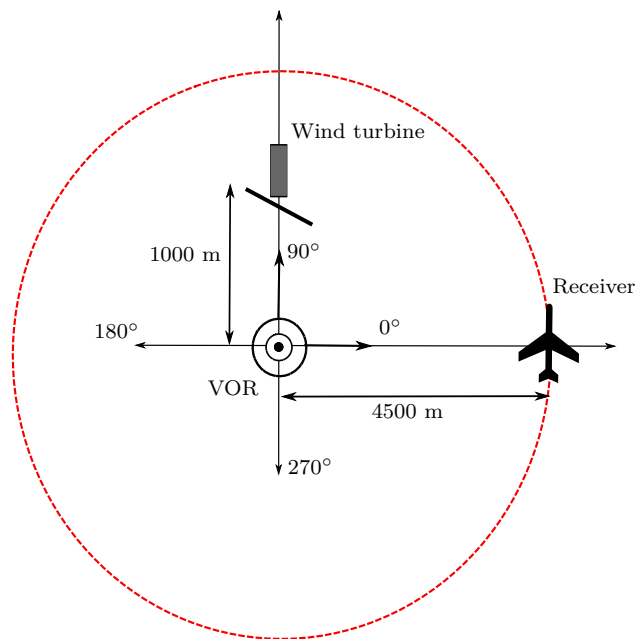


Figure 4.3: Top view of a circular aircraft trajectory around a CVOR.

In Figure 4.4a, we display the instantaneous frequency of the multipath relatively to the direct path with respect to time. This is calculated from finite differences applied to the phase variation with time. As expected, the relative Doppler frequency of the multipath depends on the speed of the aircraft and its position with respect to the VOR station and the wind turbine.

In Figure 4.4b, the VOR errors obtained with the Odunaiya expression and with the

VOR receiver model are plotted with respect to time. The receiver response fits with the Odunaiya expression during the first 90 s when the aircraft moves slowly. As the relative Doppler frequency of the multipath increases, we can observe significant discrepancies between the static Odunaiya expression and the dynamic VOR receiver model. Whenever the relative Doppler frequency of the multipath is lower in absolute value than about 1 Hz, both models behave similarly.

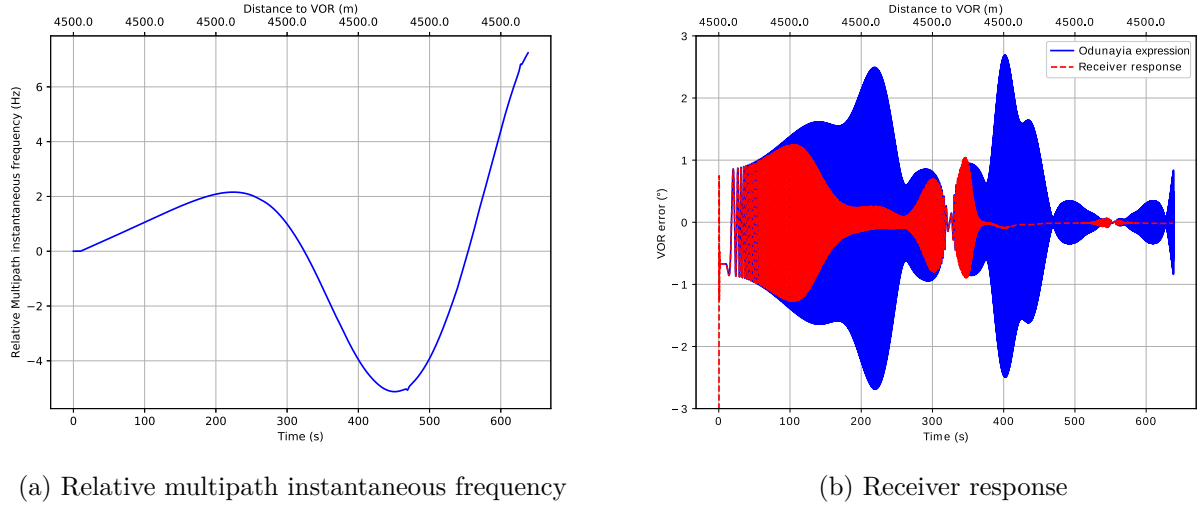


Figure 4.4: Simulation results of the confrontation test between the digital receiver model and the Odunaiya expression in dynamic context.

4.3.2 Spectral analysis of the received intermediate signals

We test here the influence of the bandwidth of the receiver filters on the bearing error. Then, we propose to perform a spectral analysis on the received intermediate signals by processing a canonical CVOR multipath.

The canonical CVOR multipath is characterized by a relative power of -20 dB, and a relative azimuth of 90° . In each case, the phase is linear, *i.e.* calculated from a set Doppler shift f_{Dop} .

- **Case 1 : Doppler shift included in both filter bandwidths**

In this first case, the Doppler shift of the multipath is assumed to be included in the 3 dB bandwidth of both filters. Thus, we consider the following parameters : $f_{\text{Dop}} = 1$ Hz , $W_{30} = 6$ Hz and $W_{\text{DC}} = 3$ Hz.

As shown in Figures 4.5a and 4.5b, both filters allow the multipath, which frequency is shifted of 1 Hz with respect to the direct path, to pass through. Thus, the Odunaiya expression is consistent with the receiver output as shown in Figure 4.6.

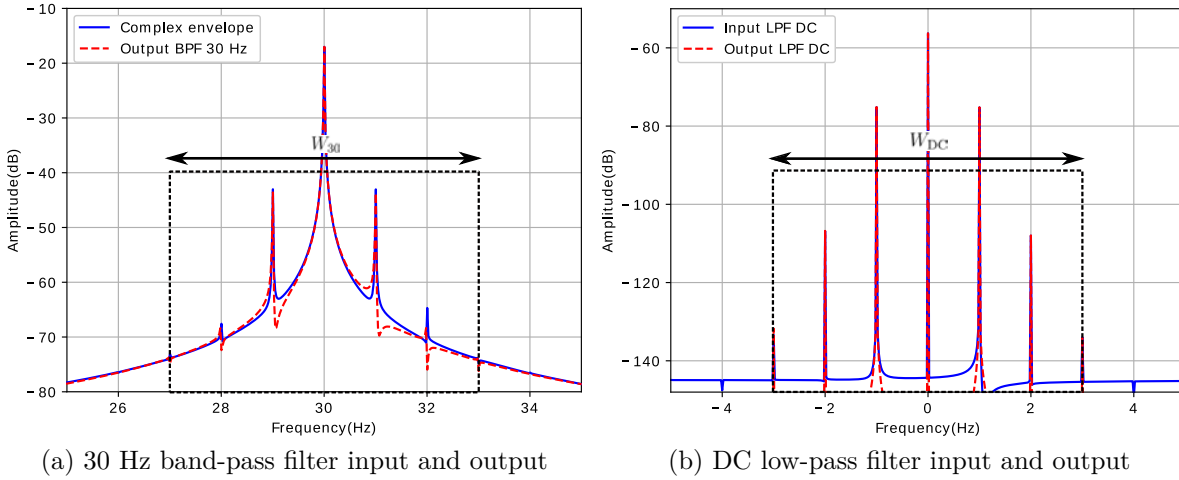


Figure 4.5: Input and output of the receiver filters in case 1.

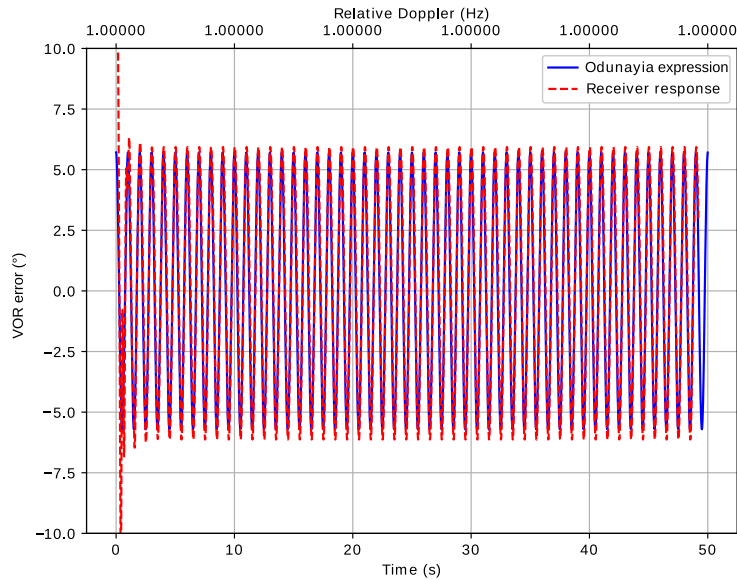


Figure 4.6: Receiver response in case 1.

- **Case 2 : Doppler shift not included in one of both filter bandwidths**

In this second case, we consider that the Doppler shift of the multipath is not included in one of both filter bandwidths. First, it is included only in the DC low-pass filter. To do this, we set : $f_{\text{Dop}} = 6 \text{ Hz}$, $W_{30} = 6 \text{ Hz}$ and $W_{\text{DC}} = 7 \text{ Hz}$. This case is denoted as 2-a.

As shown in Figure 4.7a, the frequency component $(30 \pm f_{\text{Dop}})$ is removed by the 30 Hz band-pass filter. For this reason, we cannot see this component at the DC low-pass filter input as shown in Figure 4.7b. Thus, we observe in Figure 4.8 that the receiver response does not fit with the Odunayia expression. Besides, since the multipath is filtered in this case, the error becomes nearly zero.

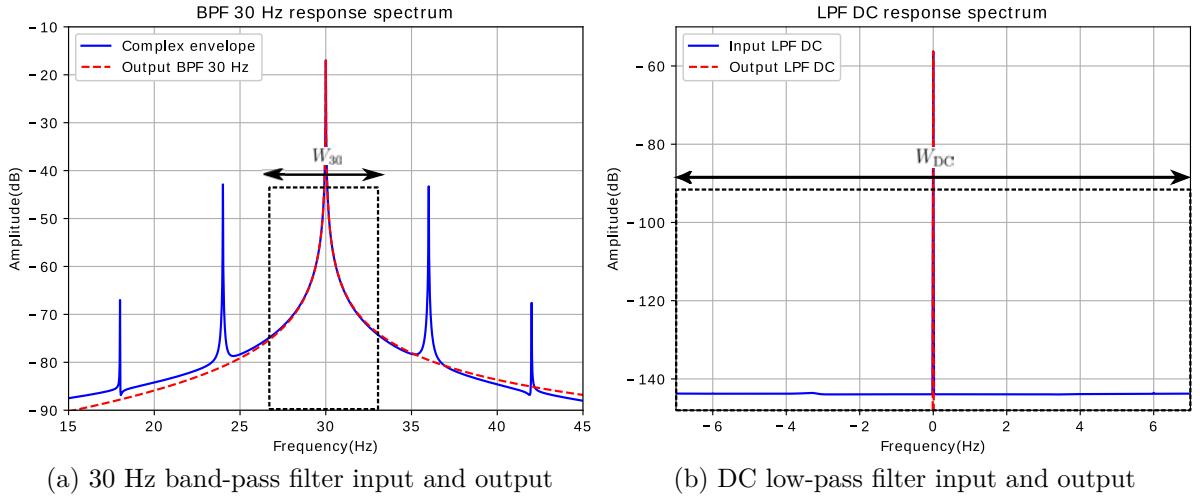


Figure 4.7: Input and output of the receiver filters in case 2-a.

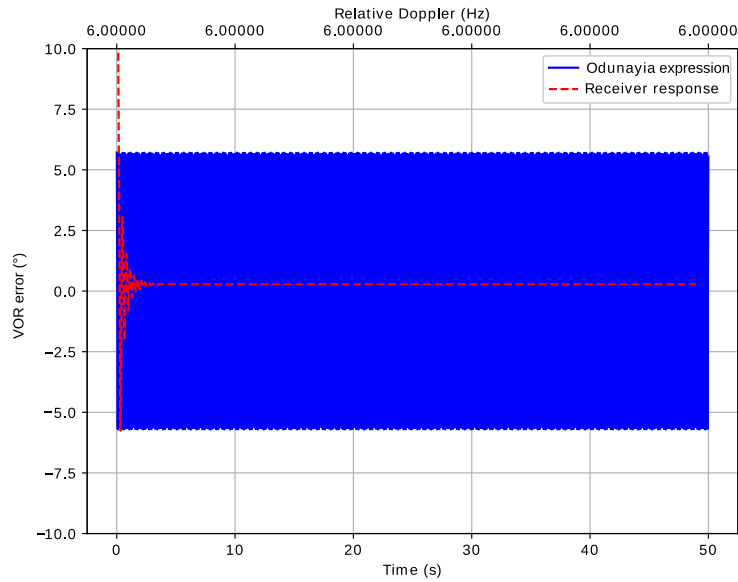


Figure 4.8: Receiver response in case 2-a.

Secondly, we consider that the Doppler shift is included only in the 30 Hz band-pass filter (case 2-b). Thus, we set the following parameters : $f_{Dop} = 3$ Hz , $W_{30} = 6$ Hz and $W_{DC} = 1$ Hz.

The 30 Hz band-pass filter allows the frequency component ($30 \pm f_{Dop}$) to pass through as shown in Figure 4.9a. Nevertheless, this component is filtered in the phase comparator as illustrated in Figure 4.9b. That explains why in this case the receiver bearing error is zero as shown in Figure 4.10.

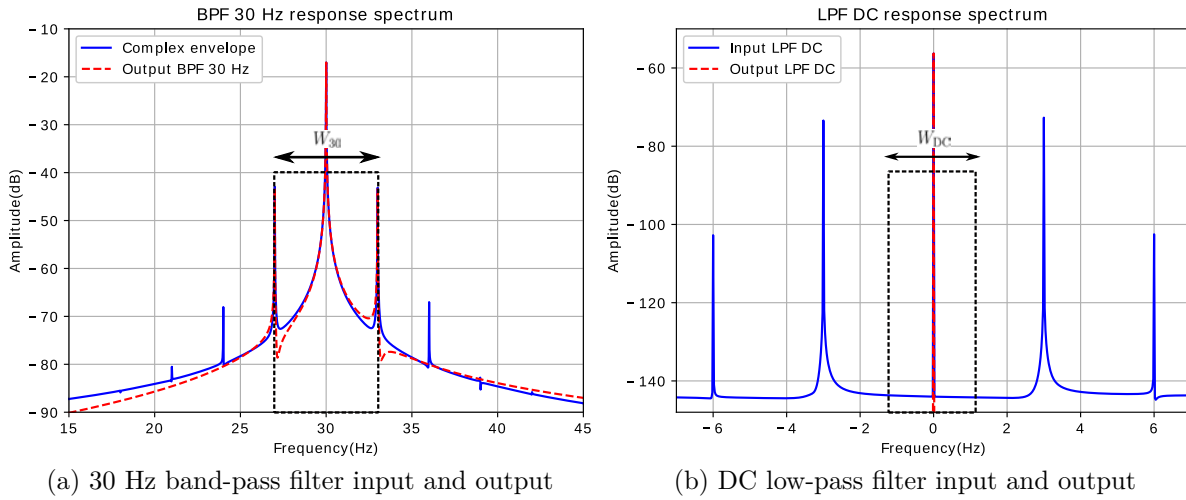


Figure 4.9: Input and output of the receiver filters in case 2-b.

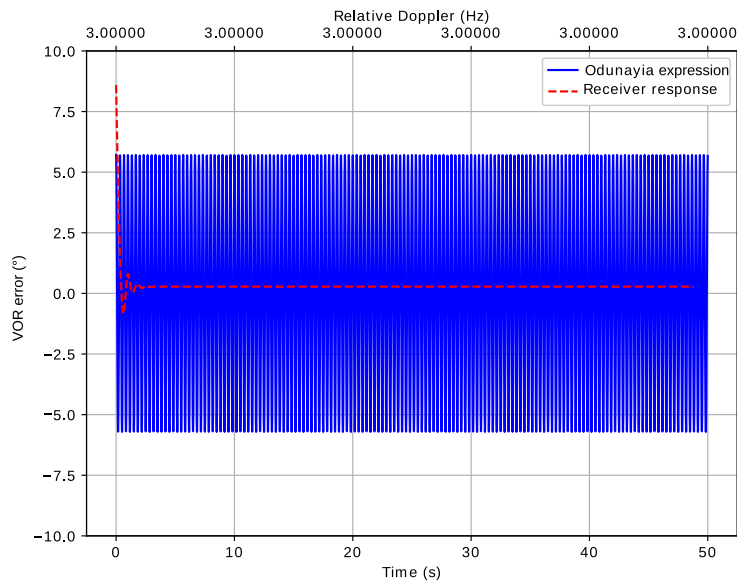


Figure 4.10: Receiver response in case 2-b.

Based on this spectral analysis for a canonical multipath, we conclude that the receiver response sensitivity to multipath depends on the relative instantaneous frequency of the multipath and the bandwidth parameters of the receiver filters.

4.3.3 Geometric criterion

We have observed in the previous section that the validity domain of the Odunayia formula is expressed in terms of the Doppler shift of the multipath with respect to the direct path. This leads to a geometric criterion that defines this domain. This criterion is presented and illustrated in this section.

4.3.3.a Definition

We consider a general configuration plotted in Figure 4.11. The aircraft moves in the direction $\hat{\mathbf{u}}_m$. The aircraft's motion relative to the VOR station yields a Doppler shift given by

$$\delta f_D^0 = -f_0 \frac{v_{Rx}}{c_0} \hat{\mathbf{r}} \cdot \hat{\mathbf{u}}_m, \quad (4.4)$$

where f_0 is the source frequency, v_{Rx} is the receiver speed, c_0 is the speed of light and $\hat{\mathbf{r}}$ is the VOR-aircraft direction. Similarly, the Doppler shift of the multipath is given by

$$\delta f_D^1 = -f_0 \frac{v_{Rx}}{c_0} \hat{\mathbf{r}}_{w_1} \cdot \hat{\mathbf{u}}_m, \quad (4.5)$$

where $\hat{\mathbf{r}}_{w_1}$ is the wind turbine-aircraft direction.

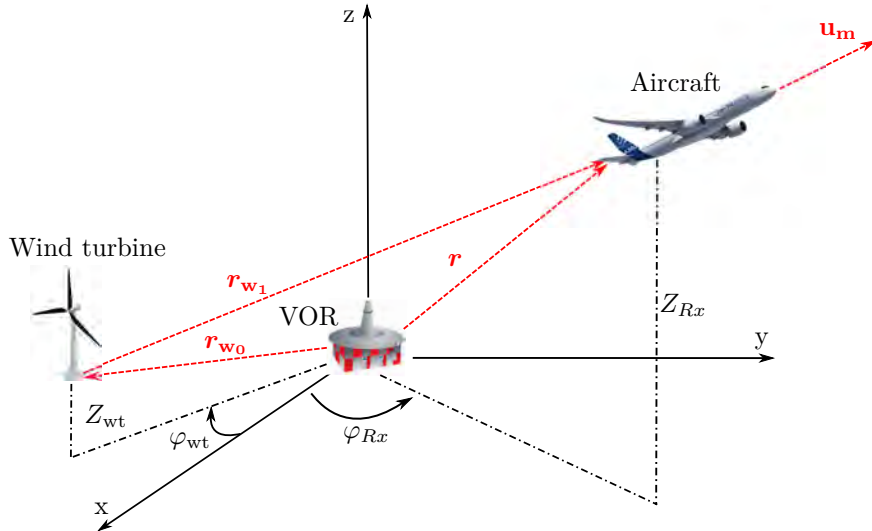


Figure 4.11: Aircraft trajectory configuration.

If the instantaneous frequency is not included in one of the two filter bandwidths, there is no multipath error. Thus, the Odunaiya expression is considered invalid when

$$|\delta f_D^1 - \delta f_D^0| = f_0 \frac{v_{Rx}}{c_0} |\hat{\mathbf{r}}_{w_0} \cdot \hat{\mathbf{u}}_m| > \min \left(\frac{W_{30}}{2}, W_{DC} \right), \quad (4.6)$$

where $\hat{\mathbf{r}}_{w_0}$ is the VOR-wind turbine direction. From (4.6), the results are independent of the altitude for aircraft trajectories in a horizontal plane (constant altitude) or for a wind turbine at the same altitude as the VOR station. This criterion is illustrated for different types of aircraft trajectory in the next section.

4.3.3.b Examples

We consider a VOR station operating at a frequency of 113 MHz. An obstacle is placed on azimuth 0° at 5 km from the VOR station. $\min\left(\frac{W_{30}}{2}, W_{DC}\right)$ is set at 10 Hz. We consider a speed of 180 km/h. The aircraft trajectories are in a horizontal plane, so that results are independent of the altitude.

In the first case, we consider radial trajectories with distances up to 50 km from the VOR station. In Figure 4.12a, we observe that the Odunaiya expression is invalid in the vicinity of the wind turbine. We consider in the second case circular trajectories around the VOR station. We observe in Figure 4.12b that the validity area of the Odunaiya expression is smaller than for radial trajectories. Actually, the phase difference between the direct and the multipath changes in a fast way when the aircraft moves around the VOR and the wind turbine.

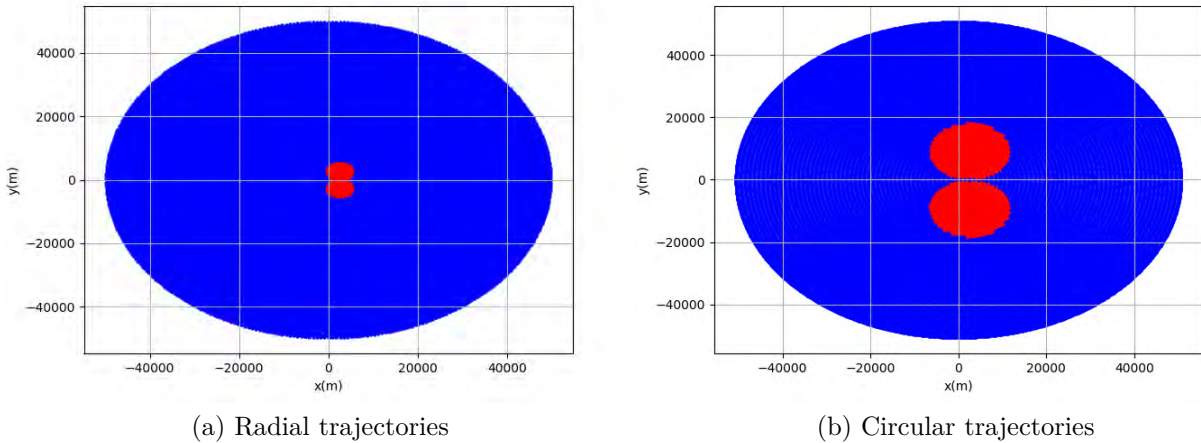


Figure 4.12: Validity domain of the CVOR Odunaiya expression (in blue).

4.3.4 Conclusion

We have observed that the CVOR Odunaiya expression is no more valid when the multipath is rejected outside the bandwidth of the receiver filters because of the Doppler effect. Then, the multipath does not affect anymore the bearing estimation. However, the Odunaiya expression is conservative: it provides a worst-case result for which multipath are not attenuated by the receiver filters.

4.4 Analytic DVOR multipath error

In order to demonstrate the Doppler error expression given by (1.28), Odunaiya accounts for an ideal FM demodulator. In our receiver model, we apply a quadrature FM demodulator. We here demonstrate that this modifies the receiver behavior. For this reason,

we develop and validate an alternative expression to the analytic DVOR multipath error which is consistent with our quadrature FM demodulator. This expression is called I2Q-FM error.

4.4.1 Confrontation test

We here perform a confrontation test between the receiver model and the Odunaiya expression by processing a canonical multipath for a DVOR. Even with a simple canonical multipath, we show that the receiver response does not fit with the Odunaiya expression.

We consider a weak multipath characterized by a relative amplitude a_1/a_0 of -40 dB and a relative azimuth $(\varphi_1 - \varphi_0)$ which varies between -180° and 180° in order to model an aircraft rotation around the VOR station. To maximize the Odunaiya expression, we set a relative multipath phase $(\theta_1 - \theta_0)$ to 0° . In Figure 4.13, the DVOR errors computed by the Odunaiya expression and the receiver model are plotted with respect to time. We observe that both models do not give the same response despite the canonical multipath. This is theoretically explained in the next section.

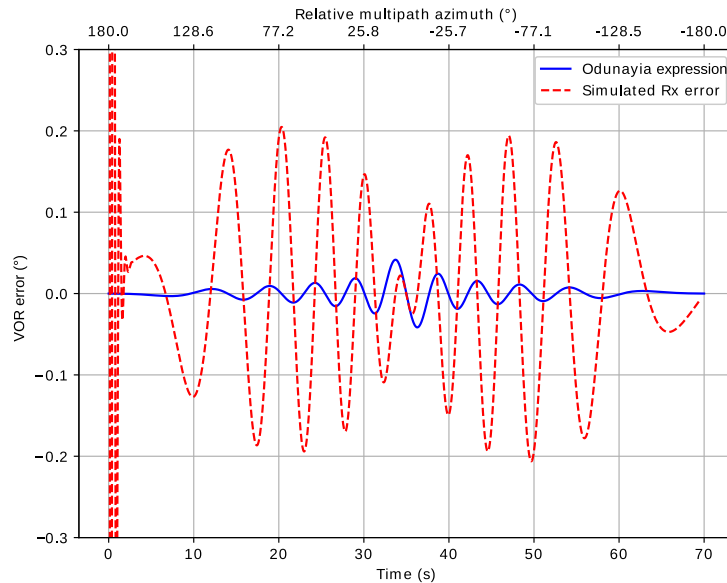


Figure 4.13: DVOR error computed by Odunaiya expression and receiver model.

4.4.2 Demonstration

In this section, we develop the expression of the I2Q-FM error, *i.e.* the error associated with a quadrature FM demodulator. The principle of our FM demodulator is based on FM to AM conversion via a multiplication with a signal replica in quadrature delay as shown in Section 2.3.3.c. The input FM signal is converted to an AM signal. An AM demodulation is then used to extract the information. This makes the FM demodulator

more sensitive to multipath compared to the ideal FM demodulation used to demonstrate the Odunaiya expression for DVOR signals.

We consider the presence of a single multipath with moderate amplitude. The high-pass filter of the FM variable signal is assumed to be ideal. In order to introduce the delay replica of the VAR signal, the quadrature delay τ_q must be taken small compared to the period of the 30 Hz signal and the quadrature phase shift error ε is considered zero, so that

$$\begin{aligned}\varepsilon &\simeq 0 \\ 2\pi f_{LF}\tau_q &\simeq 0.\end{aligned}\tag{4.7}$$

In order to simplify the calculations, we set $a_0 = 1$, $\theta_0 = 0$, $\varphi_0 = 0$. Based on (1.6), the VAR signal at the FM demodulator input is defined by

$$x_{\text{var}}(t) = \cos(2\pi f_{sc}t + \phi_{sc}^0(t)) + A_1 \cos(2\pi f_{sc}t + \phi_{sc}^1(t)),\tag{4.8}$$

with

- $A_1 = a_1 \cos(\theta_1)$
- $\phi_{sc}^0(t) = m_f \sin(2\pi f_{LF}t)$
- $\phi_{sc}^1(t) = m_f \sin(2\pi f_{LF}t - \varphi_1)$

The received signal corresponds to the sum of 2 FM signals centered at the same frequency. Thus, this signal can be expressed as

$$x_{\text{var}}(t) = R(t) \cos(2\pi f_{sc}t + \phi_{LF}(t)),\tag{4.9}$$

where $R(t)$ is the envelope of the received signal, which is defined by

$$R(t) = \sqrt{1 + A_1^2 + 2A_1 \cos(\phi_{sc}^1(t) - \phi_{sc}^0(t))},\tag{4.10}$$

and $\phi_{LF}(t)$ is the LF modulated phase, which is given by

$$\phi_{LF}(t) = \phi_{sc}^0(t) + \tan^{-1} \left(\frac{A_1 \sin(\phi_{sc}^1(t) - \phi_{sc}^0(t))}{1 + A_1 \cos(\phi_{sc}^1(t) - \phi_{sc}^0(t))} \right).\tag{4.11}$$

For an error smaller to 3° , we can linearize the arctangent by replacing its expression with its first-order Taylor series in A_1 , so that

$$\phi_{LF}(t) \simeq \phi_{sc}^0(t) + A_1 \sin(\phi_{sc}^1(t) - \phi_{sc}^0(t)).\tag{4.12}$$

Applying an approach similar to the one developed in absence of multipath (equations from (2.20) to (2.24)), we end up with

$$p(t) = x_{\text{var}}(t) x_{\text{var}}(t - \tau_q) = \frac{-R(t)R(t - \tau_q)}{2} \left[\varepsilon + \tau_q \dot{\phi}_{LF} \left(t - \frac{\tau_q}{2} \right) \right]. \quad (4.13)$$

Upon assuming (4.7), this amounts to

$$p(t) = -\frac{\tau_q}{2} R^2(t) \dot{\phi}_{LF}(t) = -\frac{\tau_q}{2} (1 + A_1^2 + 2A_1 \cos(\phi_{sc}^1(t) - \phi_{sc}^0(t))) \dot{\phi}_{LF}(t). \quad (4.14)$$

The derivative of the signal $\phi_{LF}(t)$ is expressed as

$$\dot{\phi}_{LF}(t) = \dot{\phi}_{sc}^0(t) + A_1(\dot{\phi}_{sc}^1(t) - \dot{\phi}_{sc}^0(t)) \cos(\phi_{sc}^1(t) - \phi_{sc}^0(t)). \quad (4.15)$$

Substituting (4.15) in (4.14) and using a Taylor series of order 1 in A_1 , we obtain

$$p(t) \simeq -\frac{\tau_q}{2} \left[\dot{\phi}_{sc}^0(t) + A_1(\dot{\phi}_{sc}^1(t) + \dot{\phi}_{sc}^0(t)) \cos(\phi_{sc}^1(t) - \phi_{sc}^0(t)) \right]. \quad (4.16)$$

We then need to expand the terms $\phi_{sc}^0(t)$ and $\phi_{sc}^1(t)$ in this expression. To do so, we write

$$\begin{aligned} \phi_{sc}^1(t) - \phi_{sc}^0(t) &= m_f \sin(2\pi f_{LF} t - \varphi_1) - m_f \sin(2\pi f_{LF} t) \\ &= -2m_f \cos\left(\frac{4\pi f_{LF} t - \varphi_1}{2}\right) \sin\left(\frac{\varphi_1}{2}\right). \end{aligned} \quad (4.17)$$

As in [49], the Fourier series expansion of $\cos(\phi_{sc}^1(t) - \phi_{sc}^0(t))$ then yields

$$\cos(\phi_{sc}^1(t) - \phi_{sc}^0(t)) = J_0(z) + 2 \sum_{n=1}^{\infty} (-1)^n J_{2n}(z) \cos(4\pi n f_{LF} t - n\varphi_1), \quad (4.18)$$

with $z = -2m_f \sin\left(\frac{\varphi_1}{2}\right)$.

As the high frequencies are filtered, only the terms associated with $J_0(z)$ and $J_2(z)$ are kept, so that

$$\cos(\phi_{sc}^1(t) - \phi_{sc}^0(t)) = J_0(z) - 2J_2(z) \cos(4\pi f_{LF} t - \varphi_1). \quad (4.19)$$

The derivative of the signal $\phi_{sc}^1(t)$ is expressed as

$$\dot{\phi}_{sc}^1(t) = 2\pi m_f f_{LF} \cos(2\pi f_{LF} t - \varphi_1). \quad (4.20)$$

Multiplying (4.18) and (4.20) and keeping only the terms at the f_{LF} frequency, we end up with

$$\begin{aligned} \dot{\phi}_{sc}^1(t) \cos(\phi_{sc}^1(t) - \phi_{sc}^0(t)) &= 2\pi m_f f_{LF} \left[J_0(z) \cos(2\pi f_{LF} t - \varphi_1) \right. \\ &\quad \left. - J_2(z) \cos(2\pi f_{LF} t) \right]. \end{aligned} \quad (4.21)$$

Likewise, the term $\dot{\phi}_{sc}^0(t) \cos(\phi_{sc}^1(t) - \phi_{sc}^0(t))$ in (4.16) is given by

$$\dot{\phi}_{sc}^0(t) \cos(\phi_{sc}^1(t) - \phi_{sc}^0(t)) = 2\pi m_f f_{LF} \left[J_0(z) \cos(2\pi f_{LF} t) - J_2(z) \cos(2\pi f_{LF} t - \varphi_1) \right]. \quad (4.22)$$

Inserting (4.21) and (4.22) in (4.16) and using the relation $J_1'(z) = \frac{1}{2}(J_0(z) - J_2(z))$, the signal at the output of the FM demodulator is finally given by

$$p(t) \simeq C \left[\cos(2\pi f_{LF} t) + 2A_1 J_1'(z) [\cos(2\pi f_{LF} t) + \cos(2\pi f_{LF} t - \varphi_1)] \right], \quad (4.23)$$

with C is a constant. In order to extract the bearing error, we search to express $p(t)$ in the following form

$$p(t) = A'(t) \cos(2\pi f_{LF} t - \tilde{\varphi}^D), \quad (4.24)$$

where $A'(t)$ is the envelope of the LF signal at the FM demodulator output and $\tilde{\varphi}^D$ is the information azimuth at the FM demodulator output.

Expanding the last cosine in (4.23), we end up with

$$\sin \tilde{\varphi}^D = 2 A_1 J_1'(z) \sin \varphi_1 \quad (4.25)$$

$$\cos \tilde{\varphi}^D = 1 + 2 A_1 J_1'(z) [1 + \cos \varphi_1]. \quad (4.26)$$

The bearing error is then expressed as

$$\varepsilon^D = \tan^{-1} \left(\frac{\sin \tilde{\varphi}^D}{\cos \tilde{\varphi}^D} \right) = \tan^{-1} \left(\frac{2 A_1 J_1'(z) \sin \varphi_1}{1 + 2 A_1 J_1'(z) [1 + \cos \varphi_1]} \right). \quad (4.27)$$

In the case of weak multipath, the arctangent can be assimilated to its angle. Finally, the DVOR error for single multipath is expressed as

$$\varepsilon^D = 2 A_1 J_1' \left(-2m_f \sin \left(\frac{\varphi_1}{2} \right) \right) \sin(\varphi_1). \quad (4.28)$$

This demonstration has been performed for the special case $a_0 = 1$, $\theta_0 = 0$, $\varphi_0 = 0$. Generalizing to any direct path and combining the contributions of several multipath, we finally obtain the I2Q-FM error expression

$$\varepsilon^{D,N} = 2 \sum_{n=1}^N \frac{a_n}{a_0} \cos(\theta_n - \theta_0) J_1' \left(-2m_f \sin \left(\frac{\varphi_n - \varphi_0}{2} \right) \right) \sin(\varphi_n - \varphi_0). \quad (4.29)$$

4.4.3 Validation

In this section, the I2Q-FM error given by (4.29) is validated by comparisons with results of the receiver model in canonical and complex realistic scenario.

4.4.3.a Canonical scenario

We consider the canonical multipath defined in Section 4.4.1. In Figure 4.14, we illustrate the DVOR error obtained by the Odunaiya expression, the I2Q-FM formulation and the simulation with our receiver model.

We can see a good agreement between the I2Q-FM error and the receiver model. We can also observe a discrepancy in the level of error between both expressions. The maximum error with I2Q-FM is 5 times greater than with the Odunaiya expression. Besides, these maximums do not correspond to the same value of relative multipath azimuth ($\varphi_1 - \varphi_0$): $\pm 6.5^\circ$ for the Odunaiya expression and $\pm 62^\circ$ or $\pm 76^\circ$ for the I2Q-FM formulation.

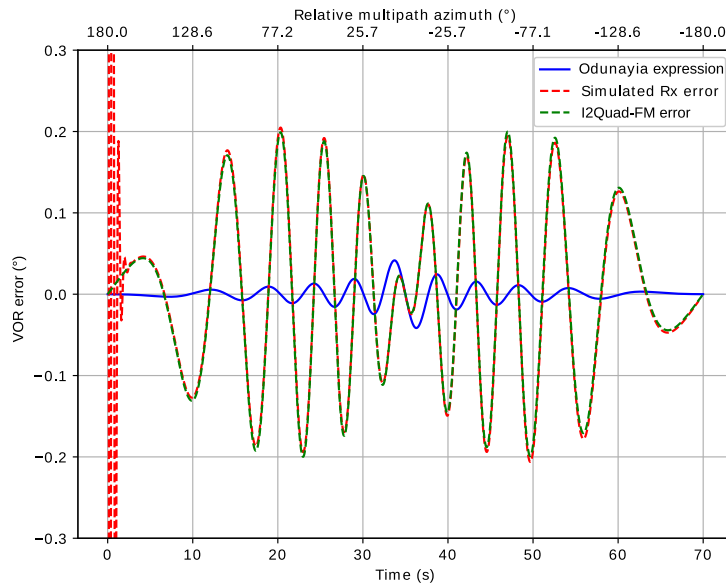
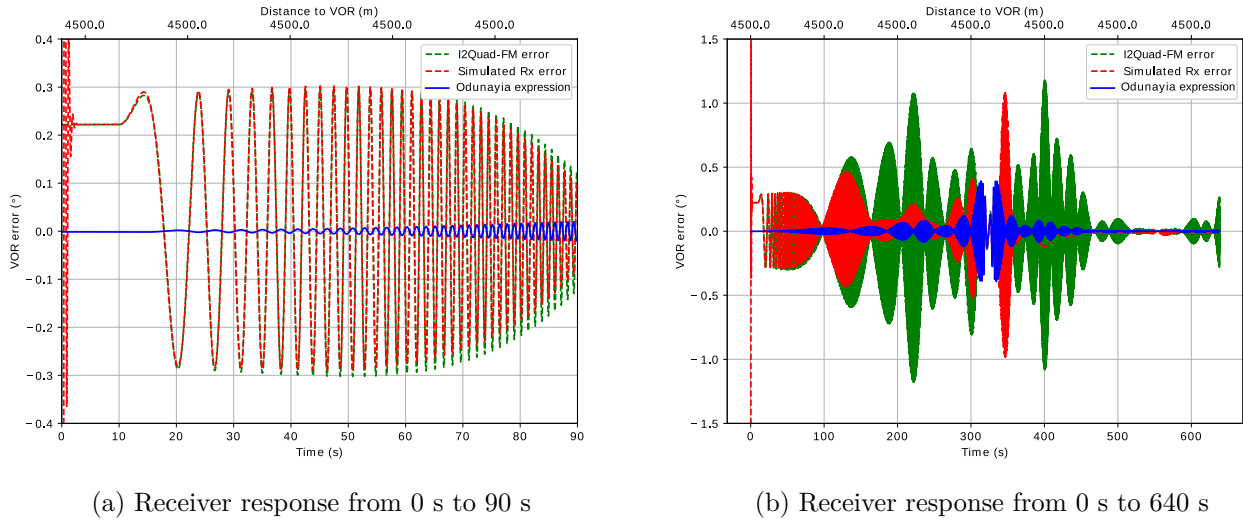


Figure 4.14: Validation of the I2Q-FM error in canonical scenario.

4.4.3.b Complex realistic scenario

The validation of the I2Q-FM error is also performed when multipath change with time in a complex realistic scenario. We consider configuration proposed in Section 4.3.1, except that we consider a DVOR station. In Figures 4.15a and 4.15b, the errors obtained by the Odunaiya expression, the I2Q-FM formulation and the simulation with our receiver model, are plotted using 2 time scales.



(a) Receiver response from 0 s to 90 s

(b) Receiver response from 0 s to 640 s

Figure 4.15: Validation of the I2Q-FM error in complex realistic scenario.

When the aircraft moves slowly at the beginning of the trajectory, a good agreement can be observed between the I2Q-FM formulation and the receiver model as shown in Figure 4.15a. When the aircraft accelerates, very low errors are observed in the receiver response despite the fast fluctuations seen in the I2Q-FM error as illustrated in Figure 4.15b. As for CVOR, the multipath might be filtered when its relative Doppler shift is high enough. However, this last claim is still to be demonstrated. A spectral analysis on the received intermediate signals could be useful to explain this phenomenon. A special focus on the applied FM demodulator could be also interesting. This is left as future works.

4.5 Multipath effect on the reference signal

The study of Bredemeyer [50] indicates that the surrounding environment (objects, noise, etc.) around a DVOR can impact the reference signal which is modulated in amplitude. This effect should be taken into account. The I2Q-FM error developed and validated in the previous section ignores the effect of multipath on the reference signal. We evaluate this phenomenon in this section.

4.5.1 Configuration

We here present the configuration proposed in order to evaluate the multipath effect on the reference signal. As shown in Figure 4.16, we consider an aircraft moving at 180 km/h from azimuth 0° to 90° along a circular trajectory around a DVOR station operating at a frequency of 113 MHz with a power of 50 W. The trajectory is characterized by a radius of 4.5 km and an altitude of 1 km. The aircraft is considered motionless at the first and last 10 s. The time series of multipath parameters are interpolated at a frequency of 25 kHz

in the I/Q signal generator. The filtering parameters of our digital receiver model are the same as in Section 2.4.1 (see Table 2.1).

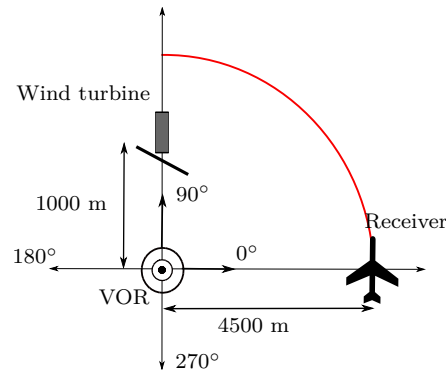


Figure 4.16: Top view of a circular aircraft trajectory from azimuth 0° to 90° around a DVOR.

4.5.2 Results

In order to evaluate separately the multipath effect on the VAR and REF channels, three cases are considered. For the first one, the multipath effect is considered only on the variable channel in the receiver model. The second one consists in assessing the multipath effect on the reference signal only. For the third one, all components of the multipath VAR and REF signals are taken into account in the processing of our receiver model. The relative multipath instantaneous frequency is illustrated in Figure 4.17. We show in Figure 4.18 the response of the receiver model for these three cases.

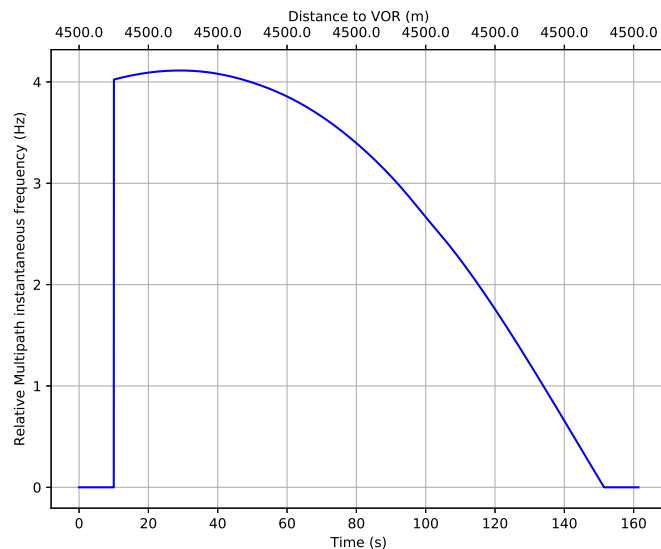


Figure 4.17: Relative multipath instantaneous frequency.

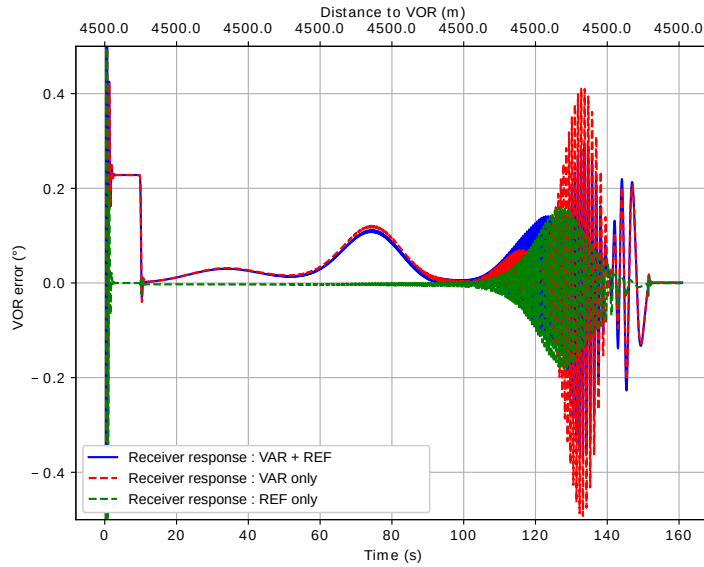


Figure 4.18: Comparison of multipath effects on VAR and REF channels.

When the phase difference between the direct signal and the multipath varies slowly at the end of the trajectory, a significant effect is seen on both channels. To explain the error generated on the REF channel between 120 s and 140 s as shown in Figure 4.18 (green line), we perform a spectral analysis of the received intermediate signals in the 30 Hz band-pass filter of the REF channel and the DC low-pass filter. The results are plotted in Figures 4.19a and 4.19b. We observe that both filters allow the multipath signal with Doppler shift which varies from 0.7 Hz to 1.7 Hz around the direct signal at 30 Hz to pass through. This explains the fluctuations of the receiver response.

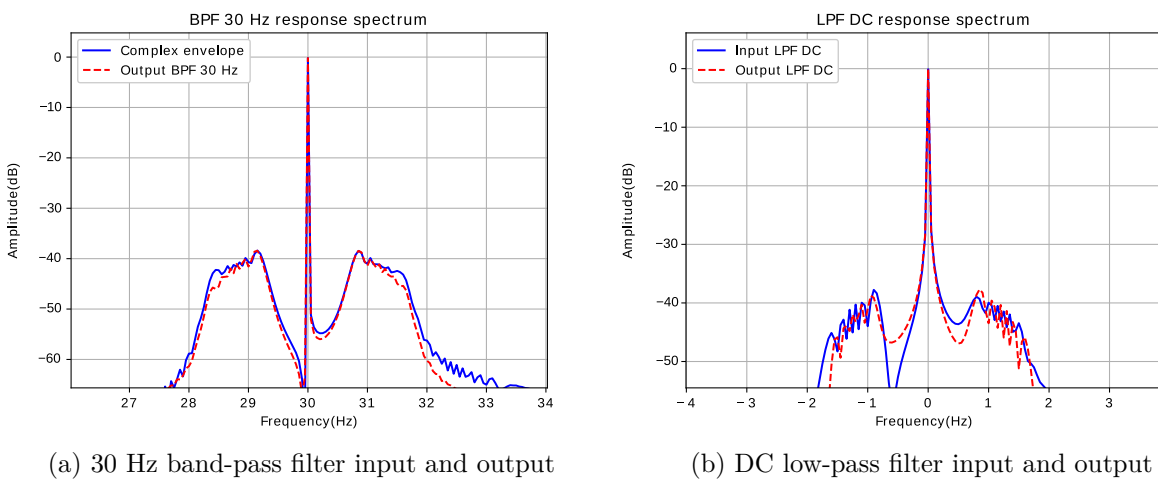


Figure 4.19: Normalized spectrum of the input and output of receiver filters.

4.5.3 Conclusion

As to conclude, we have shown that, for DVOR, the REF channel of the receiver seems to be sensitive to multipath. This may be explained by the amplitude modulation that is used for this signal. This is independent of the type of FM demodulator. This effect is ignored in the analytical I2Q-FM error and the Odunaiya expression. This result is consistent with the analysis performed by Bredemeyer [50]. Nevertheless, these analyses should be confirmed by performing a more complete study for other scenarios and with other types of FM demodulator.

4.6 Conclusion

An overview of the main results of this chapter is given in Table 4.1.

<p>CVOR/DVOR receiver group delay</p> <ul style="list-style-type: none"> The group delay of the digital receiver model is given by $\tau_g^{\text{tot}} = \tau_g^{\text{BPF}} + \tau_g^{\text{LPF}}$	<p>CVOR validity domain of Odunaiya error</p> <ul style="list-style-type: none"> Odunaiya error is valid when $f_0 \frac{V_{Rx}}{c_0} \hat{\mathbf{r}}_{\text{wt}} \cdot \hat{\mathbf{u}}_{\text{m}} < \min\left(\frac{W_{30}}{2}, W_{\text{DC}}\right)$
<p>DVOR I2Q-FM error</p> <ul style="list-style-type: none"> Demonstration of the error expression (4.29) Consistent with the quadrature FM demodulator Validation in canonical and realistic complex scenarios 	<p>DVOR multipath effect on REF signal</p> <ul style="list-style-type: none"> REF signal is sensitive to multipath This effect has been evaluated by simulation Bearing error expressions ignore this effect

Table 4.1: Overview of the main results of this chapter.

Our digital VOR receiver model has been analyzed in this chapter. The receiver group delay has been evaluated according to the filtering parameters. A method to determine the validity domain of the Odunaiya expression for computing the CVOR multipath error has been presented. The expression is no longer valid when the multipath is strongly attenuated by the receiver filter. This happens when its relative Doppler shift is large enough with respect to the filter bandwidths. A geometric criterion that defines this domain has been given and illustrated. We have shown that the DVOR error is sensitive to the type of the FM demodulator. We have developed an expression, the I2Q-FM error, consistent with the quadrature FM demodulator used in our receiver model. We have shown that the reference signal is sensitive to multipath for DVOR. As stated by the Bredemeyer's analysis, this effect should be considered in the computation of the DVOR error. Nevertheless, this should be confirmed with other scenarios and with a receiver using other types of components.

Chapter 5

Statistical Model of the CVOR Bearing Error

5.1 Introduction

The computation of multipath characteristics with the VERSO simulator usually requires high computational resources. Moreover, the configuration must be perfectly known. An alternative model providing the statistical distribution of the bearing error from few parameters would be useful. Therefore, we here propose a first step towards such a model. A statistical model for the CVOR multipath error is introduced for which the distances VOR-aircraft and VOR-wind turbine are fixed whereas the other parameters (wind turbine size, materials, ground composition, etc.) follow statistical distributions. Our approach is based on a Monte-Carlo analysis.

In Section 5.2, we define the configuration and the statistical distributions of the input parameters. We present in Section 5.3 the principle of our model by determining the statistical distributions of the multipath parameters and the CVOR error. We show that, for any aircraft and wind turbine position, the distributions only depend on one parameter that can be assessed by means of a Monte-Carlo analysis performed using VERSO. In Section 5.4, we present the principle of the Monte-Carlo analysis. We show and analyze in Section 5.5 the results of a test-case for which the distances between the VOR and the wind turbine, and between the wind turbine and the aircraft are fixed.

5.2 Configuration

In this section, we define the general configuration and the hypotheses to be considered in our statistical model.

5.2.1 Deterministic parameters

As shown in Figure 5.1, we consider one wind turbine of known approximate position \mathbf{r}_{w_0} . For the sake of simplicity, the coordinate system is chosen so that this approximate position is along the $\hat{\mathbf{x}}$ axis. We assume that this wind turbine yields one multipath with moderate amplitude. The VOR characteristics and the aircraft position are assumed to be known.

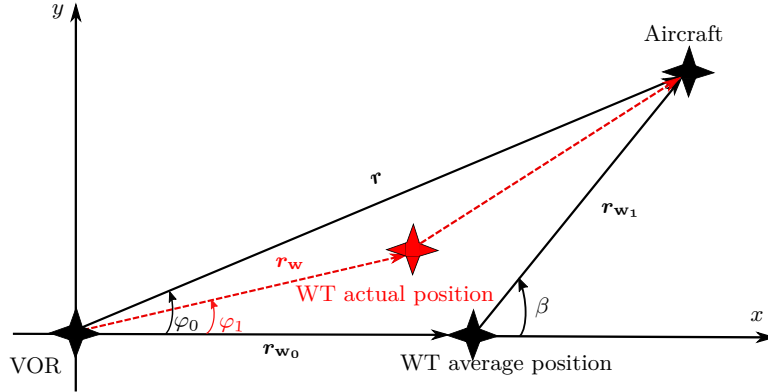


Figure 5.1: Top view of the configuration and notation for the statistical model.

5.2.2 Statistical parameters

We consider that the variation of the wind turbine position about its average value follows independent normal distributions along $\hat{\mathbf{x}}$ and $\hat{\mathbf{y}}$ of standard deviations σ_w . This parameter is assumed to be small compared to the distances from VOR to wind turbine $\|\mathbf{r}_{w_0}\|$ and from wind turbine to aircraft $\|\mathbf{r}_{w_1}\|$,

$$\sigma_w \ll \|\mathbf{r}_{w_0}\|, \|\mathbf{r}_{w_1}\|. \quad (5.1)$$

The other configuration parameters are supposed to follow statistical distributions. The ground is assumed planar and its relative permittivity follows a discrete uniform distribution, which values are associated with water, snow, dry or humid soils, etc. We suppose that the characteristics and orientation of the wind turbine which are defined in Figure 1.14 follow uniform and normal distributions.

For this configuration and these hypotheses, we search to determine the statistics of the CVOR error. This is the aim of the next section.

5.3 Model principle

Our model consists firstly in determining the statistical distributions associated with the multipath parameters. Secondly, the statistical distribution of the CVOR bearing error is deduced from the Odunayia expression. We remind that this expression is conservative.

We assume that the relative amplitude of multipath follows a Rayleigh distribution as explained in Section 5.3.1. We verify in Section 5.3.2 that the relative phase of multipath follows a uniform distribution. In Section 5.3.3, we show that the relative azimuth of multipath is approximately constant. We then explain that the CVOR bearing error follows a centered normal distribution in Section 5.3.4.

5.3.1 Relative amplitude distribution

We know that the total wind turbine scattering corresponds to the sum of the scattering of the wind turbine components. These latter randomly vary by following statistical distributions. Despite this is not fully justified, we suppose that the fields scattered by facets are independent. Therefore, we assume that the relative multipath amplitude follows a Rayleigh distribution of standard deviation σ according to the central limit theorem [51]. It is characterized by a probability density function expressed as

$$f(x) = \frac{x}{\sigma^2} \exp\left(\frac{-x^2}{2\sigma^2}\right), x \geq 0. \quad (5.2)$$

This hypothesis will be tested by means of simulations.

5.3.2 Relative phase distribution

5.3.2.a Computation

The absolute multipath phase varies rapidly in space. The objective of this section is to assess if the relative phase of the multipath follows a uniform distribution.

The actual position of the wind turbine is defined by

$$\mathbf{r}_w = \mathbf{r}_{w_0} + \delta\mathbf{w}, \quad (5.3)$$

where $\delta\mathbf{w}$ is the vector variation of the wind turbine's position with respect to its average value \mathbf{r}_{w_0} . Since the position of the wind turbine follows normal distributions along $\hat{\mathbf{x}}$ and $\hat{\mathbf{y}}$, we have

$$\delta\mathbf{w} = \delta w_x \hat{\mathbf{x}} + \delta w_y \hat{\mathbf{y}}. \quad (5.4)$$

where δw_x and δw_y follow independent centered normal distributions of standard deviations σ_w .

We first search to characterize the statistical distribution of the multipath length with respect to the direct path. This length is given by

$$\begin{aligned}
\delta d &= \|\mathbf{r}_w\| + \|\mathbf{r} - \mathbf{r}_w\| - \|\mathbf{r}\| \\
&= \|\mathbf{r}_{w_0} + \delta\mathbf{w}\| + \|\mathbf{r} - \mathbf{r}_{w_0} - \delta\mathbf{w}\| - \|\mathbf{r}\| \\
&= \|\mathbf{r}_{w_0} + \delta\mathbf{w}\| + \|\mathbf{r}_{w_1} - \delta\mathbf{w}\| - \|\mathbf{r}\| \\
&= \sqrt{\|\mathbf{r}_{w_0}\|^2 + 2\mathbf{r}_{w_0} \cdot \delta\mathbf{w} + \|\delta\mathbf{w}\|^2} + \\
&\quad \sqrt{\|\mathbf{r}_{w_1}\|^2 - 2\mathbf{r}_{w_1} \cdot \delta\mathbf{w} + \|\delta\mathbf{w}\|^2} - \|\mathbf{r}\|.
\end{aligned} \tag{5.5}$$

Upon assuming (5.1), we apply a first-order Taylor series approximation on the term $\|\delta\mathbf{w}\|$, so that

$$\delta d = \|\mathbf{r}_{w_0}\| + \|\mathbf{r}_{w_1}\| - \|\mathbf{r}\| + (\hat{\mathbf{r}}_{w_0} - \hat{\mathbf{r}}_{w_1}) \cdot \delta\mathbf{w}, \tag{5.6}$$

with $\hat{\mathbf{r}}_{w_0} = \mathbf{r}_{w_0}/\|\mathbf{r}_{w_0}\|$ and $\hat{\mathbf{r}}_{w_1} = \mathbf{r}_{w_1}/\|\mathbf{r}_{w_1}\|$. To further simplify the calculation, we note β the angle between the VOR-wind turbine axis and the wind turbine-aircraft axis as shown in Figure 5.1. We can then write

$$\hat{\mathbf{r}}_{w_0} = \hat{\mathbf{x}}, \quad \hat{\mathbf{r}}_{w_1} = \cos(\beta) \hat{\mathbf{x}} + \sin(\beta) \hat{\mathbf{y}}. \tag{5.7}$$

Inserting (5.4) and (5.7) in (5.6), we obtain

$$\delta d = \|\mathbf{r}_{w_0}\| + \|\mathbf{r}_{w_1}\| - \|\mathbf{r}\| + (1 - \cos(\beta)) \delta w_x - \sin(\beta) \delta w_y. \tag{5.8}$$

Therefore, we deduce that the relative multipath length δd follows a normal distribution characterized by a mean $\mu_{\delta d}$ given by

$$\mu_{\delta d} = \|\mathbf{r}_{w_0}\| + \|\mathbf{r}_{w_1}\| - \|\mathbf{r}\|, \tag{5.9}$$

and a standard deviation $\sigma_{\delta d}$ defined by

$$\sigma_{\delta d} = \sqrt{(1 - \cos(\beta))^2 + \sin^2(\beta)} \sigma_w = 2 \sin\left(\frac{|\beta|}{2}\right) \sigma_w. \tag{5.10}$$

The relative multipath phase can be expressed as

$$\delta\theta = \arg(e^{jk\delta d}). \tag{5.11}$$

As will be numerically shown in Section 5.3.2.b, the relative multipath phase $\delta\theta$ follows a uniform distribution on $[0, 2\pi]$ if

$$\sigma_{\delta d} \geq \frac{\lambda}{2}. \tag{5.12}$$

From (5.10) and (5.12), the relative multipath phase approximately follows a uniform distribution except for

$$|\beta| \leq 2 \sin^{-1} \left(\frac{\lambda}{4\sigma_w} \right). \quad (5.13)$$

According to the Odunaiya expression, the error is null when β tends to zero. Therefore, the relative multipath phase varies uniformly except in a region where the bearing error is weak if the standard deviation σ_w is of order of few λ .

5.3.2.b Numerical verification and illustration

We consider an example with typical values: a VOR frequency of 113 MHz and a standard deviation σ_w that varies between λ and 10λ . Using (5.13), the angles above which the relative multipath phase follows a uniform distribution on $[0, 2\pi]$ are illustrated in Figure 5.2.

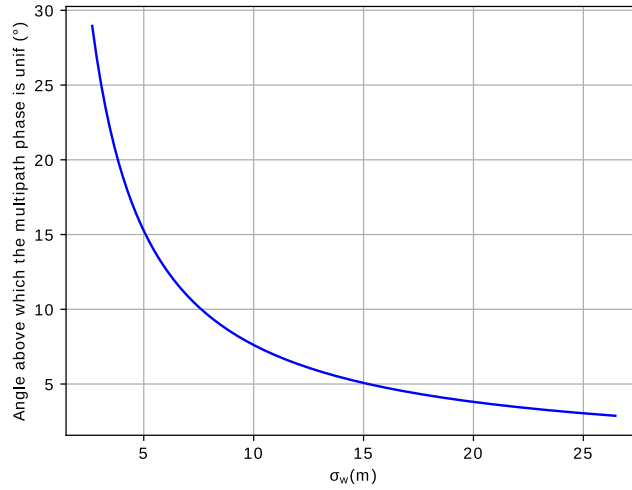


Figure 5.2: Angles above which the relative multipath phase is uniform.

In order to verify that the relative multipath phase $\delta\theta$ follows a uniform distribution if (5.12) is fulfilled, we perform a Kolmogorov-Smirnov test (K-S test) [52]. This test is characterized by a statistic D_{K-S} which quantifies the maximum difference in distance between the empirical distribution function (EDF) of the sample and the cumulative distribution function (CDF) of the reference distribution which is of uniform type in this test. We consider a standard deviation σ_{δ_d} that varies between $\lambda/10$ and λ . Figure 5.3 shows the evolution of the statistic D_{K-S} with respect to $\sigma_{\delta_d}/\lambda$. When this latter increases, the relative multipath phase approximates to a uniform distribution since D_{K-S} becomes neglectable.

We show in Figure 5.4 the histogram of the distribution associated with the relative multipath phase for $\sigma_{\delta_d} = 0.25\lambda$ and $\sigma_{\delta_d} = 0.5\lambda$. We observe that when σ_{δ_d} is equal to 0.5λ , the histogram becomes flat on $[0, 2\pi]$. In this case, we can confirm that the relative multipath phase follows a uniform distribution.

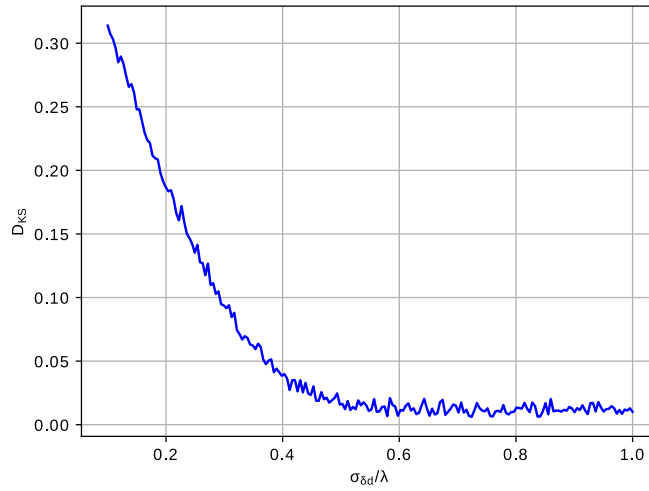


Figure 5.3: Results of the Kolmogorov-Smirnov test on the relative multipath phase.

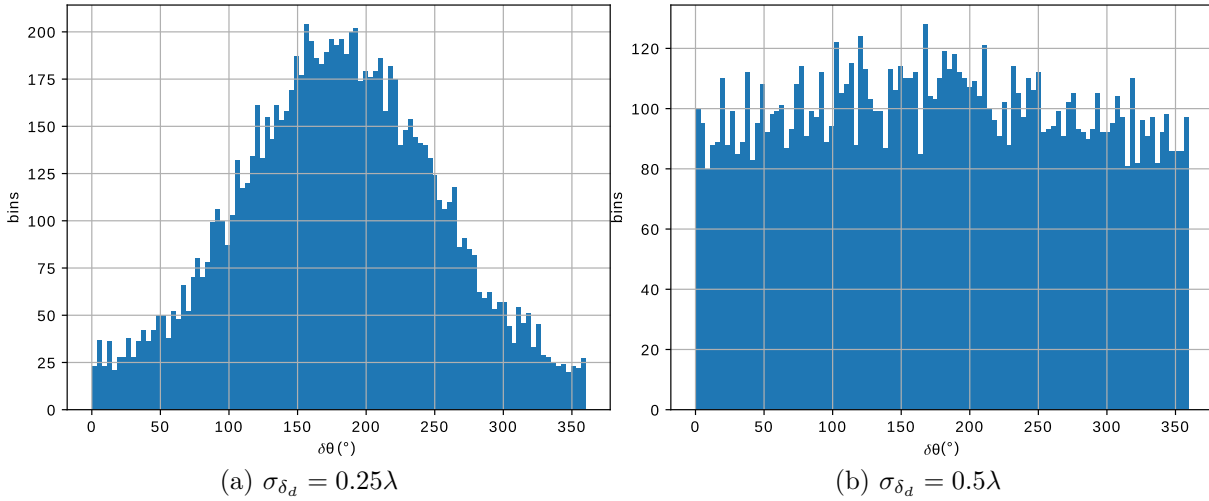


Figure 5.4: Histogram of the distribution associated with the relative multipath phase for different values of σ_{δ_d} .

5.3.3 Relative azimuth distribution

Based on the Odunaiya expression for CVOR error, we here search to determine the statistical distribution followed by the term $\sin(\varphi_1 - \varphi_0)$. This latter is expressed as

$$\sin(\varphi_1 - \varphi_0) = \sin(\varphi_1) \cos(\varphi_0) - \cos(\varphi_1) \sin(\varphi_0). \quad (5.14)$$

The standard deviation σ_w is taken to be small compared to the distance from VOR to wind turbine. Therefore, we can perform the following simplifications

$$\begin{aligned}\sin(\varphi_1) &\simeq \frac{\delta w_y}{\|\mathbf{r}_{\mathbf{w}_0}\|} \\ \cos(\varphi_1) &\simeq 1.\end{aligned}\tag{5.15}$$

Inserting (5.15) in (5.14), we obtain

$$\sin(\varphi_1 - \varphi_0) = \delta w_y \frac{\cos(\varphi_0)}{r_{\mathbf{w}_0}} - \sin(\varphi_0).\tag{5.16}$$

with $r_{\mathbf{w}_0} = \|\mathbf{r}_{\mathbf{w}_0}\|$. Therefore, we deduce that the term $\sin(\varphi_1 - \varphi_0)$ follows a normal distribution of mean $-\sin(\varphi_0)$ and standard deviation given by

$$\sigma_{\delta\varphi} = \frac{|\cos(\varphi_0)|}{r_{\mathbf{w}_0}} \sigma_w \leq \frac{\sigma_w}{r_{\mathbf{w}_0}}.\tag{5.17}$$

Upon assuming (5.1), $\sigma_{\delta\varphi}$ is very small. Thus, in the following, we consider that $\sin(\varphi_1 - \varphi_0) \approx -\sin(\varphi_0)$.

To test this hypothesis, we consider an example of a wind turbine placed at 500 m from the VOR. The standard deviation of its position variation is defined at 10 m. We find that $\sigma_{\delta\varphi} = 0.02$. Therefore, we consider in our study that the multipath azimuth is deterministic. It corresponds to the one of the average position of the wind turbine.

5.3.4 CVOR error distribution

The probability distributions of the multipath parameters have been determined in the previous sections. We here determine the statistical distribution of the CVOR bearing error.

From the general Odunaiya expression for CVOR given in (1.27), the bearing error for a multipath with moderate amplitude is expressed as

$$\varepsilon_{\text{Od}}^{\text{C}} = \frac{a_1}{a_0} \cos(\theta_1 - \theta_0) \sin(\varphi_1 - \varphi_0).\tag{5.18}$$

The CVOR error depends on three main parameters: the relative amplitude a_1/a_0 , the phase $(\theta_1 - \theta_0)$ and the azimuth $(\varphi_1 - \varphi_0)$ of the multipath. In Section 5.3.1, we have shown that the relative multipath amplitude follows a Rayleigh distribution of parameter σ_1 . As explained in Section 5.3.2, the relative multipath phase $(\theta_1 - \theta_0)$ follows a uniform distribution on $[0, 2\pi]$ when the criterion (5.13) is fulfilled. Thus, the term $\frac{a_1}{a_0} \cos(\theta_1 - \theta_0)$ follows a centered normal distribution [53]. The relative multipath azimuth is supposed deterministic as explained in Section (5.3.3). Therefore, the error $\varepsilon_{\text{Od}}^{\text{C}}$ follows a centered normal distribution of standard deviation given by

$$\sigma_1^\varepsilon = \sigma_1 |\sin(\varphi_1 - \varphi_0)|.\tag{5.19}$$

We can generalize this expression for N wind turbines. As shown in [24], the shadowing effects between wind turbines are neglectable at VOR frequency. Therefore, the statistical distributions associated with several multipath can be considered independent. The error due to a farm of N wind turbines then follows a centered normal distribution of standard deviation expressed by

$$\sigma_N^\varepsilon = \sqrt{\sum_{n=1}^N \sigma_n^2 \sin^2(\varphi_n - \varphi_0)}. \quad (5.20)$$

In this PhD thesis, no simulations are presented about this generalized expression. In order to characterize the multipath error, we need to assess one parameter which is the parameter of the Rayleigh distribution. This is the aim of the next section.

5.4 Monte-Carlo Analysis

The Monte-Carlo analysis is performed in order to assess the parameter of the Rayleigh distribution. The flowchart of this analysis is presented in Figure 5.5. The principle is to run the VERSO simulator for several samples of the input random parameters until the parameter of the Rayleigh distribution converges.

Firstly, we define the deterministic parameters which are the average position of the wind turbine, the VOR characteristics and the aircraft position. Secondly, for each iteration in the Monte-Carlo loop, the random parameters are generated. The multipath parameters are then computed with VERSO simulator. An unbiased estimator of $\hat{\sigma}_1^2(m)$ is

$$\hat{\sigma}_1^2(m) = \frac{1}{2m} \sum_{k=1}^m \left(\frac{a_1(k)}{a_0(k)} \right)^2, \quad (5.21)$$

where m is the total number of performed simulations. The convergence criterion is given by

$$\max_{\Theta_0, \varphi_0} \left(\left| \frac{\hat{\sigma}_1(N_m) - \hat{\sigma}_1(N_m - j)}{\hat{\sigma}_1(N_m)} \right| \right) \leq \delta_{\text{conv}}, \forall j \in [1, \dots, L_{\text{conv}}], \quad (5.22)$$

where Θ_0 and φ_0 are the observation angles in the spherical coordinate system, N_m is the the number of Monte-Carlo iterations at convergence, L_{conv} is the number of previous iterations used to check the convergence, and δ_{conv} is the convergence threshold. When the convergence is reached, the parameter of Rayleigh distribution is obtained. Then, we can deduce from (5.19) the parameter of the standard deviation of the centered normal distribution followed by the CVOR error.

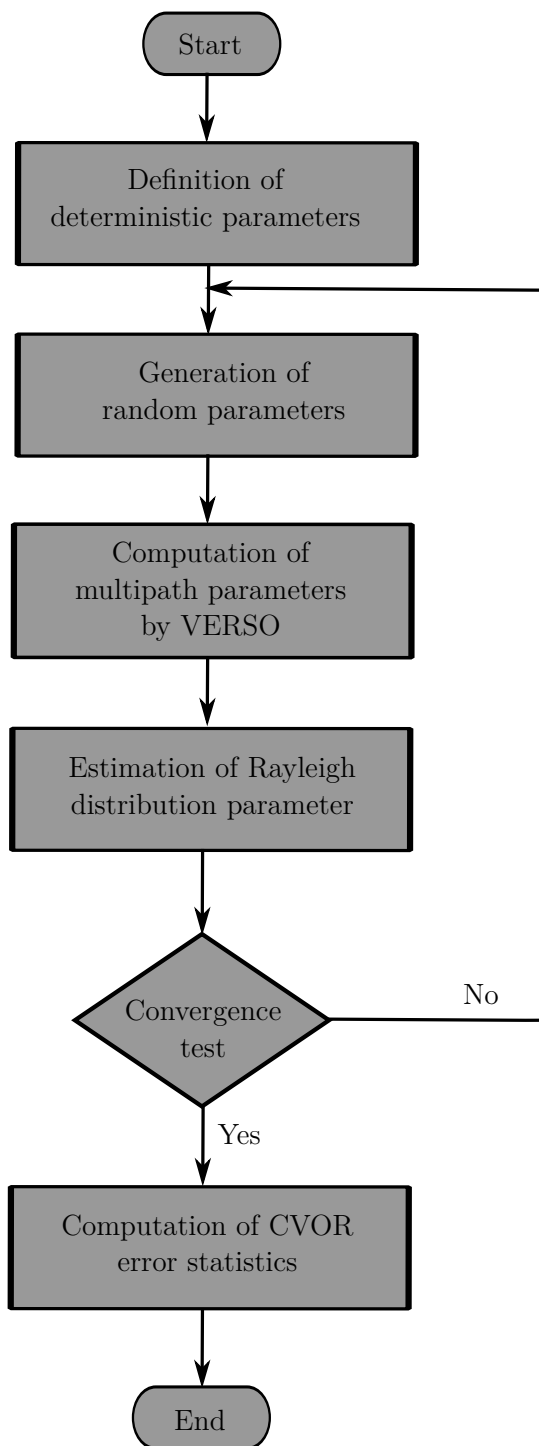


Figure 5.5: Flowchart of Monte-Carlo study.

We present in the next section a test-case.

5.5 Test-case

In the previous section, we have explained the general method for assessing the parameter of the Rayleigh distribution using Monte-Carlo analysis. A test-case is here presented for which the distances between the VOR and the wind turbine, and between the wind turbine and the aircraft are fixed. The statistical parameters of the configuration are given in Section 5.2.

5.5.1 Presentation of the test-case

5.5.1.a Deterministic parameters

We consider a CVOR station operating at a frequency of 113 MHz with a power of 50 W. A wind turbine is placed at 3 km from the VOR station on radial 0° . The observation is defined on a half sphere of radius 10 km centered on the wind turbine. Above the VOR station, there exists a blind cone inside which no observation points are placed. We consider here a blind cone of angle 40° which is consistent with usual values [15]. The configuration is illustrated in Figure 5.6. For the convergence test, we consider a threshold of $\delta_{\text{conv}} = 5\%$ and we take into account $L_{\text{conv}} = 10$ previous iterations.

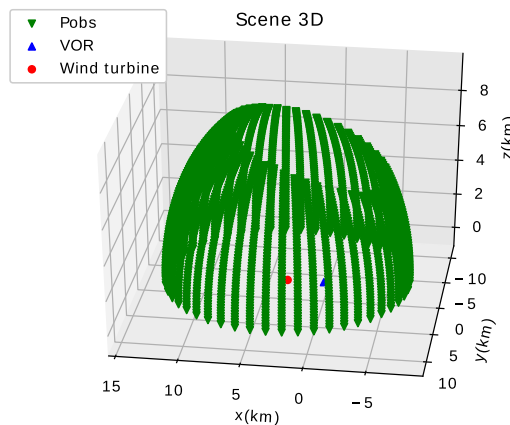


Figure 5.6: Proposed configuration for Monte-Carlo simulations.

5.5.1.b Random parameters

The dielectric ground type varies randomly by following a discrete uniform distribution. The characteristics of the grounds included in the Monte-Carlo simulations are given in Table 5.1.

The wind turbine position has a standard deviation of 10 m. The simulation is performed with the parameters given in Table 5.2. The values have been chosen from the database about wind turbines in the North of France presented in Appendix C. These values are used for our particular test-case. These values may not be consistent for all wind farms.

Type	Permittivity ε_g	Conductivity σ_g (S.m ⁻¹)
humid	25	0.02
dry	5	0.001
salty water	80	5
water	80	0.01
ice	3	1e-6
fresh snow	1.5	0.0005
conductor	0.03	5e7

Table 5.1: Characteristics of the dielectric grounds included in the Monte-Carlo simulations.

Wind turbine parameter	Distribution mode	Distribution parameters
Mast		
Height H	normal	$\mu = 95$ m, $\sigma = 21$ m
Ground diameter D_1	uniform	[3, 5] m
Top diameter D_2	uniform	[1, 3] m
Nacelle		
Length h_1	uniform	[11, 15] m
Height h_2	uniform	[4, 8] m
Width h_3	uniform	[4, 8] m
Nacelle-mast distance d_{nm}	uniform	[0, 1.5] m
Blade-nacelle orientation α_a	uniform	[0, 360]°
Blade		
Length ratio blade/mast $\frac{L_2}{H}$	normal	$\mu = 0.6$, $\sigma = 0.1$
Trapezoid length ratio $\frac{L_1}{L_2}$	uniform	[0.1615, 0.1785]
Initial width ratio $\frac{l_1}{L_2}$	uniform	[0.0180, 0.0199]
Maximal width ratio $\frac{l_2}{L_2}$	uniform	[0.0266, 0.0294]
Final width ratio $\frac{l_3}{L_2}$	uniform	[0.0085, 0.0094]
Hub-nacelle distance ratio $\frac{d_p}{L_2}$	uniform	[0.0665, 0.0735]
Nacelle-blade distance $d_{np} - \frac{h_1}{2}$	uniform	[0.5, 1.5] m
Blade/hub orientation α_m	uniform	[0, 120]°
Blade/long. axis orientation α_p	uniform	[-1, 1]°
Blade/vert. axis orientation α_v	uniform	[-1, 1]°
Dielectric layer thickness w_l	uniform	[0.022, 0.066] m
Dielectric layer permittivity ε_l	uniform	[2.5, 7.5]
Dielectric layer conductivity σ_l	uniform	[0.05, 0.15] S.m ⁻¹

Table 5.2: Proposed distributions parameters associated with the wind turbine characteristics defined in Figure 1.14.

5.5.2 Results

In this section, the results of Monte-Carlo simulations are presented and analyzed.

5.5.2.a Convergence

We here illustrate the convergence of the estimated parameter in the Monte-Carlo simulations and we introduce confidence intervals. We find that 574 simulations have been performed in order to reach convergence. The computation took approximately 15 hours on a standard workstation with an i7 8C CPU and 16 Go of RAM.

When estimating a statistical parameter from a set of data, a convergence error exists. For $\hat{\sigma}_1$ the estimated standard deviation and σ_1 the real standard deviation, the estimation error ε_σ is defined by the relation

$$\varepsilon_\sigma = \hat{\sigma}_1 - \sigma_1. \quad (5.23)$$

We cannot compute this error, but we can assume that $\hat{\sigma}_1$ equals σ_1 within specified tolerance limits: the confidence interval. We here use the confidence interval associated with normal distributions. According to [54], we have the confidence interval

$$\sqrt{\frac{(m-1)\hat{\sigma}_1^2}{\chi_{1-\Delta/2}^2(m-1)}} < \sigma_1 < \sqrt{\frac{(m-1)\hat{\sigma}_1^2}{\chi_{\Delta/2}^2(m-1)}}, \quad (5.24)$$

where $\chi_u^2(m-1)$ is the Chi-square percentile which is given in [54]. Δ is the confidence level.

Figure 5.7 presents the corresponding parameter of the Rayleigh distribution computed at each iteration for the observation point $(\Theta_0, \varphi_0) = (88^\circ, 90^\circ)$. We choose this observation point to visualize the results because the CVOR error is predicted to be significant in this zone.

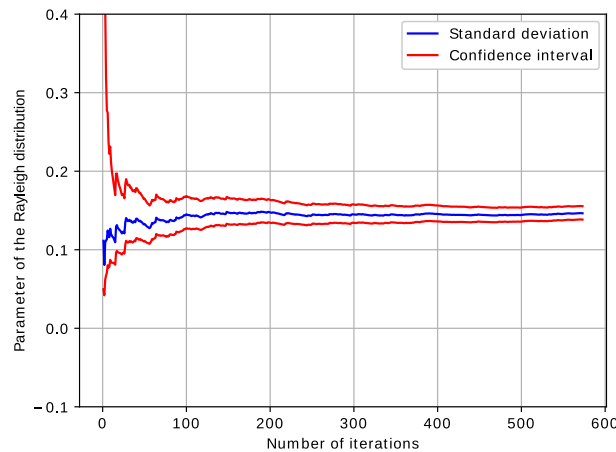


Figure 5.7: Parameter of the Rayleigh distribution and confidence interval for $\Delta = 95\%$.

We observe a relatively rapid convergence of the CVOR error parameter. We also show the confidence interval for the parameter of the Rayleigh distribution for $\Delta = 95\%$. In agreement with theory, we observe that the confidence interval becomes thinner when the number of iterations increases.

5.5.2.b Verification of the distributions chosen for the multipath parameters

We have assumed in Section 5.3.1 that the relative multipath amplitude follows a Rayleigh distribution. The relative multipath phase follows a uniform distribution on $[0, 2\pi]$ when the criterion (5.13) is fulfilled as explained in Section 5.3.2. In order to verify these hypotheses, we perform a Kolmogorov-Smirnov test (K-S test) on the multipath parameters. Therefore, we evaluate the parameter D_{K-S} with a comparison between the empirical distribution function (EDF) of the relative multipath amplitude and the cumulative distribution function (CDF) of different types of reference distributions: Rayleigh, normal, Rice and uniform. We choose to perform this test for the observation point at $\Theta_0 = 88^\circ$ and $\varphi_0 = [0^\circ, 90^\circ, 180^\circ, 270^\circ]$. Tables 5.3 and 5.4 show the results of the Kolmogorov-Smirnov test on the relative multipath amplitude and phase, respectively.

	$\varphi_0 = 0^\circ$	$\varphi_0 = 90^\circ$	$\varphi_0 = 180^\circ$	$\varphi_0 = 270^\circ$
Rayleigh	0.064	0.131	0.391	0.209
Normal	0.368	0.412	0.621	0.551
Rice	0.127	0.213	0.365	0.332
Uniform	0.841	0.722	0.621	0.842

Table 5.3: Results of the Kolmogorov-Smirnov test on the relative multipath amplitude.

	$\varphi_0 = 0^\circ$	$\varphi_0 = 90^\circ$	$\varphi_0 = 180^\circ$	$\varphi_0 = 270^\circ$
Rayleigh	0.629	0.712	0.812	0.804
Normal	0.119	0.522	0.588	0.491
Rice	0.839	0.635	0.628	0.771
Uniform	0.212	0.058	0.087	0.092

Table 5.4: Results of the Kolmogorov-Smirnov test on the relative multipath phase.

For the relative multipath amplitude, we can observe that the D_{K-S} value associated with the Rayleigh distribution is generally the smallest compared with other distributions. Nevertheless, for some directions, this value is significant. This is due to the weak relative multipath amplitude in these directions.

For the relative phase, the D_{K-S} value associated with the uniform distribution is neglectable except for $\varphi_0 = 0^\circ$ when the VOR, the wind turbine and the aircraft are in the same direction. This is explained in Section 5.3.2. Thus, the distributions chosen for the multipath parameters are verified.

5.5.2.c Estimated multipath Rayleigh parameter

In Figures 5.8 and 5.9, we show the parameter of the Rayleigh distribution associated with the relative multipath amplitude in 2D and 3D representations, respectively. As expected, the relative multipath is powerful in the zone behind the wind turbine for high Θ_0 angles, *i.e.* angles few degrees above the horizon as shown in Figures 5.8a and 5.8b. This zone corresponds to the specular diffraction zone of the mast. It is determined by the Snell's law as illustrated in Figure 5.10. Since we illustrate the multipath amplitude normalized with respect to the direct signal, we can't observe the second specular diffraction zone in front of the mast, *i.e.* the direction $\varphi_0 = 180^\circ$. Indeed, the direct path is dominant in this zone because the distance VOR aircraft is really smaller than the distance wind turbine aircraft. For medium Θ_0 angles, *i.e.* angles between 40° and 70° , we observe a residual contribution which is due to the blades.

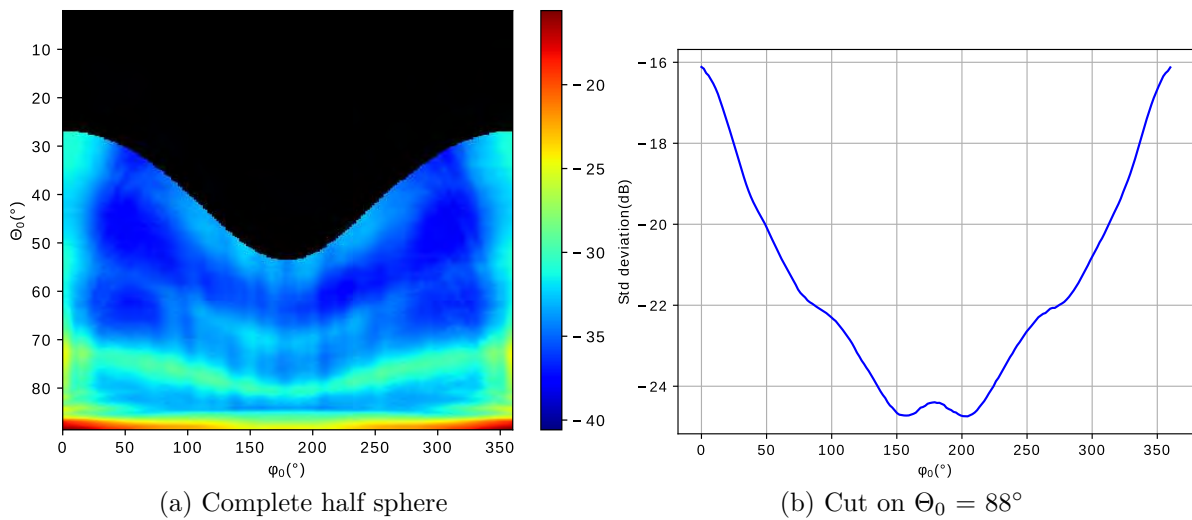


Figure 5.8: 2D representation of the parameter of the Rayleigh distribution associated with the relative multipath amplitude.

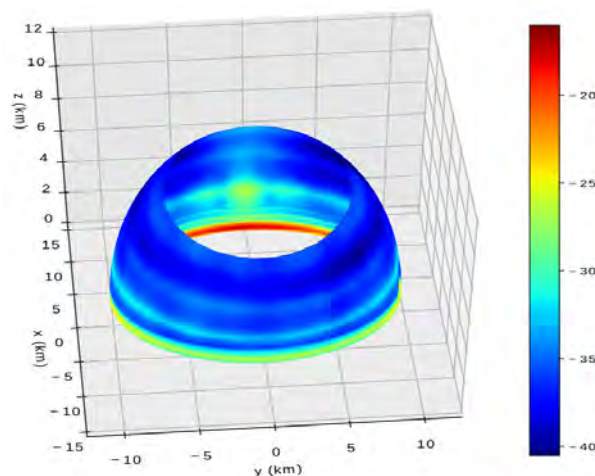


Figure 5.9: 3D representation of the parameter of the Rayleigh distribution associated with the relative multipath amplitude.

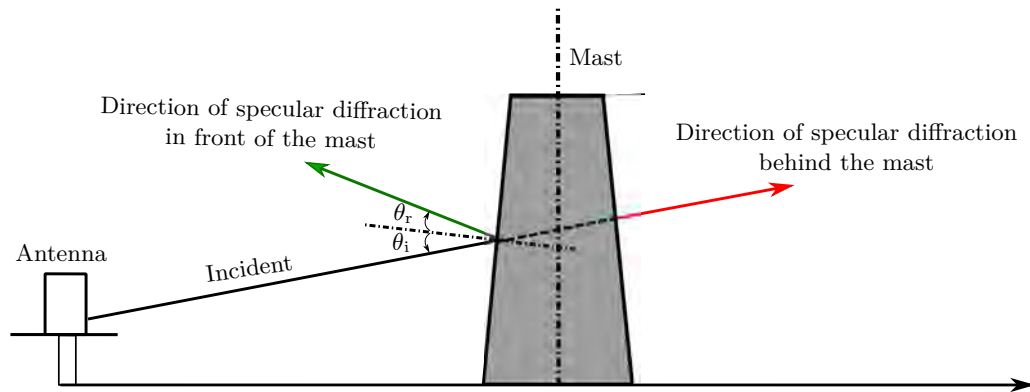


Figure 5.10: Main directions of specular diffraction by the mast.

5.5.2.d Standard deviation of the estimated bearing error

Figure 5.11 shows the standard deviation of the centered normal distribution associated with the bearing error computed by (5.19). As expected, we observe that this error is equal to zero when the VOR station, the wind turbine and the aircraft are in the same direction, *i.e.* the directions 0 and 180° as shown in Figures 5.11a and 5.11b. For high Θ_0 angles, the standard deviation of the bearing error reaches a maximum of 0.3° towards azimuth 90° and 270° . We observe in Figure 5.11b fluctuations when the standard deviation of the CVOR error is greater than 0.15° . They are of smaller amplitude than the 95% confidence. Thus, they may be associated with convergence of Monte-Carlo simulations.

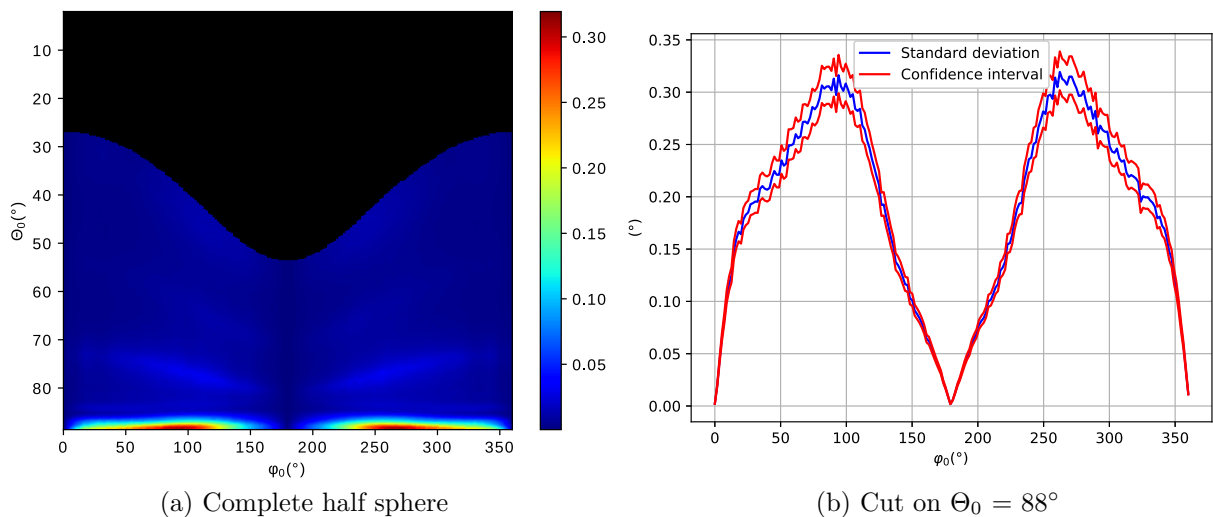


Figure 5.11: Standard deviation of the centered normal distribution associated with the bearing error.

5.6 Conclusion

In this chapter, a statistical model for the CVOR multipath error has been presented. This model provides the statistical distribution of the bearing error when wind turbine size, materials, ground composition, etc follow statistical distributions. Our model is based on a Monte-Carlo analysis. This approach could be used in future works to develop a complete statistical model in order to quantify the standard deviation of the VOR error from few parameters without running complete VERSO simulations. The configuration and the statistical distributions of the input parameters have been defined. The model principle has been presented by determining the statistical distributions of the multipath parameters and CVOR error. We have found that for a wind turbine of approximately known position and at a given observation point, the multipath approximately has a uniform relative phase, a constant relative azimuth and a Rayleigh relative amplitude. From the Odunaiya expression, we have shown that this leads to centered normal distribution for CVOR bearing error. A Monte-Carlo analysis has been performed in order to assess the parameter of the Rayleigh distribution. The simulation results for a test-case have been presented and analyzed. The convergence of the Monte-Carlo analysis has been checked. The distributions chosen for the multipath parameters have been verified by means of a Kolmogorov-Smirnov test. We have found that for a generic wind turbine placed approximately at 3 km from the VOR station, the standard deviation of the VOR error reaches 0.3° when the azimuth difference between the aircraft and the wind turbine are about 90° or 270° . Besides, the standard deviation is maximal for low elevation angles, *i.e.* where the mast scattering is maximal.

Conclusion

Thesis summary

The objective of this PhD thesis was to propose fast, accurate and validated tools to assess the impact of multipath on the VOR bearing error in presence of wind turbines.

In **Chapter 1**, the general context of the study has been presented. The basic principle of the CVOR and DVOR systems has been presented. The multipath phenomenon generated by wind turbines in the vicinity of VOR stations has been detailed by presenting its parameters. A state-of-the-art on modeling methods has been given. Since our work is based on the VERSO simulator, this latter has been presented in details. The classical architecture of a VOR receiver has then been exposed. This includes the main reception steps such as demodulations, filterings and phase detection to estimate the azimuth information. To calculate the VOR error, the analytical expressions proposed by Odunaiya and Quinet for CVOR and DVOR systems have been reminded and illustrated.

In **Chapter 2**, a digital VOR receiver model including filtering and demodulation steps for estimating the bearing error has been presented. This model can reproduce the response of a VOR receiver in a realistic way by taking into account the variations in time of multipath in the VOR error. A time series generator along a realistic aircraft trajectory which is defined by straight and circular sections has been presented. A sampling criterion has also been proposed to ensure the capture of the multipath variations in time and space. The digital VOR receiver model has been detailed. In order to analyze the effect of multipath dynamics on the VOR receiver, an illustration test has been given by comparing the receiver model response with the Odunaiya expression.

In **Chapter 3**, the difficulty of validating a digital VOR receiver model from available in-flight measurements has been presented. Thus, a solution which consists in performing two laboratory measurements in a conducted environment for CVOR signals has been proposed. During these measurements, our receiver model has been compared with a calibration receiver (Rhodes & Schwarz EVS300). The first measurement has been performed in the VHF frequency band for one canonical multipath. A parametric study has been carried out in order to assess the sensitivity of the results to the receiver model parameters. The second measurement has been performed using baseband IQ signals in a complex scenario. The measurements results have shown a good agreement between receivers. Thus, we can be confident on the structure and the parameters of our digital VOR receiver model.

In **Chapter 4**, an analysis of the bearing error from our digital VOR receiver model has been presented. The receiver group delay has been evaluated according to the filtering parameters. A method to determine the validity domain of the Odunaiya expression for computing the CVOR multipath error has been presented. The expression is no longer valid when the multipath is strongly attenuated by the receiver filter. This happens when its relative Doppler shift is large enough with respect to the filter bandwidths. A geometric criterion that defines this domain has been given and illustrated. We have shown that the DVOR error is sensitive to the type of FM demodulator. We have developed and validated an alternative expression called I2Q-FM error consistent with a quadrature FM demodulator. We have evaluated the multipath effect on the reference signal for DVOR. As stated by the Bredemeyer's analysis, we have shown that this effect can impact significantly the bearing error. Nevertheless, this should be confirmed with other scenarios and with a receiver using other types of components.

In **Chapter 5**, a statistical model for the CVOR multipath error has been presented. This model provides the statistical distribution of the bearing error for fixed distances VOR-aircraft and VOR-wind turbine. The other parameters (wind turbine size, materials, ground composition, etc.) follow statistical distributions. Our model is based on a Monte-Carlo analysis. This approach is a first step to develop a complete statistical model in order to quantify the VOR error from few parameters without running VERSO simulations. The configuration and the statistical distributions of the input parameters have been defined. Then, we have determined the statistical distributions of the multipath parameters and CVOR error. We have found that for a wind turbine of approximately known position and at a given observation point, the multipath is characterized by a uniform relative phase, a constant relative azimuth and a Rayleigh relative amplitude. From the Odunaiya expression, we have shown that this leads to a centered normal distribution for the CVOR bearing error. A Monte-Carlo analysis has been performed in order to assess the parameter of the Rayleigh distribution. Simulation results for a test-case have been presented and analyzed. The convergence of the Monte-Carlo analysis has been checked. Besides, the distributions chosen for the multipath parameters have been verified from Kolmogorov-Smirnov tests. We have found that for a generic wind turbine placed approximately at 3 km from the VOR station, the standard deviation of the VOR error reaches 0.3° when the azimuth difference between the aircraft and the wind turbine are about 90° or 270° . Besides, the standard deviation is maximal for low elevation angles, *i.e.* where the mast scattering is maximal.

Recommendations for future works

We here propose recommendations for future works. They are organized according to the thesis outline.

In the simulator, the relief is only taken into account between the VOR and the wind turbine. It would be valuable to take it into consideration between the VOR and the aircraft and between the wind turbine and the aircraft by applying the parabolic equation method. However, this can make the computation time very long for great distances between the

VOR antenna, the wind turbines and the aircraft. In addition, the consideration of the atmospheric refraction in all steps of the electromagnetic computation would be useful.

Secondly, the response of our digital VOR receiver model has been analyzed for CVOR signals by means of laboratory measurements in a conducted environment with a Rhodes & Schwarz EVS300. It could be useful to perform comparisons with other types of receivers such as avionic navigation receivers. Furthermore, a similar study could be performed for DVOR signals.

Thirdly, the models proposed in this PhD could be further validated by means of specific measurement campaigns. This may be performed by considering a configuration for which the wind turbine multipath error is strong. These measurements could imply a mobile VOR station, and a drone as performed in [7].

Fourthly, we have shown that the DVOR error is sensitive to the type of FM demodulator. We could assess this effect with another FM demodulation solution such as a PLL (Phase Locked Loop). We could also define the validity domain of the static analytical expressions for computing the DVOR multipath error.

Next, our statistical model of the bearing error has been applied in a test-case for fixed distances between the VOR and the wind turbine, and between the wind turbine and the aircraft. To obtain a complete statistical model, this simulation should be run again with other distances. This would allow to interpolate the CVOR error and limit the calculations to be performed for a given configuration. Furthermore, in order to improve the accuracy of the statistical model, the terrain relief could be included. Finally, a similar work for DVOR should be performed.

Finally, it would be interesting to perform the same analyses for other types of navigation systems such as ILS (Instrument Landing System), DME (Distance measuring equipment), TACAN (TACTical Air Navigation), etc. Furthermore, a complete tool based on our study could be developed in order to operationally assist the French Civil Aviation Authority (DGAC) in making decisions on the viability of wind farm projects around their communication, navigation and surveillance (CNS) ground systems.

Appendix A

Demonstration of the Odunaiya expressions

This appendix is related to the demonstration of the expressions of Odunaiya errors defined in Section 1.5.

A.1 CVOR error

In order to simplify the calculations, the amplitude of multipath is normalized by the one of direct signal. Thus, we set $a_0 = 1$, $\theta_0 = 0$ and $\varphi_0 = 0$. In Section A.1.1, we consider the particular case for which there is only one multipath. A generalized formulation is then given for N multipath in Section A.1.2.

A.1.1 Single multipath

The total VAR signal received by the receiver antenna is expressed as

$$U_{\text{var}}^{\text{tot}}(t) = \cos(2\pi f_c t)[1 + m_a \cos(2\pi f_{LF} t)] + a_1 \cos(2\pi f_c t + \theta_1)[1 + m_a \cos(2\pi f_{LF} t - \varphi_1)]. \quad (\text{A.1})$$

In the first step, an AM demodulation is applied. Therefore, the received signal is multiplied by the carrier $\cos(2\pi f_c t)$

$$\begin{aligned} U_{\text{var}}^1(t) &= \cos^2(2\pi f_c t)[1 + m_a \cos(2\pi f_{LF} t)] + \\ &\quad a_1 \cos(2\pi f_c t) \cos(2\pi f_c t + \theta_1)[1 + m_a \cos(2\pi f_{LF} t - \varphi_1)] \\ &= \frac{1}{2}(1 + \cos(4\pi f_c t))[1 + m_a \cos(2\pi f_{LF} t)] + \\ &\quad \frac{a_1}{2}(\cos(\theta_1) + \cos(4\pi f_c t + \theta_1))[1 + m_a \cos(2\pi f_{LF} t - \varphi_1)]. \end{aligned} \quad (\text{A.2})$$

In order to extract the LF information, a band-pass filter is applied. The resulting signal has the following expression

$$U_{\text{var}}^2(t) = \frac{1}{2}m_a \cos(2\pi f_{LF}t) + \frac{a_1}{2}m_a \cos(\theta_1) \cos(2\pi f_{LF}t - \varphi_1). \quad (\text{A.3})$$

This signal corresponds to the sum of 2 signals centered at the same frequency. Thus, it can be expressed as

$$U_{\text{var}}^2(t) = R \cos(2\pi f_{LF}t + \tilde{\varphi}_v^C), \quad (\text{A.4})$$

where R is the envelope, which is given by

$$R = \sqrt{\left(\frac{1}{2}m_a + \frac{a_1}{2}m_a \cos(\theta_1) \cos(\varphi_1)\right)^2 + \left(\frac{a_1}{2}m_a \cos(\theta_1)\right)^2 \sin^2(\varphi_1)}, \quad (\text{A.5})$$

and $\tilde{\varphi}_v^C$ is the LF modulated azimuth, which is defined by

$$\tilde{\varphi}_v^C = \tan^{-1} \left(\frac{a_1 \cos(\theta_1) \sin(\varphi_1)}{1 + a_1 \cos(\theta_1) \cos(\varphi_1)} \right). \quad (\text{A.6})$$

The CVOR error is expressed as the difference between the measured azimuth and the direct azimuth information. Removing the normalization, $a_0 = 1$, $\theta_0 = 0$ and $\varphi_0 = 0$, we obtain

$$\varepsilon^{C,1} = \tilde{\varphi}_v^C - \varphi_0 = \tan^{-1} \left(\frac{\frac{a_1}{a_0} \cos(\theta_1 - \theta_0) \sin(\varphi_1 - \varphi_0)}{1 + \frac{a_1}{a_0} \cos(\theta_1 - \theta_0) \cos(\varphi_1 - \varphi_0)} \right). \quad (\text{A.7})$$

A.1.2 N multipath

The expression (A.7) can be generalized for N multipath, so that

$$\varepsilon^{C,N} = \tan^{-1} \left(\frac{\sum_{n=1}^N \frac{a_n}{a_0} \cos(\theta_n - \theta_0) \sin(\varphi_n - \varphi_0)}{1 + \sum_{n=1}^N \frac{a_n}{a_0} \cos(\theta_n - \theta_0) \cos(\varphi_n - \varphi_0)} \right). \quad (\text{A.8})$$

A.2 DVOR error

In order to simplify the calculations, the amplitude of multipath is normalized by the one of direct signal. Thus, we set $a_0 = 1$, $\theta_0 = 0$ and $\varphi_0 = 0$. In Section A.2.1, we consider the particular case for which there is only one multipath. A generalized formulation is then given for N multipath in Section A.2.2.

A.2.1 Single multipath

The total VAR signal received by the receiver antenna is expressed as

$$U_{\text{var}}^{\text{tot}}(t) = \cos(2\pi f_c t) [1 + m_a \cos(2\pi f_{sc} t + m_f \cos(2\pi f_{LF} t))] + a_1 \cos(2\pi f_c t + \theta_1) [1 + m_a \cos(2\pi f_{sc} t + m_f \cos(2\pi f_{LF} t - \varphi_1))]. \quad (\text{A.9})$$

In the first step, an AM demodulation is applied. Therefore, the received signal is multiplied by the carrier $\cos(2\pi f_c t)$ and filtered to extract the sub-carrier frequency f_{sc}

$$U_{\text{var}}^1(t) = m_a \cos(2\pi f_{sc} t + m_f \cos(2\pi f_{LF} t)) + a_1 m_a \cos(\theta_1) \cos(2\pi f_{sc} t + m_f \cos(2\pi f_{LF} t - \varphi_1)). \quad (\text{A.10})$$

The signal is normalized by m_a and the following notations are considered:

- $A_1 = a_1 \cos(\theta_1)$,
- $\phi_{sc}^0 = m_f \cos(2\pi f_{LF} t)$,
- $\phi_{sc}^1 = m_f \cos(2\pi f_{LF} t - \varphi_1)$.

Thus, the signal $U_{\text{var}}^1(t)$ is expressed as

$$U_{\text{var}}^1(t) = \cos(2\pi f_{sc} t + \phi_{sc}^0) + A_1 \cos(2\pi f_{sc} t + \phi_{sc}^1). \quad (\text{A.11})$$

The signal corresponds to the sum of 2 signals of the same frequency modulated in frequency. This can be rewritten as

$$U_{\text{var}}^1(t) = R \cos(2\pi f_{sc} t + \tilde{\phi}_{LF}). \quad (\text{A.12})$$

The signal envelope is defined by

$$R = \sqrt{1 + A_1^2 + 2A_1 \cos(\phi_{sc}^1 - \phi_{sc}^0)}. \quad (\text{A.13})$$

The LF phase modulated of the signal is given by

$$\tilde{\phi}_{LF} = \phi_{sc}^0 + \tan^{-1} \left(\frac{A_1 \sin(\phi_{sc}^1 - \phi_{sc}^0)}{1 + A_1 \cos(\phi_{sc}^1 - \phi_{sc}^0)} \right). \quad (\text{A.14})$$

Noted that an ideal FM demodulator is considered in this demonstration. We assume that it will perfectly recover the phase $\tilde{\phi}_{LF}$. In the case of weak multipath, the arctangent can be assimilated to its angle, so that

$$\tilde{\phi}_{LF} = \phi_{sc}^0 + A_1 \sin(\phi_{sc}^1 - \phi_{sc}^0). \quad (\text{A.15})$$

The term $\phi_{sc}^1 - \phi_{sc}^0$ is expressed as

$$\begin{aligned}\phi_{sc}^1 - \phi_{sc}^0 &= m_f \cos(2\pi f_{LF}t - \varphi_1) - m_f \cos(2\pi f_{LF}t) \\ &= -2m_f \sin\left(\frac{2\pi f_{LF}t - \varphi_1 + 2\pi f_{LF}t}{2}\right) \sin\left(\frac{2\pi f_{LF}t - \varphi_1 - 2\pi f_{LF}t}{2}\right) \\ &= 2m_f \sin\left(\frac{4\pi f_{LF}t - \varphi_1}{2}\right) \sin\left(\frac{\varphi_1}{2}\right).\end{aligned}\quad (\text{A.16})$$

Using the properties of Bessel's functions, we can write the term $\sin(\phi_{sc}^1 - \phi_{sc}^0)$ in the following form

$$\sin(\phi_{sc}^1 - \phi_{sc}^0) = 2 \sum_{p=1}^{\infty} J_{2p-1}\left(2m_f \sin\left(\frac{\varphi_1}{2}\right)\right) \sin\left((2p-1)\frac{4\pi f_{LF}t - \varphi_1}{2}\right). \quad (\text{A.17})$$

The phase is determined with an ideal FM demodulator where the high frequencies are filtered, only the first term of this series is considered. Thus, the FM discriminator output becomes

$$\begin{aligned}\tilde{\phi}_{LF} &= m_f \cos(2\pi f_{LF}t) + 2A_1 J_1\left(2m_f \sin\left(\frac{\varphi_1}{2}\right)\right) \sin\left(2\pi f_{LF}t - \frac{\varphi_1}{2}\right) \\ &= m_f \cos(2\pi f_{LF}t) + 2A_1 J_1\left(2m_f \sin\left(\frac{\varphi_1}{2}\right)\right) \cos\left(\frac{\pi}{2} - 2\pi f_{LF}t + \frac{\varphi_1}{2}\right).\end{aligned}\quad (\text{A.18})$$

The signal corresponds to the sum of 2 signals of the same frequency modulated in frequency. This can be rewritten

$$\tilde{\phi}_{LF} = Q \cos(2\pi f_{LF}t + \tilde{\varphi}^D), \quad (\text{A.19})$$

Q represents the signal envelope. $\tilde{\varphi}^D$ corresponds to the estimated azimuth in presence of one multipath for a DVOR. Its value is given by

$$\tilde{\varphi}^D = \tan^{-1}\left(\frac{2A_1 J_1\left(-2m_f \sin\left(\frac{-\varphi_1}{2}\right)\right) \sin\left(\frac{\pi}{2} - \frac{\varphi_1}{2}\right)}{m_f + 2A_1 J_1\left(-2m_f \sin\left(\frac{-\varphi_1}{2}\right)\right) \cos\left(\frac{\pi}{2} - \frac{-\varphi_1}{2}\right)}\right). \quad (\text{A.20})$$

The DVOR error is expressed as the difference between the measured azimuth and the direct azimuth information. Removing the normalization, $a_0 = 1$, $\theta_0 = 0$ and $\varphi_0 = 0$, we obtain

$$\varepsilon^{\text{D},1} = \tilde{\varphi}^D - \varphi_0 = \tan^{-1}\left(\frac{2A_1 J_1\left(2m_f \sin\left(\frac{\varphi_1}{2}\right)\right) \cos\left(\frac{\varphi_1}{2}\right)}{m_f + 2A_1 J_1\left(2m_f \sin\left(\frac{\varphi_1}{2}\right)\right) \sin\left(\frac{\varphi_1}{2}\right)}\right). \quad (\text{A.21})$$

A.2.2 N multipath

The expression (A.21) can be generalized for N multipath, so that

$$\varepsilon^{\text{D},N} = \tan^{-1} \left(\frac{2 \sum_{n=1}^N \frac{a_n}{a_0} \cos(\theta_n - \theta_0) J_1 \left(2m_f \sin \left(\frac{\varphi_n - \varphi_0}{2} \right) \right) \cos \left(\frac{\varphi_n - \varphi_0}{2} \right)}{m_f + 2 \sum_{n=1}^N \frac{a_n}{a_0} \cos(\theta_n - \theta_0) J_1 \left(2m_f \sin \left(\frac{\varphi_n - \varphi_0}{2} \right) \right) \sin \left(\frac{\varphi_n - \varphi_0}{2} \right)} \right). \quad (\text{A.22})$$

Appendix B

Taylor series analysis of the Quadrature FM demodulator

This appendix is related to a more detailed analysis of the FM quadrature demodulator given in Section 2.3.3.c via Taylor series.

We consider the FM REF signal for CVOR expressed by (2.18). The first demodulation step consists in introducing a replica of the REF signal with a quadrature delay τ_q . The second operation is to multiply the reference signal with its delayed replica. This yields (2.20). The term around the frequency $2f_{sc}$ is then eliminated by band-pass filtering. Thus, after filtering we have (2.21). τ_q is taken small compared to the 30 Hz signal period constituting $\phi_{LF}(t)$. Therefore, we can perform the following simplifications

$$\begin{aligned}\cos(\delta\phi_{LF}) &\simeq 1 + O(\delta\phi_{LF}) \\ \sin(\delta\phi_{LF}) &\simeq \delta\phi_{LF} + O((\delta\phi_{LF})^2) \\ \frac{\delta\phi_{LF}}{\tau_q} &\simeq \dot{\phi}_{LF} \left(t - \frac{\tau_q}{2} \right) + O(\tau_q^2),\end{aligned}\tag{B.1}$$

where $\delta\phi_{LF} = \phi_{LF}(t) - \phi_{LF}(t - \tau_q)$. If the quadrature phase shift error ε is small enough in (2.19), we can write

$$\begin{aligned}\cos(2\pi f_{sc}\tau_q) &= -\sin(\varepsilon) \simeq -\varepsilon + O(\varepsilon) \\ \sin(2\pi f_{sc}\tau_q) &= \cos(\varepsilon) \simeq 1 + O(\varepsilon).\end{aligned}\tag{B.2}$$

We include these simplifications (B.1) and (B.2) in (2.21). The signal at the output of the FM demodulator is expressed as

$$p(t) = \frac{-A_0(t)A_0(t - \tau_q)}{2} \left[\varepsilon + \tau_q \dot{\phi}_{LF} \left(t - \frac{\tau_q}{2} \right) + O(\varepsilon) + O(\tau_q^2) + O(\delta\phi_{LF}) \right].\tag{B.3}$$

Appendix C

Statistics of the wind turbine characteristics

This appendix is related to the numerical values of statistical parameters proposed in Section 5.5.1.b.

The characteristics of the wind turbine follow statistical distributions. The characteristics of the distributions associated with the mast and the blade lengths are defined from a database of 2000 wind turbines installed in the North of France. This database comes from geo.data.gouv.fr, a french institutional website [55]. The distributions of the other parameters are characterized according to available data from wind turbine manufacturers.

- **Parameters of mast**

The mast is modeled by a metallic conical section and characterized by its height H , its ground diameter D_1 and its top diameter D_2 . In Figure C.1, we display the observation frequency of the mast height distribution extracted from the database. We assume that this parameter follows a normal distribution characterized by a mean of 95 m and a standard deviation of 21 m.

The characteristics of the diameters D_1 and D_2 are not available in the database. We then consider that these diameters follow an uniform distribution. In Table C.1, we show examples of mast diameters for different types of wind turbines [56, 57].

Type	Ground diameter D_1 (m)	Top diameter D_2 (m)
ENERCON E-92	4.9	2.2
ENERCON E-82	4	2.1
VESTAS V112	3.9	3.2

Table C.1: Examples of mast diameters for different types of wind turbines.

According to [58], the ground diameter of mast must not exceed 5 m in order to facilitate the transportation. Therefore, the parameters of the uniform distribution

associated with these diameters are set in Monte Carlo simulations with respect to this construction criterion and the data given in Table C.1.

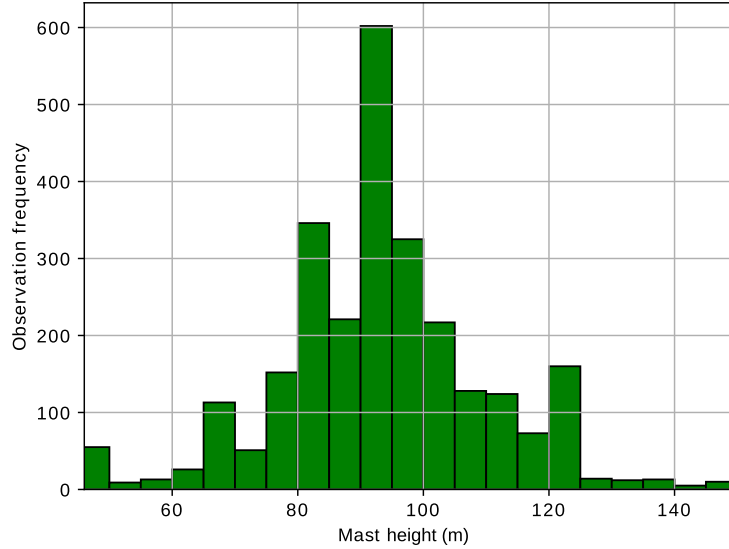


Figure C.1: Observation frequency of the mast height in the database.

- **Nacelle parameters**

The nacelle is modeled by a metallic rectangular box of size $h_1 \times h_2 \times h_3$. The characteristics of these parameters are not available in the database. We then consider that they follow a uniform distribution. In Table C.2, we show examples of nacelle dimensions for different types of wind turbines [56, 57].

Type	Length h_1 (m)	Height h_2 (m)	Width h_3 (m)
ENERCON E-70	11	4	4
VESTAS V112	12.8	4	3.4
VESTAS V136	14	4.2	4.2

Table C.2: Examples of nacelle dimensions for different types of wind turbines.

- **Blade parameters**

In Figure C.2, we display the observation frequency of the length ratio blade/mast distribution extracted from the database. We assume that this parameter follows a normal distribution characterized by a mean of 0.6 and a standard deviation of 0.1. The other blade dimensions are fixed by deterministic ratios with respect to the total length L_2 .

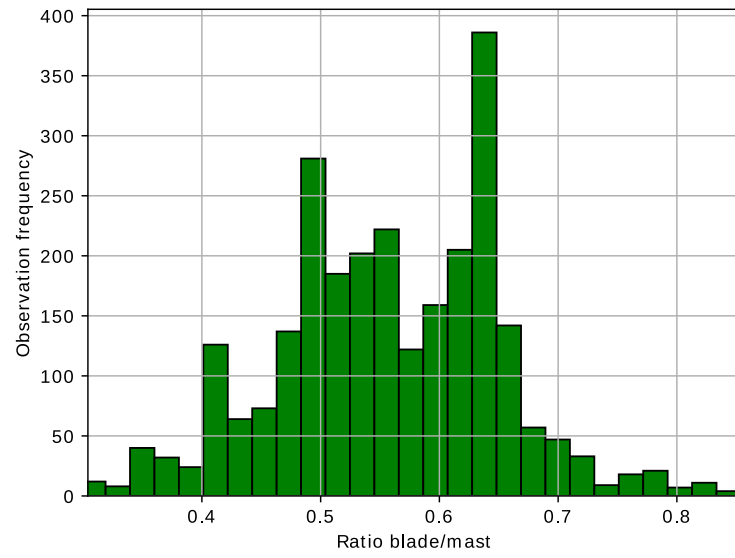


Figure C.2: Observation frequency of the ratio blade length over mast length in the database.

Appendix D

Summary in French (Résumé français)

D.1 Introduction

L'implémentation des éoliennes à proximité des systèmes VOR (VHF Omnidirectional Range) est une préoccupation importante pour l'aviation civile. Les éoliennes constituent une source de multitrajets qui peuvent produire des erreurs sur l'information d'azimut estimée par le récepteur d'avion. Dans la littérature, l'erreur VOR est calculée à partir de paramètres multitrajets en utilisant l'expression analytique proposée par Odunaiya et Quinet. L'objectif principal de cette thèse de doctorat consiste à fournir un ou plusieurs outils de simulation rapides, précis et validés afin d'évaluer l'impact des multitrajets sur l'erreur VOR en présence d'éoliennes. Les principales tâches à accomplir dans le cadre de ce travail de thèse sont les suivantes :

- Développement d'un modèle de récepteur VOR numérique qui peut reproduire la réponse d'un récepteur VOR de manière réaliste.
- Évaluation de l'impact des variations de multitrajets avec le temps au long d'une trajectoire d'avion réaliste sur un récepteur VOR réel en analysant l'erreur angulaire à partir du modèle numérique.
- Détermination de la validité du modèle de récepteur VOR numérique et des expressions statiques d'Odunaiya à partir de simulations, d'analyses physiques et de mesures en laboratoire.
- Développement d'un modèle alternatif fournissant la distribution statistique de l'erreur VOR à partir de quelques paramètres.

D.2 Modèle de récepteur VOR numérique

D.2.1 Introduction

Dans ce chapitre, nous présentons un modèle de récepteur VOR numérique qui peut reproduire la réponse d'un récepteur VOR sur une trajectoire d'avion réaliste en présence de multitrajets variant avec le temps.

D.2.2 Séries temporelles de paramètres multitrajets

Pour obtenir les séries temporelles, une trajectoire réaliste de l'avion est échantillonnée avec un pas temporel suffisamment court pour modéliser avec précision les variations du signal dans l'espace. La trajectoire est une série d'éléments rectilignes ou circulaires. Selon le critère de Nyquist, le pas spatial doit être inférieur à une demi-longueur d'onde

$$\Delta x < \frac{\lambda}{2}. \quad (\text{D.1})$$

le pas temporel est exprimé en termes de pas spatial et de vitesse maximale au long de la trajectoire

$$\Delta t_{\min} = \frac{\Delta x}{V_{\max}}. \quad (\text{D.2})$$

À chaque point de la trajectoire, nous utilisons la méthode d'hybridation de l'équation parabolique avec l'optique physique pour calculer les paramètres multitrajets. Ces caractéristiques seront envoyées à un récepteur VOR numérique pour évaluer l'influence des variations multitrajets avec le temps sur l'erreur angulaire.

D.2.3 Présentation du modèle de récepteur

Nous proposons ici un modèle de récepteur VOR numérique pour reproduire la réponse dynamique d'un récepteur VOR réaliste, en tenant compte des démodulations et du filtrage. Dans cette section, la structure du modèle proposé est présentée.

Le diagramme en bloc de notre modèle de récepteur VOR numérique pour traiter le signal VORC (VOR Conventionnel) est donné dans la Figure D.1. Il convient de noter que le modèle de récepteur peut également traiter les signaux du VORD (VOR Doppler).

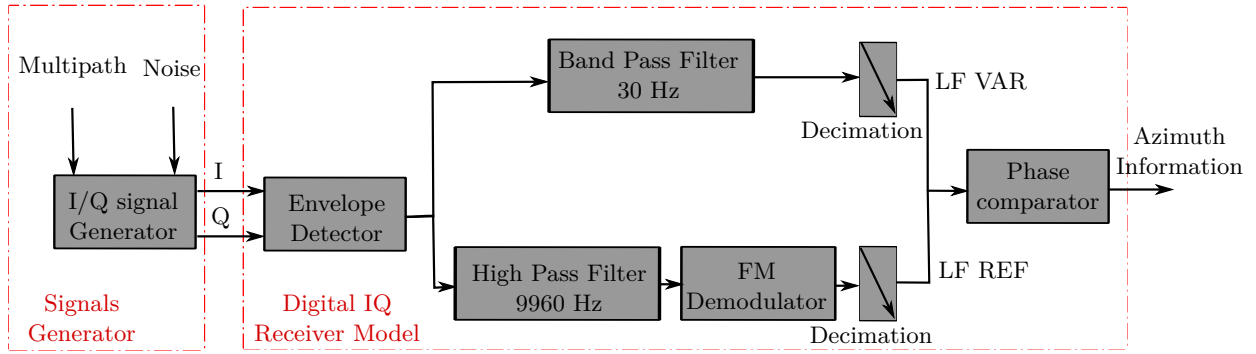


Figure D.1: Diagramme en bloc du modèle de récepteur VOR numérique pour traiter le signal VORC (pour le signal VORD, les canaux REF et VAR sont inversés).

D.2.3.a Générateur de signaux I/Q

Notre modèle est basé sur un générateur de signaux I/Q à partir des paramètres des multitrajets calculés par le simulateur VERSO (VOR ERror SimulatOr). Nous avons besoin dans le récepteur d'une fréquence d'échantillonnage d'au moins $2(f_{sc} + f_{LF}m_f) = 20880$ Hz pour respecter le critère de Nyquist. Un sur-échantillonnage doit donc être effectué sur les paramètres des multitrajets. Ceci est fait en utilisant une interpolation linéaire. Afin de modéliser le bruit détecté à l'entrée du modèle de récepteur, un bruit blanc gaussien additif est ajouté aux signaux I/Q.

D.2.3.b Simulateur de récepteur

Lorsque les signaux I/Q sont générés, ils sont transmis à l'unité réceptrice pour extraire l'information d'azimut. Cette section décrit les étapes de démodulation et de filtrage appliquées dans le modèle de récepteur VOR numérique proposé.

D'abord, le détecteur d'enveloppe effectue une démodulation AM afin de récupérer les signaux VAR et REF. Ensuite, des filtrages dédiés sont appliqués à l'enveloppe complexe afin d'extraire séparément ces signaux. Pour le VORC, un filtre passe-bande est utilisé pour extraire le signal variable à 30 Hz et un filtre passe-haut est appliqué pour obtenir le signal de référence à 9960 Hz. Puis, nous proposons le discriminateur à déphasage afin d'extraire le signal REF à 30 Hz. À la sortie des canaux REF et VAR, seuls les signaux LF (30 Hz) doivent rester. Ainsi, une opération de décimation est appliquée afin de réduire le temps de calcul. Enfin, les données décimées sont envoyées au comparateur de phase afin d'extraire l'information d'azimut.

D.2.4 Test d'illustration

Cette section présente un test de simulation avec notre modèle de récepteur et avec l'expression d'Odunaiya pour analyser les variations des multitrajets avec le temps.

Nous considérons une station VOR fonctionnant à une fréquence de 113,8 MHz avec une puissance de 50 W. Une éolienne de type ENERCON E82 est placée à 1 km de la station VOR, ce qui devrait permettre d'obtenir un multitrajet. Pour simplifier l'analyse, une trajectoire rectiligne de 6 km est considérée ici. Tout d'abord, l'avion est immobile pendant 5 s pour assurer la fin de la période transitoire du récepteur. Ensuite, il démarre à basse vitesse jusqu'à ce qu'il atteigne le second point de trajectoire à 180 km/h. La configuration est illustrée sur la Figure D.2.

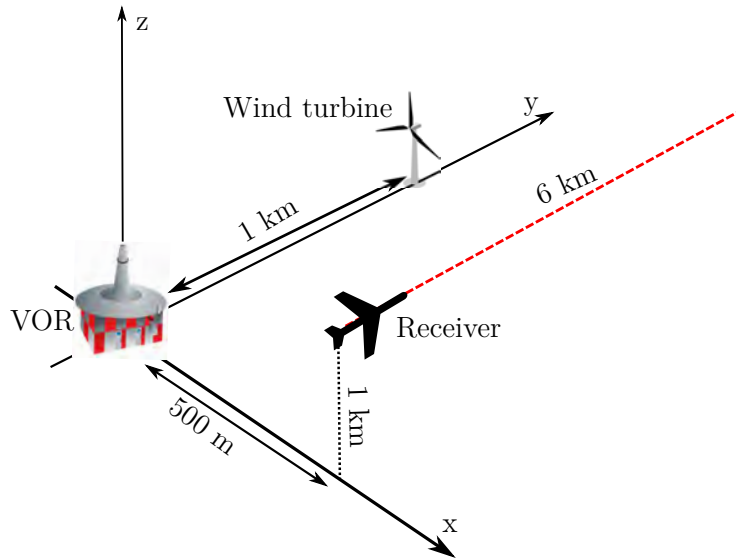


Figure D.2: Configuration proposée pour le test d'illustration.

Les paramètres des multitrajets sont interpolés à une fréquence de 25 kHz dans le générateur de signaux I/Q. Pour se concentrer sur l'effet de multitrajets, aucun bruit supplémentaire n'est pris en compte. Les paramètres de filtrage de notre modèle de récepteur I/Q numérique sont indiqués dans Table D.1.

Dans Figure D.3, l'azimut du multitrajet est tracé par rapport au temps. La couleur indique la puissance du multitrajet par rapport au trajet direct. On observe qu'il existe un seul multitrajet. Il est puissant pendant la première partie de la trajectoire de 0 s à 50 s et significative à la fin de 200 s à 250 s. Ceci est dû au fait que l'avion se trouve dans la zone de réflexion spéculaire de l'éolienne.

Dans les Figures D.4a et D.4b, nous affichons les erreurs VOR obtenues avec l'expression d'Odunaiya et avec le modèle de récepteur VOR. Pendant les 2 premières secondes, la réponse du récepteur change rapidement. Cela est dû à la phase transitoire des filtres. La réponse du récepteur converge vers le modèle d'Odunaiya pendant 5 s lorsqu'aucun effet dynamique n'est impliqué.

L'avion se déplace lentement et la réponse du récepteur reste proche du modèle statique d'Odunaiya. Pendant cette phase, il y a un retard entre les deux modèles qui est dû à la réponse du filtrage. Lorsque l'avion accélère, Les deux modèles ne donnent pas la même réponse à partir de 25 s. Cela est dû à la variation rapide du multitrajet. Lorsque l'avion s'éloigne du VOR et de l'éolienne, la différence de phase entre le trajet direct et le

multitrajet varie lentement, ce qui explique les fluctuations lentes de l'erreur VOR. D'où, le modèle statique converge à nouveau vers le modèle dynamique malgré la vitesse élevée de l'avion.

Input parameters					
	Type	F_{pass} (Hz)	F_{stop} (Hz)	R_{pass} (dB)	R_{stop} (dB)
Band-pass filter 30 Hz	IIR Butterworth	[29,31]	[24,36]	0.1	30
Low-pass filter DC	IIR Butterworth	1	2	0.1	20
High-pass filter 9960 Hz	FIR Kaiser	8000	7000	N/A	60
Filter characteristics					
	Cutoff frequency (Hz)			Order	
Band-pass filter 30 Hz	31.74			9	
Low-pass filter DC	1.43			5	
High-pass filter 9960 Hz	7795.14			15	

Table D.1: Paramètres des filtres du modèle de récepteur utilisés pour le test d'illustration.

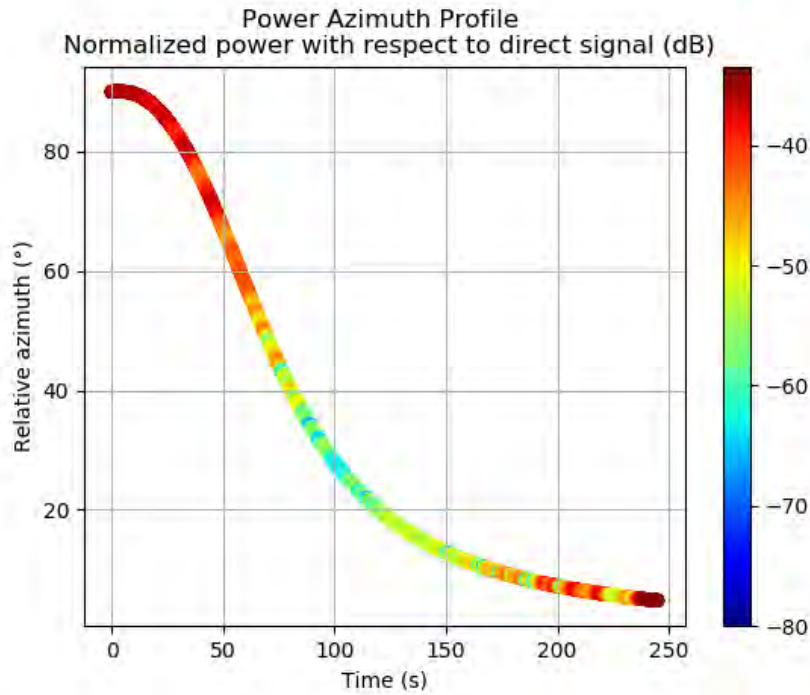
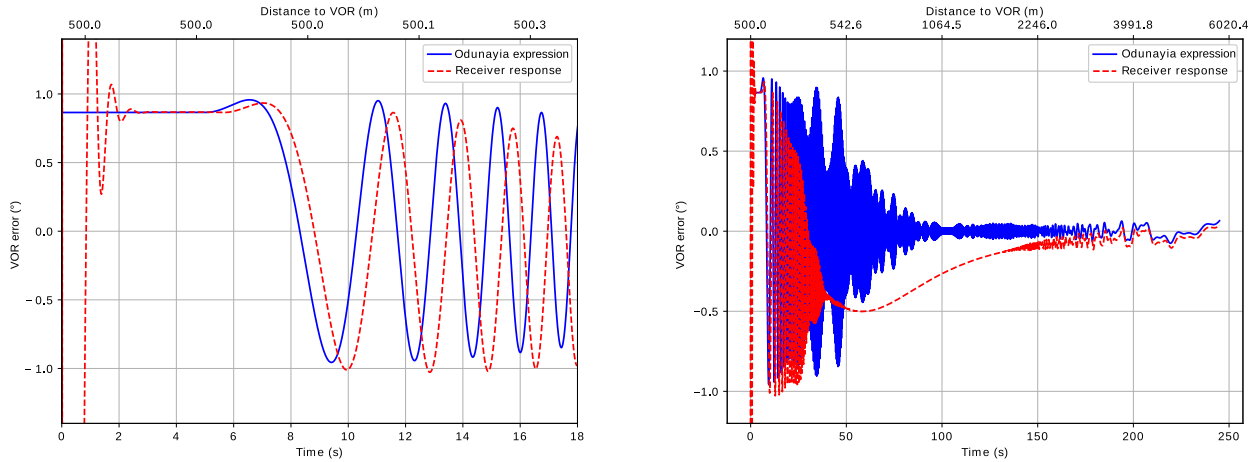


Figure D.3: Profil azimutal de puissance relative (dB) du multitrajet tout au long de la trajectoire.



(a) Réponse du récepteur entre 0 s et 18 s

(b) Réponse du récepteur entre 0 s et 250 s

Figure D.4: Réponse du récepteur au long de la trajectoire.

D.2.5 Conclusion

Dans ce chapitre, un modèle de récepteur VOR numérique permettant d'estimer l'erreur angulaire a été étudié. Le calcul des séries temporelles pour les signaux VOR en présence de multitrajets a été présenté. Ces séries temporelles ont été envoyées à un modèle de récepteur VOR numérique pour évaluer l'influence des variations des multitrajets avec le temps sur l'erreur VOR. Le modèle a été testé dans un scénario dynamique.

D.3 Analyse du multitrajet VORC à partir de mesures en laboratoire

D.3.1 Introduction

Dans ce chapitre, le comportement de notre modèle de récepteur VOR numérique est analysé en le comparant avec un récepteur de calibration (R&S EVS300) à l'aide de deux mesures de laboratoire pour des signaux VORC. La première mesure est effectuée dans la bande des fréquences VHF en traitant un multitrajet canonique. La seconde mesure est effectuée en utilisant des signaux en bande de base IQ générées à partir d'une simulation d'un scénario complexe.

D.3.2 Analyse des mesures de contrôle en vol: difficultés et limites

Nous présentons ici la difficulté de comparer les résultats de simulation avec des mesures disponibles de contrôle en vol.

Le scénario, illustré Figure D.5, est composé de 9 éoliennes ENERCON-E70 (représentées par des cercles jaunes) à proximité d'un VORC à Boulogne-sur-Mer (France) à la fréquence de 113/8 MHz. Le relief entre le VORC et les éoliennes est pris en compte et le sol est considéré humide.

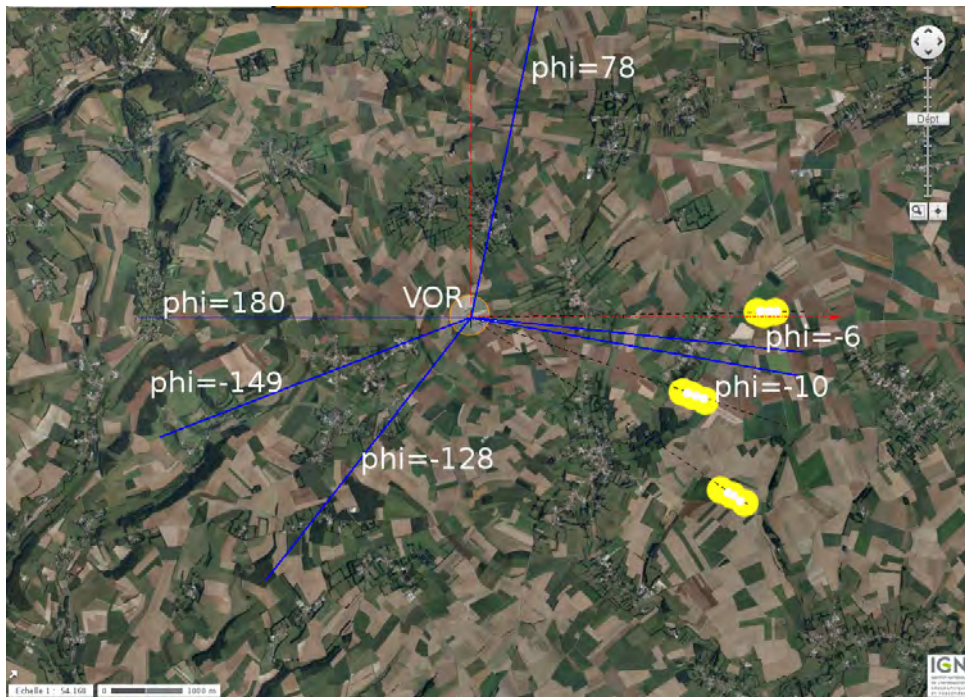


Figure D.5: Parc éolien à 5 km du VORC de Boulogne-sur-Mer.

La campagne de mesures a été réalisée sur 6 radiales et à trois moments différents correspondant à trois configurations : sans éoliennes, avec seulement les mâts et avec les éoliennes complètes. Dans le travail de thèse de Claudepierre, cette configuration a été simulée. Nous nous concentrons sur les radiales -6° et -10° .

Les erreurs VORC simulées et mesurées en présence des éoliennes sont représentées sur la Figure D.6 par rapport à la distance du VORC. On peut voir que la simulation reproduit avec succès l'enveloppe et la période d'oscillation de l'erreur mesurée. Cependant, on observe qu'il est difficile de récupérer toutes les oscillations de l'erreur mesurée pour les deux simulations.

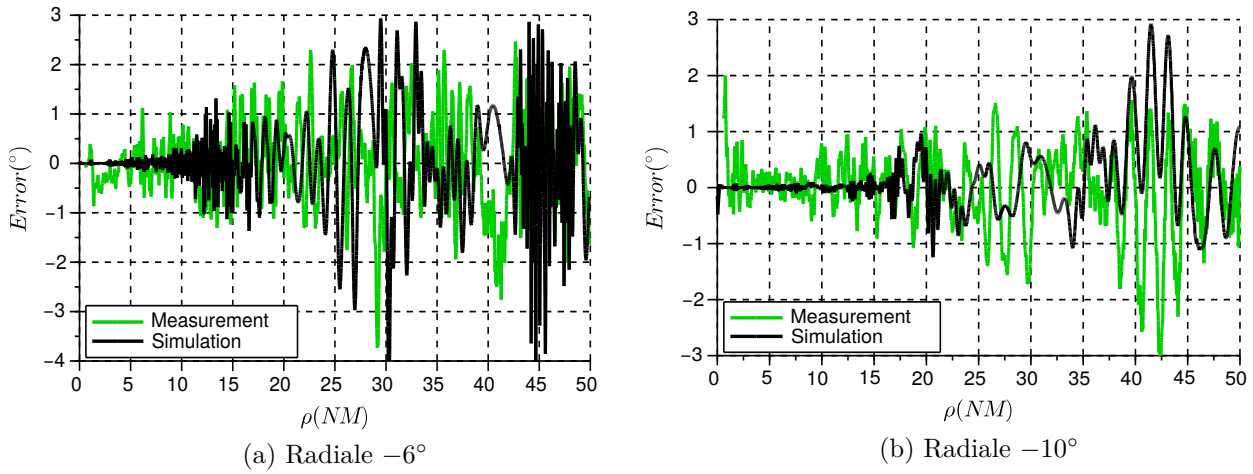


Figure D.6: Erreurs VOR simulées et mesurées en présence des éoliennes.

Les incertitudes entre la simulation et les résultats des mesures peuvent être dues au relief non pris en compte entre les éoliennes et les points d'observation. Elles sont très probablement dues aux inexactitudes dans les positions. Une légère modification de la trajectoire de l'avion ou des positions des éoliennes modifie considérablement la phase de propagation. L'erreur peut alors aussi être significativement affectée. Ceci est dû à la forte dépendance de l'erreur VOR par rapport à la phase de multitrajet.

Cela montre la difficulté de comparer les résultats des simulations avec les mesures disponibles. Ainsi, nous proposons une solution qui consiste à effectuer des mesures en laboratoire dans un environnement conduit.

D.3.3 Confrontation à partir de mesures VHF

L'objectif de cette section est de comparer le modèle de récepteur VOR numérique avec le récepteur de calibration en traitant un signal VHF pour un multitrajet canonique dans un environnement conduit.

La Figure D.7 montre la configuration de notre campagne de mesures. Un signal direct et un multitrajet canonique sont générés. La combinaison de ces signaux est envoyée à un récepteur VOR de calibration via son entrée RF et au modèle de récepteur VOR numérique via un détecteur IQ numérique pour estimer l'erreur angulaire.

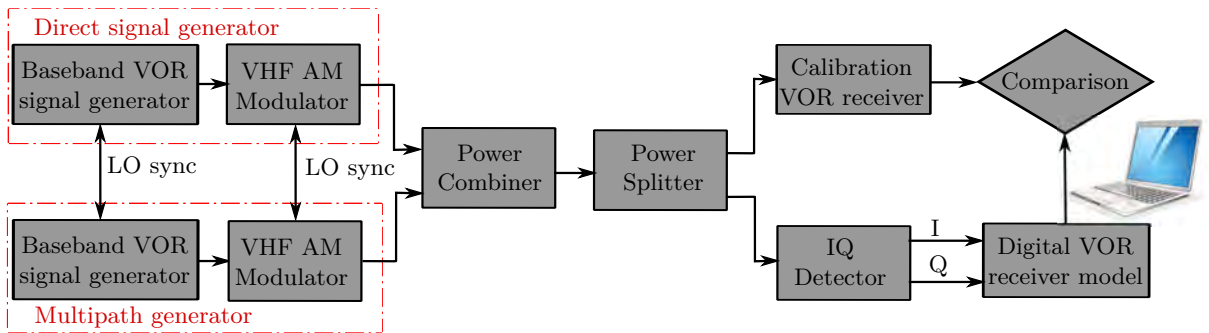
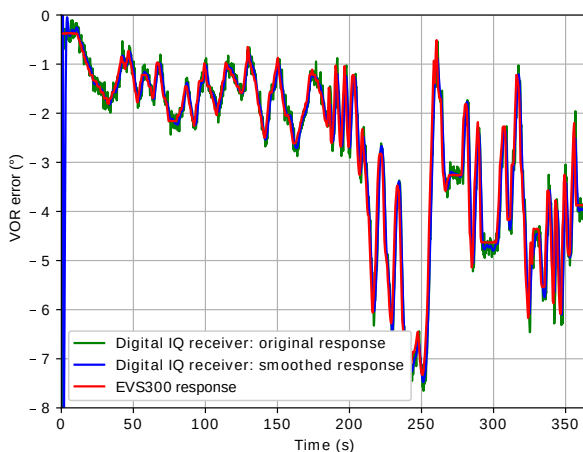


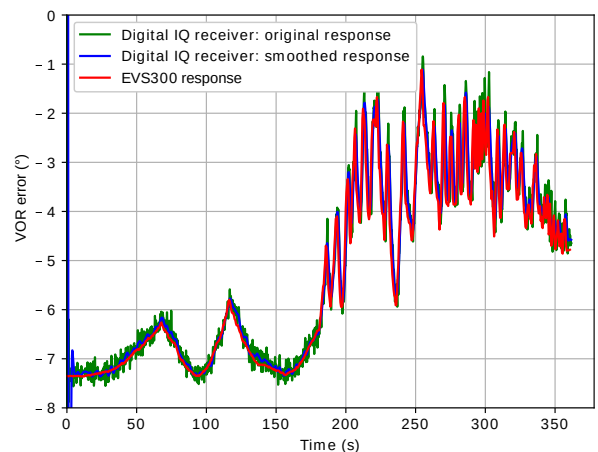
Figure D.7: Schéma bloc de la campagne de mesures VHF.

Nous considérons un VORC de fréquence 113 MHz. Nous fixons une puissance de -50 dBm pour le signal direct et de -70 dBm pour le multitrajet. L'azimut relatif du multitrajet est fixé à 90°. La phase relative du multitrajet varie aléatoirement. Dans ce test, on considère deux enregistrements de 6 min.

Les erreurs VOR calculées par le modèle de récepteur IQ numérique et le récepteur de calibration sont tracées Figures D.8a et D.8b par rapport au temps pour les deux enregistrements. Un filtrage de lissage est appliqué à la réponse de récepteur numérique. Nous observons un très bon accord entre notre modèle de récepteur et le récepteur réel, sauf pendant les premières secondes, qui correspondent à la période transitoire du modèle de récepteur. L'erreur mesurée par le récepteur EVS300 est bien évaluée par le modèle de récepteur en termes d'enveloppe et d'oscillations.



(a) Enregistrement 1



(b) Enregistrement 2

Figure D.8: Réponses des récepteurs pour les deux enregistrements.

D.3.4 Confrontation à partir des mesures IQ en bande de base

L'objectif de cette section consiste à comparer le modèle de récepteur avec le récepteur de calibration à partir des mesures IQ en bande de base pour un scénario réaliste complexe.

Le schéma bloc de la campagne de mesure IQ en bande de base est présenté dans Figure D.9.

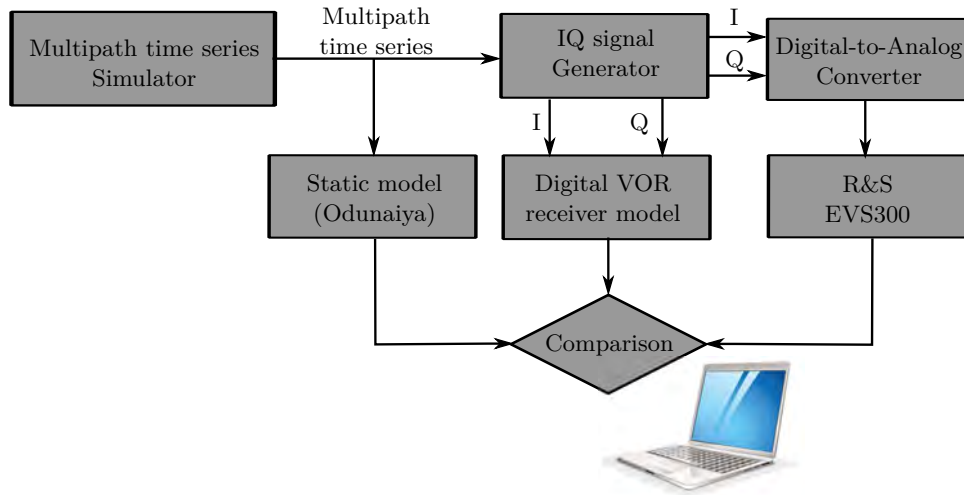


Figure D.9: Schéma bloc de la campagne de mesure IQ en bande de base.

Le signal IQ est généré dans un scénario complexe calculé avec notre simulateur de séries temporelles de multitrajets. L'erreur VOR est calculée par notre modèle de récepteur. Nous effectuons également un calcul analytique avec les expressions d'Odunaiya afin de mettre en évidence le comportement de notre modèle de récepteur dans le contexte de la variation temporelle des multitrajets. Pour estimer l'erreur VOR par le récepteur de calibration, les données IQ sont envoyées à l'EVS300 via son entrée LF au moyen d'un convertisseur numérique-analogique qui est la sortie audio d'une carte son de PC.

Nous considérons une station VORC fonctionnant à une fréquence de 113 MHz avec une puissance de 50 W. À 1 km de la station VOR, il y a une éolienne générique. L'avion se déplace sur une trajectoire rectiligne de 15 km avec un azimuth constant de 45°. L'avion est immobile pendant les 10 premières secondes pour assurer la fin de l'état transitoire du récepteur. Il démarre à faible vitesse jusqu'à la fin de la trajectoire où il atteint une vitesse de 180 km/h.

Nous montrons sur la FigureD.10 les erreurs VOR calculées par l'expression d'Odunaiya, le modèle de récepteur et le récepteur de calibration. On observe un bon accord entre le modèle de récepteur et le dispositif de calibration tout au long de trajectoire de l'avion. Lorsque le multitrajet varie rapidement au entre 10 s et 320 s, la réponse statique ne suit ni le récepteur de calibration ni le modèle du récepteur. Lorsque l'avion s'éloigne du

D.4. ANALYSE DE L'ERREUR ANGULAIRE OBTENUE À PARTIR DU MODÈLE DE RÉCEPT

VOR et de l'éolienne, les réponses du récepteur correspondent à l'expression d'Odunaiya malgré la vitesse élevée de l'avion. Ceci est dû à la lente variation de phase multitrajet.

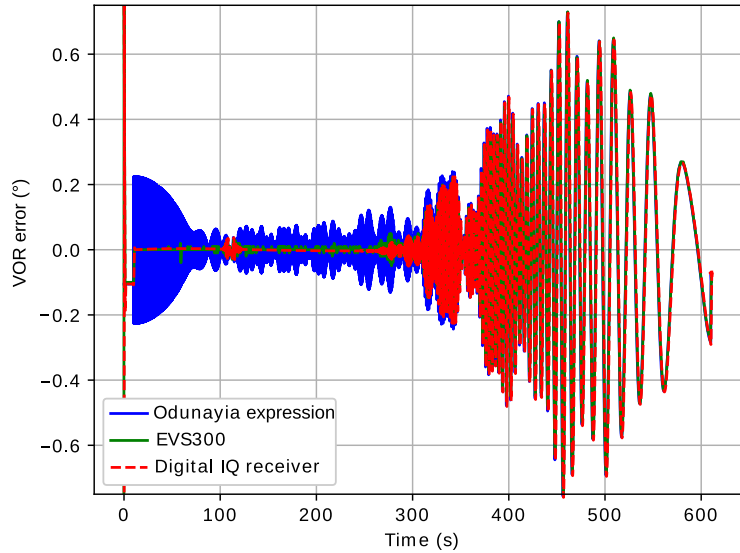


Figure D.10: Réponses des récepteurs tout au long de la trajectoire pour les mesures IQ en bande de base.

D.3.5 Conclusion

Dans ce chapitre, la difficulté d'analyser les résultats de la simulation par rapport aux mesures de contrôle en vol a été présentée. Ainsi, une solution qui consiste à effectuer deux mesures en laboratoire dans un environnement conduit pour les signaux VORC a été proposée. La première mesure a été réalisée dans la bande de fréquences VHF pour un multitrajet canonique. La seconde mesure a été réalisée en utilisant des signaux IQ en bande de base dans un scénario complexe. Les résultats des mesures ont montré un bon accord entre notre modèle et l'EVS300. Ainsi, nous pouvons être confiants sur la structure et les paramètres de notre modèle de récepteur numérique.

D.4 Analyse de l'erreur angulaire obtenue à partir du modèle de récepteur

D.4.1 Introduction

Dans ce chapitre, l'erreur VOR obtenue à partir du modèle du récepteur est analysée. Le retard de groupe récepteur est présenté. Pour le VORC, nous déterminons le domaine de validité de l'expression d'Odunaiya afin de calculer l'erreur VOR. Pour le VORD,

nous montrons que l'erreur VOR est sensible au type de démodulateur FM. Enfin, nous évaluons l'analyse de Bredemeyer qui indique que l'effet des multitrajets sur le signal de référence doit être pris en compte dans le calcul de l'erreur VORD.

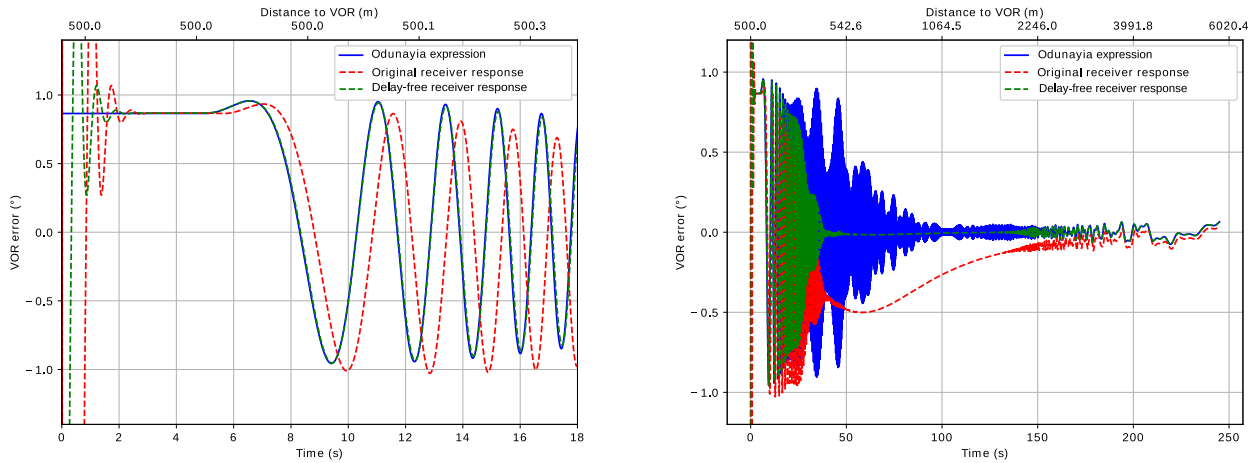
D.4.2 Retard de groupe récepteur

Nous présentons ici que le retard de groupe récepteur qui correspond principalement à la réponse de filtrage.

Nous avons montré que le retard de groupe du filtre passe-haut de 9960 Hz est négligeable par rapport aux retards des autres filtres de récepteur. Ainsi, le retard de groupe total du récepteur est donné par la somme des retards τ_g^{BPF} et τ_g^{LPF} correspondant respectivement au filtre passe-bande de 30 Hz et au filtre passe-bas DC, de sorte que

$$\tau_g^{\text{tot}} = \tau_g^{\text{BPF}} + \tau_g^{\text{LPF}}. \quad (\text{D.3})$$

Nous considérons l'exemple des résultats des tests donnés dans Section D.2.4 (voir Figure D.4). Nous illustrons Figures D.11a et D.11b les résultats de la réponse du récepteur sans et avec retard en utilisant 2 échelles de temps. Les résultats correspondent à l'expression Odunaiya lorsque les multitrajets varient lentement ($t < 30$ s et $t > 140$ s). Pour $30 < t < 140$ s, la réponse du récepteur sans retard de groupe tend vers zéro.



(a) Réponse du récepteur entre 0 s et 18 s

(b) Réponse du récepteur entre 0 s et 250 s

Figure D.11: Réponse du récepteur avec et sans retard de groupe.

D.4.3 Domaine de validité de l'expression d'Odunaiya pour le VORC

Nous présentons ici le domaine de validité de l'expression statique d'Odunaiya pour le calcul de l'erreur VORC.

En faisant une analyse spectrale des signaux intermédiaires dans le modèle de récepteur en présence d'un multitrajet canonique, nous avons montré que la sensibilité de la réponse du récepteur au multitrajet dépend de la fréquence instantanée relative de ce multitrajet et des paramètres de largeur de bande des filtres du récepteur. Nous avons observé que l'expression d'Odunaiya pour un VORC n'est plus valable lorsque le multitrajet est rejeté en dehors de la bande passante des filtres du récepteur en raison de l'effet Doppler. Dans ce cas, le multitrajet n'affecte plus l'estimation angulaire. L'expression d'Odunaiya n'est pas valable lorsque

$$f_0 \frac{v_{Rx}}{c_0} |\hat{\mathbf{r}}_{w_0} \cdot \hat{\mathbf{u}}_m| > \min \left(\frac{W_{30}}{2}, W_{DC} \right), \quad (\text{D.4})$$

où f_0 est la fréquence de la source, v_{Rx} est la vitesse du récepteur, c_0 est la vitesse de la lumière. W_{30} et W_{DC} sont les largeurs de bande à 3 dB du filtre bande-passante 30 Hz et filtre passe-bas DC, respectivement. \mathbf{r}_{w_0} et \mathbf{u}_m sont illustrés dans Figure D.12.

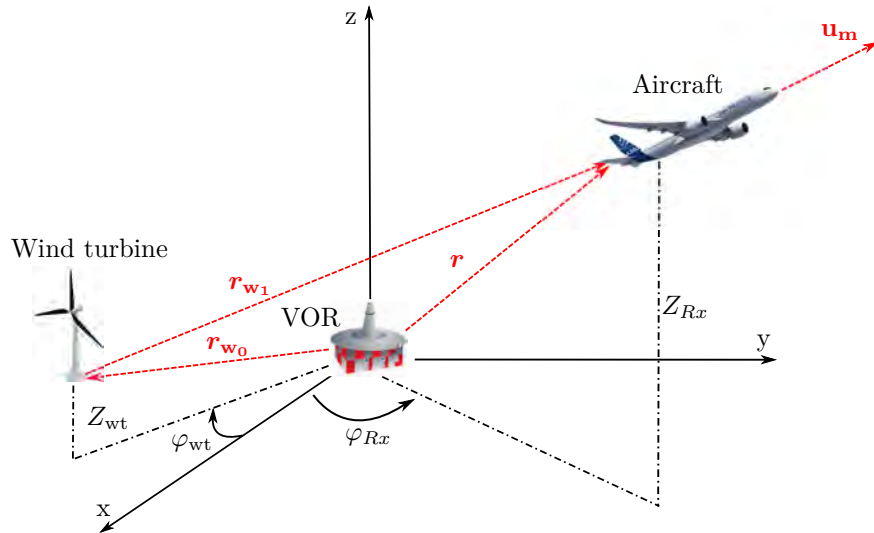


Figure D.12: Configuration de la trajectoire de l'avion.

D.4.4 Erreur analytique du multitrajet VORD

Nous présentons ici l'expression de l'erreur analytique du multitrajet VORD, appelée erreur I2Q-FM, qui est cohérente avec notre démodulateur en quadrature FM.

L'expression analytique de l'erreur I2Q-FM est donnée par

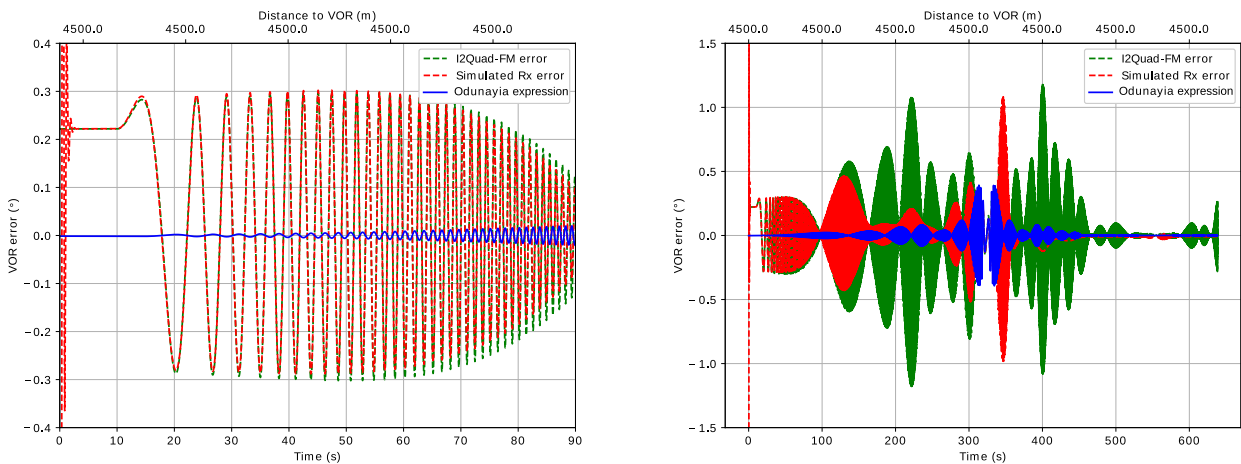
$$\varepsilon^{D,N} = 2 \sum_{n=1}^N \frac{a_n}{a_0} \cos(\theta_n - \theta_0) J_1' \left(-2m_f \sin \left(\frac{\varphi_n - \varphi_0}{2} \right) \right) \sin(\varphi_n - \varphi_0). \quad (\text{D.5})$$

Cette expression est développée en appliquant certaines hypothèses qui sont :

- Les multitrajets sont faibles
- Le retard qui assure le déphasage en quadrature dans le démodulateur FM est pris faible par rapport à la période du signal 30 Hz
- L'erreur de déphasage en quadrature est négligeable dans le démodulateur FM
- Le filtrage passe-haut est considéré idéal
- Absence de bruit

L'erreur I2Q-FM donnée par (D.5) est validée par des comparaisons avec les résultats du modèle du récepteur dans un scénario réaliste complexe.

Nous considérons la configuration proposée dans Section D.2.4, sauf que nous considérons une station VORD. Dans les Figures D.13a et D.13b, les erreurs obtenues par l'expression d'Odunaiya, la formulation I2Q-FM et la simulation avec notre modèle de récepteur, sont tracées en utilisant 2 échelles de temps. Lorsque l'avion se déplace lentement au début de la trajectoire, on peut observer un bon accord entre la formulation I2Q-FM et le modèle du récepteur. Lorsque l'avion accélère, on observe des erreurs très faibles dans la réponse du récepteur. Comme pour le VORC, le multitrajet peut être filtré lorsque son décalage Doppler relatif est suffisamment élevé. Toutefois, cette dernière affirmation reste à démontrer.



(a) Réponse du récepteur entre 0 s et 18 s

(b) Réponse du récepteur entre 0 s et 640 s

Figure D.13: Validation de l'erreur I2Q-FM dans un scénario réaliste complexe.

D.4.5 Effet des multitrajets sur le signal de référence

Nous évaluons ici l'effet des multitrajets sur le signal de référence en vérifiant l'analyse de Bredemeyer qui consiste à considérer cet effet dans le calcul de l'erreur VORD.

Nous considérons un avion volant à 180 km/h d'azimut 0° à 90° tout au long d'une trajectoire circulaire autour d'une station VORD fonctionnant à une fréquence de 113 MHz avec une puissance de 50 W. La trajectoire est caractérisée par un rayon de 4,5 km et une altitude de 1 km. L'avion est considéré comme immobile au cours des 10 premières et dernières secondes.

Nous évaluons séparément l'effet des multitrajets sur les canaux VAR et REF. Les résultats sont présentés sur Figure D.14. Lorsque la différence de phase entre le signal direct et le multitrajet varie lentement à la fin de la trajectoire, on observe un effet significatif sur les deux canaux.

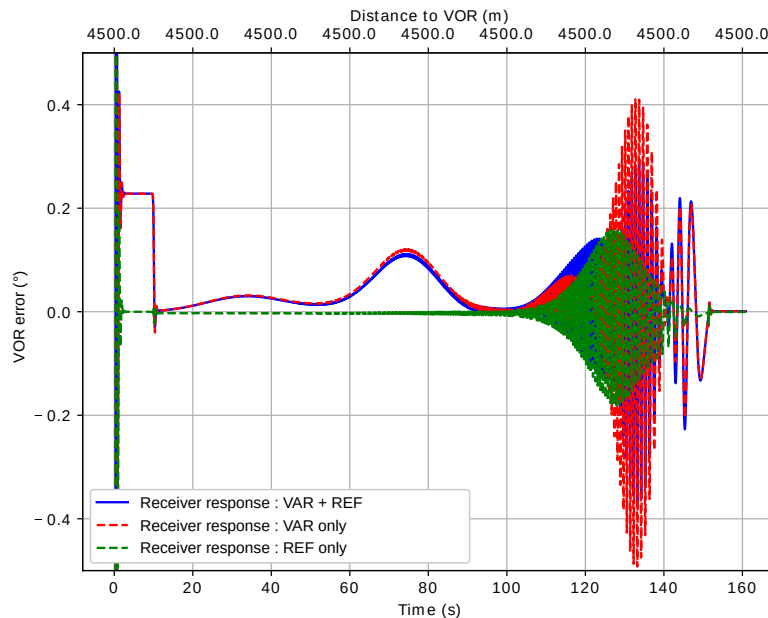
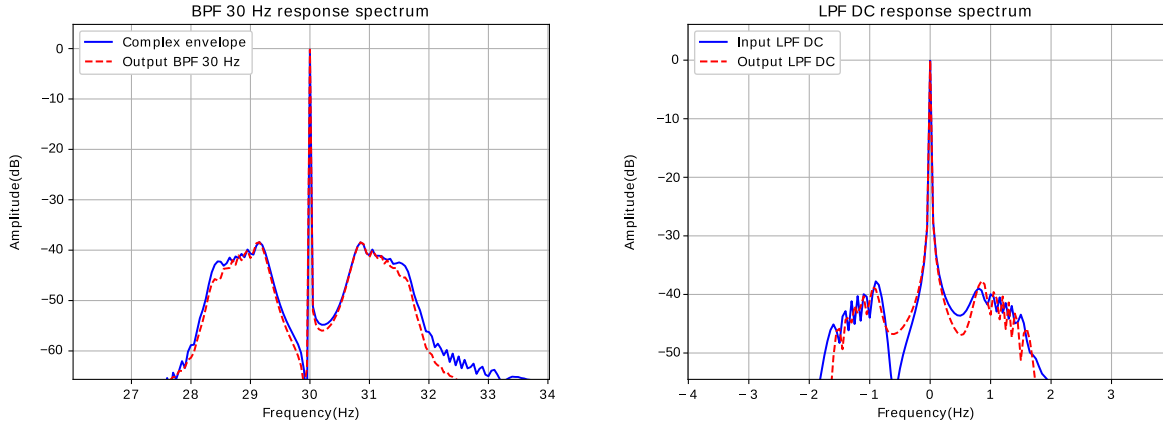


Figure D.14: Comparaison des effets des multitrajets sur les canaux VAR et REF.

Pour expliquer l'erreur générée sur le canal REF entre 120 s et 140 s, nous effectuons une analyse spectrale des signaux intermédiaires reçus au niveau du filtre passe-bande de 30 Hz du canal REF et du filtre passe-bas DC. Les résultats sont présentés sur Figures D.15a and D.15b. On observe que les deux filtres laissent passer le multitrajet avec un décalage Doppler qui varie de 0,7 Hz à 1,7 Hz autour du signal direct à 30 Hz. Cela explique les fluctuations de la réponse du récepteur.

Ce résultat est cohérent avec l'analyse effectuée par Bredemeyer. Néanmoins, ces analyses devraient être confirmées en réalisant une étude plus complète pour d'autres scénarios et avec d'autres types de démodulateurs FM.



(a) Entrée et sortie du filtre passe-bande 30 Hz

(b) Entrée et sortie du filtre passe-bas DC

Figure D.15: Spectre normalisé de l'entrée et de la sortie des filtres du récepteur.

D.4.6 Conclusion

Notre modèle de récepteur VOR numérique a été analysé dans ce chapitre. Un aperçu des principaux résultats est donné dans Table D.2.

Retard de groupe récepteur VORC/VORD	Validité de l'erreur VORD d'Odunaiya
<ul style="list-style-type: none"> Le retard de groupe récepteur est donné par $\tau_g^{\text{tot}} = \tau_g^{\text{BPF}} + \tau_g^{\text{LPF}}$	<ul style="list-style-type: none"> L'erreur Odunaiya est valable lorsque $f_0 \frac{v_{R_x}}{c_0} \hat{\mathbf{r}}_{\mathbf{w}_0} \cdot \hat{\mathbf{u}}_{\mathbf{m}} > \min\left(\frac{W_{30}}{2}, W_{\text{DC}}\right)$
Erreur VORD I2Q-FM	Effet multitrajet sur le signal REF
<ul style="list-style-type: none"> Démonstration de l'expression d'erreur (D.5) Cohérent avec le démodulateur FM en quadrature Validation dans des scénarios complexes 	<ul style="list-style-type: none"> Le signal REF est sensible aux multitrajets Cet effet a été évalué par simulation Les expressions d'erreur VOR ignorent cet effet

Table D.2: Aperçu des principaux résultats de ce chapitre.

D.5 Modèle statistique de l'erreur angulaire VORC

D.5.1 Introduction

Dans ce chapitre, nous présentons un modèle statistique de l'erreur multitrajet VORC pour lequel les distances VOR-avion et VOR-éolienne sont fixes alors que les autres

paramètres (taille de l'éolienne, matériaux, composition du sol, etc.) suivent des distributions statistiques. Notre approche est basée sur une analyse de Monte-Carlo.

D.5.2 Configuration

la configuration générale considérée dans notre modèle statistique est illustrée dans Figure D.16. On considère une éolienne de position connue \mathbf{r}_{w_0} au long de l'axe $\hat{\mathbf{x}}$. Nous supposons que cette éolienne produit un multitrajet d'amplitude modérée. On suppose que les caractéristiques du VOR et la position de l'avion sont connues.

Nous considérons que la variation de la position de l'éolienne autour de sa valeur moyenne suit une distribution normale d'écart type σ_w . Ce paramètre est supposé être faible par rapport aux distances entre le VOR et l'éolienne $\|\mathbf{r}_{w_0}\|$ et entre l'éolienne et l'avion $\|\mathbf{r}_{w_1}\|$,

$$\sigma_w \ll \|\mathbf{r}_{w_0}\|, \|\mathbf{r}_{w_1}\|. \quad (\text{D.6})$$

Les autres paramètres de configuration sont supposés suivre des distributions statistiques (normale et uniforme).

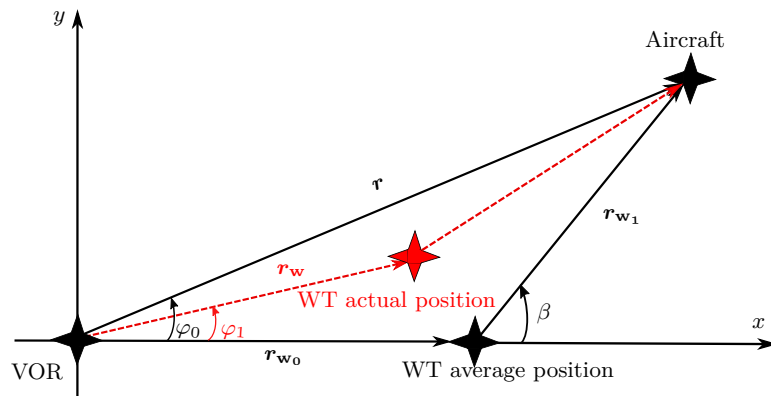


Figure D.16: Vue de dessus de la configuration et de la notation pour le modèle statistique.

D.5.3 Statistiques de l'erreur VORC

D'après l'expression d'Odunaiya pour le VORC, l'erreur angulaire pour un multitrajet d'amplitude modérée est exprimée comme suit

$$\varepsilon_{\text{Od}}^{\text{C}} = \frac{a_1}{a_0} \cos(\theta_1 - \theta_0) \sin(\varphi_1 - \varphi_0). \quad (\text{D.7})$$

Nous avons constaté que pour la configuration présentée précédemment, le multitrajet a approximativement une phase relative uniforme, un azimut relatif constant et une ampli-

tude relative de Rayleigh. À partir de l'expression d'Odunaiya, l'erreur VORC suit une distribution normale centrée d'écart type donné par

$$\sigma_1^{\varepsilon} = \sigma_1 |\sin(\varphi_1 - \varphi_0)|. \quad (\text{D.8})$$

où σ_1 est le paramètre de la distribution de Rayleigh. Nous effectuons l'analyse de Monte-Carlo afin d'évaluer ce paramètre et caractériser l'erreur VORC.

D.5.4 Cas de test

Un cas de test est présenté ici pour évaluer le paramètre de la distribution de Rayleigh en utilisant l'analyse de Monte-Carlo.

Nous considérons une station VORC fonctionnant à une fréquence de 113 MHz avec une puissance de 50 W. Cette station est caractérisée par une cône de silence de 40° . Une éolienne est placée à 3 km de la station VOR sur la radiale 0° . L'observation est définie sur une demi-sphère de rayon 10 km centrée sur l'éolienne. Pour la convergence du paramètre estimé dans les simulations de Monte-Carlo, on considère des variations de valeur estimée inférieures à 5% au cours des 10 dernières itérations.

Les résultats sont présentés dans Figures D.17 et D.18. Le multitrajet relatif est puissant dans la zone située derrière l'éolienne pour des angles Θ_0 élevés. Cette zone correspond à la zone de réflexion spéculaire du mât. Pour les angles moyens Θ_0 (entre 40° et 70°), on observe une contribution résiduelle qui est due aux pales.

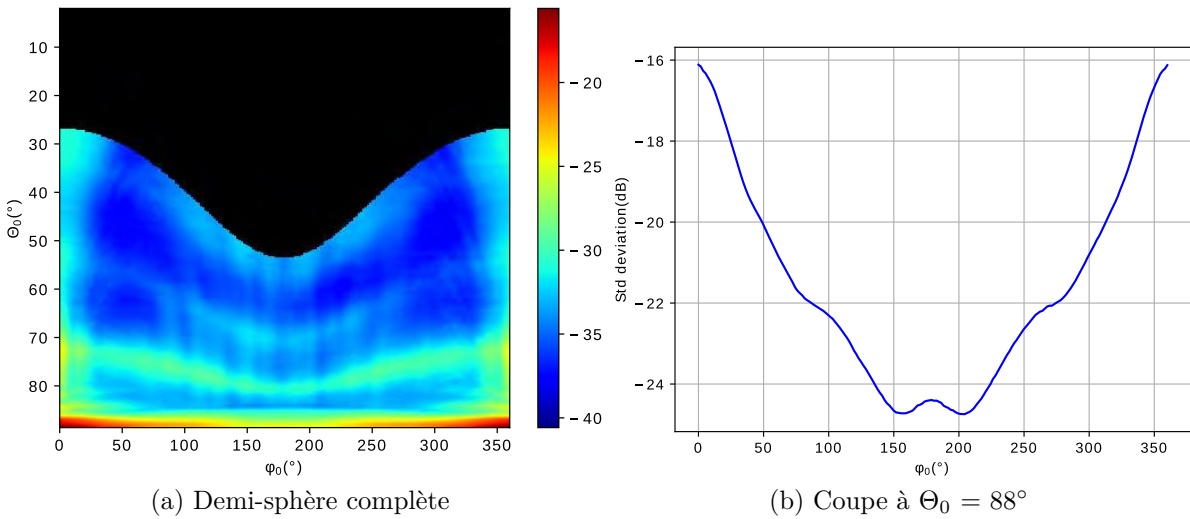


Figure D.17: Représentation 2D du paramètre de la distribution de Rayleigh associé à l'amplitude relative du multitrajet.

l'écart-type de l'erreur VOR atteint $0,3^\circ$ lorsque la différence d'azimut entre l'avion et l'éolienne est d'environ 90° ou 270° . En outre, l'écart-type est maximal pour les angles d'élévation faibles, *i.e.* où la diffusion du mât est maximale.

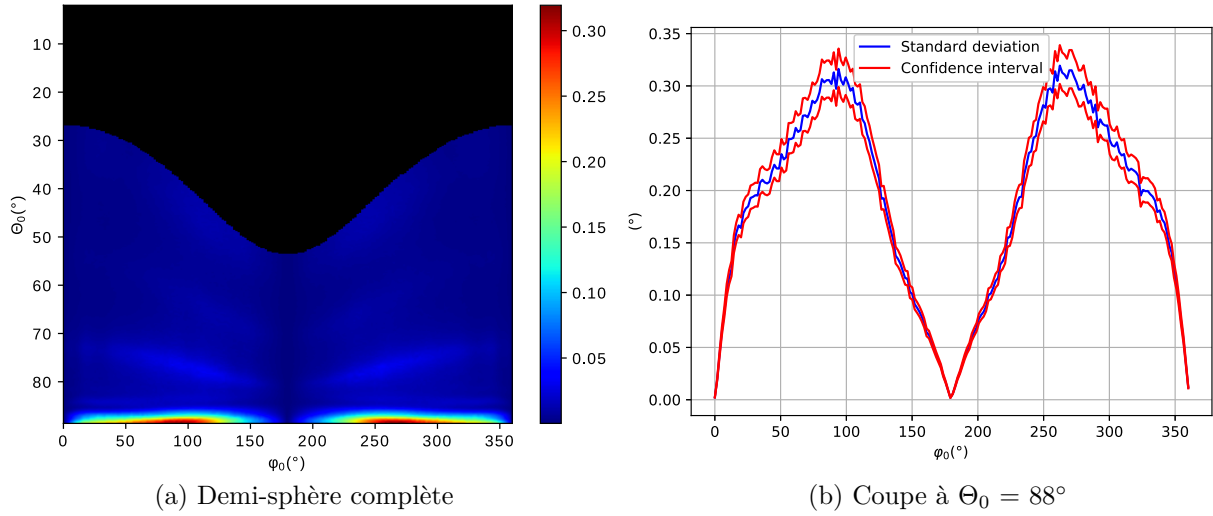


Figure D.18: Écart-type de la distribution normale centrée associée à l'erreur VORC.

D.5.5 Conclusion

Dans ce chapitre, un modèle statistique de l'erreur VORC a été présenté. Ce modèle fournit la distribution statistique de l'erreur lorsque la taille de l'éolienne, les matériaux, la composition du sol, etc. suivent des distributions statistiques. Notre modèle est basé sur une analyse de Monte-Carlo. Nous avons constaté que pour une éolienne dont la position est approximativement connue et à un point d'observation donné, le multitrajet a approximativement une phase relative uniforme, un azimut relatif constant et une amplitude relative de Rayleigh. Cela conduit à une distribution normale centrée pour l'erreur VORC.

D.6 Conclusion

L'objectif de cette thèse de doctorat était de proposer des outils rapides, précis et validés pour évaluer l'impact des multitrajets sur l'erreur VOR en présence d'éoliennes. Nous avons effectué les tâches suivantes :

- Développement d'un modèle de récepteur VOR numérique intégrant des réponses de filtrage et de démodulation
 - Reproduction de la réponse d'un récepteur VOR de manière réaliste.
 - Prise en compte de variations des multitrajets avec le temps dans l'erreur VOR.
- Analyse des multitrajets VORC à partir de mesures en laboratoire dans un environnement conduit

- Comparaison avec un récepteur de calibration (R&S EVS300).
- Bon accord entre les résultats \Rightarrow bonne confiance dans les paramètres du modèle de récepteur VOR numérique.
- Analyse de l'erreur angulaire obtenue à partir du modèle de récepteur
 - Évaluation du retard du groupe récepteur en fonction des paramètres de filtrage.
 - Montrer que l'expression Odunaiya n'est plus valable lorsque le multitrajet est fortement atténué par les filtres de récepteur.
 - Montrer la sensibilité du type de démodulateur FM sur le modèle d'erreur d'un récepteur VORD \Rightarrow développement d'une expression cohérente avec notre démodulateur en quadrature FM.
 - Mise en évidence de l'effet multitrajet sur le signal de référence pour le VORD \Rightarrow Vérification relative de l'analyse de Bredemeyer.
- Développement d'un modèle statistique de l'erreur VORC
 - Distribution normale centrée de l'erreur VORC pour une éolienne dont la position est approximativement connue et à un point d'observation donné.
 - Obtention du paramètre de la distribution de Rayleigh via l'analyse de Monte-Carlo.

Lists of my publications

- S. Ben-Hassine, A. Chabory, C. Morlaas, and R. Douvenot, “VOR times series for an aircraft trajectory in the presence of wind turbines,” in *22nd International Microwave and Radar Conference (MIKON 2018)*, (Poznan, Poland), pp. 116–118, May 2018
- S. Ben-Hassine, A. Chabory, C. Morlaas, and R. Douvenot, “A dynamic VOR receiver model for estimating the bearing error in the presence of wind turbines,” in *13th European Conference on Antennas and Propagation (EuCAP)*, (Krakow, Poland), pp. 1–4, March 2019
- S. Ben-Hassine, A. Chabory, C. Morlaas, and R. Douvenot, “An analytic formulation of the Doppler VOR multipath error for a digital receiver - comparaisons with the Odunaiya expression,” in *Specialist Meeting on Electromagnetic Waves and Wind Turbines (EMWT 2019)*, (Toulouse, France), December 2019
- S. Ben-Hassine, A. Chabory, C. Morlaas, and R. Douvenot, “Analysis of an IQ receiver model by means of laboratory measurements for conventional VOR,” in *Specialist Meeting on Electromagnetic Waves and Wind Turbines (EMWT 2019)*, (Toulouse, France), December 2019
- A. Chabory, S. Ben-Hassine, C. Morlaas, and R. Douvenot, “A statistical model for assessing the impact of wind turbines on conventionnal VOR,” in *Specialist Meeting on Electromagnetic Waves and Wind Turbines (EMWT 2019)*, (Toulouse, France), December 2019
- S. Ben-Hassine, A. Chabory, C. Morlaas, and R. Douvenot, “Validity domain of the Odunaiya expression for computing the conventional VOR multipath error,” in *14th European Conference on Antennas and Propagation (EuCAP)*, (Copenhagen, Denmark), March 2020

Bibliography

- [1] T. Sequeira and L. Reis, *Climate Change and Global Development*. Springer, 2019.
- [2] S. Odunaiya, “A Physical Theory of Diffraction Model for Predicting the Effects of Multipath on VOR Performance,” in *Institute of Navigation, National Technical Meeting’Vision 2010: Present and Future’, San Diego, CA*, pp. 435–446, 1999.
- [3] S. Odunaiya and D. Quinet, “Calculations and analysis of signal processing by various navigation receivers architectures,” in *The 23rd Digital Avionics Systems Conference*, pp. 1.D.1–11, Oct 2004.
- [4] C. Morlaas, M. Fares, and B. Souny, “Wind turbine effects on VOR system performance,” *IEEE Transactions on Aerospace and Electronic Systems*, vol. 44, no. 4, pp. 1464–1476, 2008.
- [5] D. de la Vega, C. Fernández, O. Grande, I. Angulo, D. Guerra, Y. Wu, P. Angueira, and J. L. Ordiales, “Software tool for the analysis of potential impact of wind farms on radiocommunication services,” in *IEEE International Symposium on Broadband Multimedia Systems and Broadcasting (BMSB)*, (Nuremberg, Germany), pp. 1–5, June 2011.
- [6] T. Schrader, “Predicting DVOR Bearing Errors Caused by Wind Turbines - A New Tool,” in *Specialist Meeting on Electromagnetic Waves and Wind Turbines (EMWT2019)*, (Toulouse, France), 2019.
- [7] S. Sandmann, J. Bredemeyer, T. Schrader, and M. Mihalachi, “Comparing Predicted and Measured Time-variant DVOR Bearing Errors in Presence of Wind Turbines,” in *Specialist Meeting on Electromagnetic Waves and Wind Turbines (EMWT2019)*, (Toulouse, France), 2019.
- [8] C. Morlaas, A. Chabory, and B. Souny, “Propagation model for estimating VOR bearing error in the presence of windturbines — Hybridization of parabolic equation with physical optics,” in *Proceedings of the Fourth European Conference on Antennas and Propagation (EuCAP)*, (Barcelona, Spain), pp. 1–5, April 2010.
- [9] L. Claudepierre, *Simulateur Électromagnétique d’Erreur VOR par Méthodes Déterministes—Application aux Parcs Éoliens*. PhD thesis, University of Toulouse, 2015.

- [10] L. Claudepierre, R. Douvenot, A. Chabory, and C. Morlaas, “A deterministic VOR error modeling method—Application to wind turbines,” *IEEE Transactions on Aerospace and Electronic Systems*, vol. 53, no. 1, pp. 247–257, 2017.
- [11] I. González, E. Garcia, F. Saez de Adana, and M. Cátedra, “MONURBS: a parallelized fast multipole multilevel code for analyzing complex bodies modeled by NURBS surfaces,” *Applied Computational Electromagnetics Society Journal*, vol. 23, no. 2, pp. 134–142, 2008.
- [12] L. S. Rashid and A. K. Brown, “RCS and radar propagation near offshore wind farms,” in *IEEE Antennas and Propagation Society International Symposium*, (Honolulu, USA), pp. 4605–4608, June 2007.
- [13] ICAO, “Annex 10 to the convention on international civil aviation,” tech. rep., International Civil Aviation Organisation (ICAO), July 2006.
- [14] D. Wyatt and M. Tooley, *Aircraft Communications and Navigation Systems*. Routledge, 2013.
- [15] A. Helfrick, *Principles of Avionics*. Avionics Communications, 2010.
- [16] J. Chitode, *Principles of Communication*. Technical Publications, 2009.
- [17] I. González, L. Lozano, J. Gómez, A. Tayebi, I. Etayo, and M. F. Cátedra, “Analysis of the scattering field of wind turbine using rigorous and asymptotic techniques,” in *Proceedings of the Fourth European Conference on Antennas and Propagation (EuCAP)*, (Barcelona, Spain), pp. 1–4, April 2010.
- [18] A. C. Casanova, M. C. Ramon, L. de Haro y Ariet, and P. Blanco-Gonzalez, “Wind farming interference effects,” in *5th International Multi-Conference on Systems, Signals and Devices*, (Amman, Jordan), pp. 1–6, July 2008.
- [19] F. Weinmann, “Ray tracing with PO/PTD for RCS modeling of large complex objects,” *IEEE Transactions on Antennas and Propagation*, vol. 54, no. 6, pp. 1797–1806, 2006.
- [20] F. Weinmann, “PO/PTD ray tracing for arbitrary metallic and dielectric objects,” in *First European Conference on Antennas and Propagation (EuCAP)*, (Nice, France), pp. 1–5, Nov 2006.
- [21] F. Weinmann, “Stochastic scattering model for the application of SBR to rough surfaces,” in *Proceedings of the 5th European Conference on Antennas and Propagation (EuCAP)*, (Rome, Italy), pp. 6–9, April 2011.
- [22] F. Weinmann, “Accurate prediction of EM scattering by wind turbines,” in *The 8th European Conference on Antennas and Propagation (EuCAP)*, (The Hague, Netherlands), pp. 2317–2321, April 2014.

- [23] L. Claudepierre, R. Douvenot, and C. Morlaas, “A simple and accurate electromagnetic model of a windturbine blade at radar frequency,” in *International Conference on Electromagnetics in Advanced Applications (ICEAA 2014)*, (Palm Beach, Netherlands Antilles), pp. 253–256, Aug 2014.
- [24] L. Claudepierre, R. Douvenot, A. Chabory, and C. Morlaas, “Assessment of the shadowing effect between windturbines,” in *9th European Conference on Antennas and Propagation (EuCAP)*, (Lisbon, Portugal), pp. 1–4, April 2015.
- [25] L. Claudepierre, R. Douvenot, A. Chabory, and C. Morlaas, “A method for computing the VOR multipath error - Comparisons with in-flight measurements,” in *10th European Conference on Antennas and Propagation (EuCAP)*, (Davos, Switzerland), pp. 1–5, April 2016.
- [26] A. Calo Casanova, P. H. Pathak, and M. Calvo Ramón, “Modeling windmill interference via hybrid parabolic equation and equivalent current approximation methods,” in *International Conference on Electromagnetics in Advanced Applications*, (Torino, Italy), pp. 275–278, Sep. 2011.
- [27] A. Chabory, S. Ben-Hassine, C. Morlaas, and R. Douvenot, “A statistical model for assessing the impact of wind turbines on conventionnal VOR,” in *Specialist Meeting on Electromagnetic Waves and Wind Turbines (EMWT 2019)*, (Toulouse, France), December 2019.
- [28] M. Levy, *Parabolic Equation Methods for Electromagnetic Wave Propagation*. No. 45, IET, 2000.
- [29] J. R. Kuttler and G. D. Dockery, “Theoretical description of the parabolic approximation/Fourier split-step method of representing electromagnetic propagation in the troposphere,” *Radio Science*, vol. 26, no. 02, pp. 381–393, 1991.
- [30] D. Dockery and J. R. Kuttler, “An improved impedance-boundary algorithm for Fourier split-step solutions of the parabolic wave equation,” *IEEE Transactions on Antennas and Propagation*, vol. 44, pp. 1592–1599, Dec 1996.
- [31] A. Chabory, *Modélisation Électromagnétique des Radômes par des Techniques Basées sur les Faisceaux Gaussiens*. PhD thesis, University of Toulouse, 2004.
- [32] Shung-Wu Lee and R. Mittra, “Fourier transform of a polygonal shape function and its application in electromagnetics,” *IEEE Transactions on Antennas and Propagation*, vol. 31, pp. 99–103, January 1983.
- [33] C. A. Balanis, *Advanced Engineering Electromagnetics*. John Wiley & Sons, 1999.
- [34] M. Kayton and W. R. Fried, *Avionics Navigation Systems*. John Wiley & Sons, 1997.
- [35] T. N. Tye, *Application of Digital Signal Processing Methods to Very High Frequency Omnidirectional Range (VOR) Signals in the Design of an Airborne Flight Measurement System*. PhD thesis, Ohio University, 1996.

- [36] J. I. Park and H. S. Park, “A study on demodulation system design of the VOR receiver,” in *Future Information Technology*, pp. 343–349, 2011.
- [37] A. B. Carlson, *An Introduction to Signals and Noise in Electrical Communication*. Communication Systems, 4th Edition, McGraw Hill, 2002.
- [38] S. Haykin, *Communication Systems*. John Wiley & Sons, 2008.
- [39] J. G. Proakis, *Digital Signal Processing: Principles Algorithms and Applications*. Pearson Education India, 2001.
- [40] L. W. Couch, H. Shao, X. Li, and L. Liu, *Digital and Analog Communication Systems*. Pearson, 1997.
- [41] H. Voelcker, “Zero-crossing properties of angle-modulated signals,” *IEEE Transactions on Communications*, vol. 20, no. 3, pp. 307–315, 1972.
- [42] T. Scholand, C. Spiegel, A. Waadt, A. Burnic, and P. Jung, “A real-time zero-crossing demodulation concept,” *Wireless Personal Communications*, vol. 43, no. 2, pp. 157–183, 2007.
- [43] G. D. Mandyam, “Analysis of a digital quadrature discriminator for an AMPS handset,” in *IEEE 49th Vehicular Technology Conference*, (Houston, USA), pp. 1906–1909, May 1999.
- [44] A. Nitescu-Henry, F. O. Eynde, S. A. Spanoche, D. Claudius, and S. M. Popescu, “A fully-integrated FM discriminator for RDS applications,” in *Proceedings of the 23rd European Solid-State Circuits Conference*, (Southampton, UK), pp. 92–95, Sep. 1997.
- [45] A. V. Räisänen, J. Zheng, J. Ala-Laurinaho, and V. Viikari, “Antenna measurements at millimeter wavelengths — Overview,” in *12th European Conference on Antennas and Propagation (EuCAP)*, (London, UK), pp. 1–3, April 2018.
- [46] I. W. Selesnick and C. S. Burrus, “Generalized digital Butterworth filter design,” *IEEE Transactions on Signal Processing*, vol. 46, no. 6, pp. 1688–1694, 1998.
- [47] R. W. Hamming, *Digital Filters*. Courier Corporation, 1998.
- [48] B. A. Shenoi, *Introduction to Digital Signal Processing and Filter Design*. John Wiley & Sons, 2005.
- [49] M. Abramowitz and I. A. Stegun, *Handbook of Mathematical Functions with Formulas, Graphs, and Mathematical Tables*. US Government printing office, 1948.
- [50] J. Bredemeyer, “Further expertise on the interaction between wind turbines and the DVOR MIC with special consideration on the interference effects on the receiver,” tech. rep., Flight Calibration Services, 2015.

- [51] E. Hossain, M. Rasti, and L. B. Le, *Radio Resource Management in Wireless Networks: An Engineering Approach*. Cambridge University Press, 2017.
- [52] M. E. Allen, “Kolmogorov-smirnov test for discrete distributions,” tech. rep., Naval Postgraduate School Monterey CA, 1976.
- [53] C. P. Tsokos, *Probability for Engineering, Mathematics, and Sciences*. Cengage Learning, 2012.
- [54] A. Papoulis, *Probability, Random Variables, and Stochastic Processes*. McGraw-Hill, 1991.
- [55] Ministry for the Ecological and Inclusive Transition, “Open platform for French public geographic data.” <https://geo.data.gouv.fr/fr/>. Online; accessed 05 November 2019.
- [56] ENERCON GmbH. <https://www.enercon.de>. Online; accessed 16 November 2019.
- [57] Vestas Wind Systems A/S. <https://www.vestas.com>. Online; accessed 16 November 2019.
- [58] K. Rao, *Wind Energy for Power Generation: Meeting the Challenge of Practical Implementation*. Springer, 2019.
- [59] S. Ben-Hassine, A. Chabory, C. Morlaas, and R. Douvenot, “VOR times series for an aircraft trajectory in the presence of wind turbines,” in *22nd International Microwave and Radar Conference (MIKON 2018)*, (Poznan, Poland), pp. 116–118, May 2018.
- [60] S. Ben-Hassine, A. Chabory, C. Morlaas, and R. Douvenot, “A dynamic VOR receiver model for estimating the bearing error in the presence of wind turbines,” in *13th European Conference on Antennas and Propagation (EuCAP)*, (Krakow, Poland), pp. 1–4, March 2019.
- [61] S. Ben-Hassine, A. Chabory, C. Morlaas, and R. Douvenot, “An analytic formulation of the Doppler VOR multipath error for a digital receiver - comparaisons with the Odunaiya expression,” in *Specialist Meeting on Electromagnetic Waves and Wind Turbines (EMWT 2019)*, (Toulouse, France), December 2019.
- [62] S. Ben-Hassine, A. Chabory, C. Morlaas, and R. Douvenot, “Analysis of an IQ receiver model by means of laboratory measurements for conventional VOR,” in *Specialist Meeting on Electromagnetic Waves and Wind Turbines (EMWT 2019)*, (Toulouse, France), December 2019.
- [63] A. Chabory, S. Ben-Hassine, C. Morlaas, and R. Douvenot, “A statistical model for assessing the impact of wind turbines on conventionnal VOR,” in *Specialist Meeting on Electromagnetic Waves and Wind Turbines (EMWT 2019)*, (Toulouse, France), December 2019.

- [64] S. Ben-Hassine, A. Chabory, C. Morlaas, and R. Douvenot, “Validity domain of the Odunaiya expression for computing the conventional VOR multipath error,” in *14th European Conference on Antennas and Propagation (EuCAP)*, (Copenhagen, Denmark), March 2020.
- [65] L. Fei, H. Yue, and L. Yuankai, “Research on height and diameter of Doppler VHF omnidirectional beacon in complex environment,” in *IOP Conference Series: Materials Science and Engineering*, vol. 608, (Shanghai, China), p. 012005, 2019.
- [66] J. Perez, F. Saez de Adana, O. Gutierrez, I. Gonzalez, M. F. Catedra, I. Montiel, and J. Guzman, “FASANT: fast computer tool for the analysis of on-board antennas,” *IEEE Antennas and Propagation Magazine*, vol. 41, no. 2, pp. 94–98, 1999.
- [67] S. Laybros, H. Mametsa, P. Combes, and P. N’Guyen, “Unified asymptotic methods formulations for the shooting and bouncing ray technique,” in *International Conference on Electromagnetics in Advanced Applications*, (Torino, Italy), pp. 1–3, 2003.
- [68] A. Warrington, *Protective Relays: Their Theory and Practice*. Springer Science & Business Media, 2012.
- [69] C. Wadhwa, *Electrical Power Systems*. New Age International, 2006.
- [70] B. Ram, *Power System Protection and Switchgear*. Tata McGraw-Hill Education, 2011.
- [71] S. Sarkar, U. Maulik, and B. N. Biswas, “A new digital phase lock loop using fuzzy controlled discrete energy separation algorithm 1a,” *International Journal of Electronics and Communication Technology*, vol. 5, pp. 46–49, 2014.
- [72] J.-L. Azan, *Précis d’Électronique*, vol. 1. Editions Bréal, 1993.
- [73] H. Zhou, *Modeling the Atmospheric Propagation of Electromagnetic Waves in 2D and 3D using Fourier and Wavelet Transforms*. PhD thesis, University of Toulouse, 2018.
- [74] N. T. Larsen, D. F. Vecchia, and G. R. Sugar, “VOR calibration services,” *National Bureau of Standards technical note*, no. 1069, 1985.
- [75] C. Binns, *Aircraft Systems: Instruments, Communications, Navigation and Control*. Wiley-IEEE Press, 2018.
- [76] S. A. Odunaiya, “Wind farms and their effect on radio navigation aids,” in *14th SIIV IFIS*, (Toulouse, France), pp. 77–80, June 2006.